Thermodynamic Principle and Engineering of Resistive Memory

by

Jingxian Li

A dissertation submitted in partial fulfillment
of the requirements for the degree of
Doctor of Philosophy
(Materials Science and Engineering)
in the University of Michigan
2024

Doctoral Committee:

Assistant Professor Yiyang Li, Chair
Associate Professor John T. Heron
Professor Wei D. Lu
Assistant Professor Wenhao Sun

Jingxian Li

jxli@umich.edu

ORCID iD: 0000-0003-0222-1213

© Jingxian Li 2024

Dedication

To my beloved family, whose unwavering support and encouragement have been my foundation. To my friends and colleagues, whose camaraderie and inspiration have enriched my journey. And to my girlfriend, whose love and patience have been my constant source of strength. This work is dedicated to all of you.

Acknowledgements

I would like to express my deepest gratitude to those who have supported and guided me throughout my PhD journey. First and foremost, I extend my heartfelt thanks to my advisor, Professor Yiyang Li, for his invaluable mentorship, encouragement, and guidance. His profound insights and unwavering support have been instrumental in shaping my research and academic growth.

I am also deeply grateful to my committee members for their constructive feedback and encouragement. Thank you to Professor Wenhao Sun for sharing his thermodynamic knowledge and for always being available to discuss my work and life. My sincere thanks to Professor John T. Heron for his expertise and insightful advice, which has greatly enriched my research. I am immensely grateful to Professor Wei D. Lu for his guidance, inspiration, and for providing us with excellent research resources. I also want to extend a special mention to the department PhD program chair, Professor Geeta Mehta, for her constant support during the final stage of my PhD.

I would like to acknowledge and thank all my group members, Diana Kim, Lindsay Gubow, Brianna Roest, Virgil Watkins, Jinhong Min, Laszlo Cline, Riley Hargrave, Dongjae Shin, Andrew Jalbert, Emily MacInnis, Leah Simakas, Noah Giesler, Sabrina Wong, Pengyu Ren, Po-Yu Kung, Sangyong Lee, Yerin Hong, Harshada Suryawanshi, and Wonjoon Suk for their camaraderie, support, and collaborative spirit. Your ideas, discussions, and friendship have made this journey both enjoyable and rewarding.

I would also like to thank the collaborators for their technical support and inspiring discussion: Anirudh Appachar, Dr. Sangmin Yoo, Tony Chiang, and Dr. Kai Sun at University of Michigan; Dr. Sabrina L. Peczonczyk, and Dr. Elisa T. Harrison at Ford Research; Dr. Anton V. Ievlev, Dr. Olya Popova, and Dr. Petro Maksymovych at Oak Ridge National Laboratory; Dr. Ryan Hood, Dr. Suhas Kumar, and Dr. Alec Talin at Sandia National Laboratories; Dr. Karsten Beckmann, and Dr. Nathaniel Cady at University at Albany.

Next, I would like to thank the staff members in this university: Dr. Haiping Sun, Dr. Allen Hunter, Dr. Nancy Senabulya Muyanja, and Dr. Tao Ma in the Michigan Center for Materials Characterization (MC2); Katharine Beach, Dr. Jorge Barreda, Casey Jackson, Shawn Wright, Matthew Oonk, Dr. Vishva Ray, and Dr. Sandrine Martin in the Lurie Nanofabrication Facility (LNF); Dr. Ying Qi, and Dr. Sahar Farjami in the Van Vlack lab; Keith McIntyre, Renee Hilgendorf, and Shelley Fellers in the department.

To my friends, thank you for your unwavering support, for always being there to listen, for joining me on restaurant adventures in Ann Arbor, and for providing a balance between work and relaxation. A special thank you to my girlfriend, Mengru Wang, whose love, patience, and encouragement have been a source of strength and motivation throughout this journey. Your support has meant the world to me. Lastly, I am profoundly grateful to my family for their unconditional love and support. Thank you for believing in me and for always encouraging me to pursue my dreams.

This accomplishment would not have been possible without the support and encouragement of all these amazing individuals.

Table of Contents

Dedication ii

Acknowledgements iii

List of Figures viii

List of Appendices xvi

Abstract xvii

Chapter 1 Nonvolatile Memory 1

1.1 Resistive Memory 2

1.1.1 Resistive Random Access Memory 3

1.1.2 Electrochemical Random Access Memory 6

1.2 Application 7

1.2.1 Neuromorphic Computing 9

1.2.2 High-temperature Memory 9

1.3 Device Fabrication 10

1.4 Electrical Characterization 13

1.4.1 Switching 13

1.4.2 Endurance 14

1.4.3 Retention 15

1.5 Device Characterization 16

1.5.1 Transmission Electron Microscopy 16

1.5.2 Conductive Atomic Force Microscopy 16

Chapter 2 Diffusion 19

2.1 Diffusion 19
2.1.1 Fickian Diffusion 19
2.1.2 Phase Separation 20
2.2 Material System 22
2.3 Diffusion in Resistive Memory 24
2.3.1 Fickian Diffusion in Resistive Memory 24
2.3.2 Phase Separation in Resistive Memory 26
2.4 Phase-field Model 27
2.4.1 Phase Separation Model 28
2.4.2 Fickian Diffusion Models 29
2.4.3 Electronic Conductance Models 29
2.5 Material Characterization 31
2.5.1 Auger Electron Spectroscopy 31
2.5.2 Time-of-Flight, Secondary Ion Mass Spectrometry 32
Chapter 3 Thermodynamic Origin of Nonvolatility in ReRAM 35
3.1 Phase Separation Hypothesis 35
3.2 Retention Measurements in TaO_X-based ReRAM 37
3.3 Composition Phase Separation in Amorphous Ta-O System 42
3.4 Ab initio Thermodynamic Calculations 46
3.5 Phase-field Simulations of Device Operation 51
3.6 Experimental Verification of Phase-field Model 56
3.7 Conclusion 59
Chapter 4 Composition-dependent Diffusion in ReRAM 60
4.1 Composition-dependent Diffusion Hypothesis 60
4.2 Oxygen Tracer Diffusion in TaO_X 61

4.3 Retention Simulation with Composition-dependent Diffusivity....64
4.4 Conclusion....65
Chapter 5 Thermodynamic Engineering for ECRAM....67
5.1 Phase Separation Enables Nonvolatile Phenomena....67
5.2 TaO_X-based ECRAM as High Temperature Binary Memory....68
5.3 Electron Microscopy Reveals Compositional Phase Separation....72
5.4 Device Simulation of TaO_X-based ECRAM....75
5.5 Analog and Temperature-depending Switching....78
5.6 Conclusion....85
Chapter 6 Conclusion and Future Work....86
6.1 Summary....86
6.1.1 Thermodynamics and Kinetics in ReRAM....87
6.1.2 Thermodynamic Engineering for Nonvolatile ECRAM....88
6.2 Future Work....89
6.2.1 Downscaling ECRAM....89
6.2.2 Fabrication of ECRAM Arrays for High-temperature Applications....90
Appendices....92
References....97

List of Figures

Figure 1.1: Properties of nonvolatile memories and application requirements[2]. Image reproduced with permission from ref.[2]. Copyright 2020.....1

Figure 1.2: Category of Resistive memory based on the number of terminals involved.....3

Figure 1.3: Illustration of an filament in the OFF state (HRS) and ON state (LRS) in an anion-type (top) and cation-type (bottom) ReRAM device[2]. Image reproduced with permission from ref.[2]. Copyright 2020.....5

Figure 1.4: Device structure and operation principle of a ECRAM device based on cation intercalation[10]. Image reproduced with permission from ref.[10]. Copyright 2023.....6

Figure 1.5: The race towards future computing solutions[14]. Image reproduced with permission from ref.[14]. Copyright 2018.....8

Figure 1.6: Illustration of ReRAM fabrication workflow.....12

Figure 1.7: Illustration of c-AFM measurement on ReRAM device with LRS after removing top electrode.....17

Figure 2.1: Schematic illustrating (a) Fickian diffusion and (b) phase separation.....19

Figure 2.2: Phase diagram, governed by thermodynamic variables, has guided strategies for controlling materials microstructure. The discovery of spinodal decomposition (dotted line) introduced a new understanding beyond nucleation and growth below the binodal line.....21

Figure 2.3: Phase Diagrams of four transition metal oxide systems, including of (a) Tungsten-Oxygen[40], (b) Titanium-Oxygen[44], (c) Tantalum-Oxygen[45], and (d) Hafnium-Oxygen[46].....23

Figure 2.4: HAADF image of the active area of the TaOx device showing phase separation[47]...27

Figure 2.5: Device and switching layer geometry used in the simulation. (a) Device geometry for 2D retention simulation. (b) Dispersion is assumed to be linearly proportional to the gap size in both the horizontal and vertical directions. (c) Boundary labels in 2D device.....28

Figure 2.6: Experimental setup for AES depth profiling on oxide bilayer before and after annealing treatment. The Pt cap layer is grown to block oxidation in the air.....31

Figure 2.7: Sample preparation for ToF-SIMS. (a) Tracer diffusion samples are traditionally conducted by annealing a natural-abundance (^{16}O) film in $^{18}O_2$-enriched gas at elevated

temperatures. (b) Our novel trilayer structure that embeds the ^{18}O tracer into the film stack enables tracer diffusivity measurement in sub-oxide films. 33

Figure 3.1: Schematic of potential oxygen vacancy migration pathways under no applied voltage in bilayer TaOx ReRAM. a) Fick's first law for ideal solutions, which states that mobile species diffuse from high to low concentration, suggests that the Ta_2O_5 will rapidly gain oxygen vacancies when in contact with a suboxide, resulting in failure shortly after fabrication. b) Most models assume that oxygen vacancies do not migrate between the two oxide layers during retention. Under this diffusion model, the filament dissolves, resulting in increased resistance over time, a result consistent with some experiments. **c)** Other experiments suggest that the filament strengthens over time, yielding a decrease in resistance. This result cannot be explained by either ideal solution Fickian diffusion model, and represents a knowledge gap. We propose this behaviour results from phase separation. Image reproduced with permission from ref.[51]. Copyright 2024. 36

Figure 3.2: (a) X-ray diffraction, (b) cross-section TEM and EDS images of (c) Ta signal and (d) Oxygen signal on TaO_X samples annealed at 300ºC. Both the X-ray diffraction and the TEM-fast Fourier transform indicate that the sample remains largely amorphous. Image reproduced with permission from ref.[51]. Copyright 2024. 37

Figure 3.3: Switching, retention, and conductive AFM characterization of the bilayer TaO_X-based memristors. a) A typical switching curve from the ~2 μm^2 crossbar device shows typical resistive switching behaviour. The inserts show cross-section TEM (top left, 10 nm scale bar) and planar SEM image (bottom right, 10 μm scale bar) b) Retention characteristics of devices from the pristine state, HRS, and LRS baked at 250 ºC. LRS and pristine state devices are stable, while HRS devices fail over time. The grey dashed line represents the failure threshold. c) HRS retention failure statistics show accelerated device failure as the bake temperature increases. The error bar represents one standard deviation for a binomial distribution (fail or not fail). d-f) C-AFM of the conductive filaments in devices with LRS device (d), HRS device (e), and HRS device annealed at 300ºC for 3 hours (f). The broken HRS filament re-forms after annealing in (f). Scale bar is 20 nm. Image reproduced with permission from ref.[51]. Copyright 2024. 38

Figure 3.4: Conductance cumulative probability distribution of $Pd/TaO_X/Ta_2O_5/Pd$ devices in HRS and LRS. Image reproduced with permission from ref.[51]. Copyright 2024. 38

Figure 3.5: (a) Retention measurements of devices from the pristine state, HRS, LRS baked at 300ºC in Ar. (b) The same LRS and HRS retention results are observed in both Ar and air environments, confirming that our observations are not a result of environmental reduction. (c-d) Retention measurements of devices from the pristine state, HRS, LRS baked at 200ºC (c) and 350ºC in Ar. Image reproduced with permission from ref.[51]. Copyright 2024. 40

Figure 3.6: Atomic force microscopy images on all devices. (a) Pristine (not switched) ReRAM devices, (b) pristine devices after annealing at 300°C for 3 hours, (c) LRS devices with 1mA compliance current, (d) LRS devices with 100 μA compliance current, (e) HRS with 1mA compliance current and 1.5 V RESET voltage, (f) HRS with 1mA compliance current and

1.5 V RESET voltage after annealing at 300°C for 3 hours. Image reproduced with permission from ref.[51]. Copyright 2024. 41

Figure 3.7: Compositional phase separation probed by Auger electron spectroscopy (AES) depth profile of bilayer stack Ta_2O_5/TaO_X. a) The AES depth profile results of $Ta_2O_5/TaO_{0.7}$ before (left panel) and after annealing at 300°C for 3, 16 and 48 hours (right panel). While the Ta_2O_5 is initially oxidised to $TaO_{1.9}$, it does not undergo further exchange of oxygen with the suboxide; this persistent interface after annealing indicates compositional phase separation. A darker plot background colour indicates higher Ta content. b) The AES depth profile results of three bilayer stacks before (left panel) and after annealing at 300 °C for 3 hours (right panel) suggest that the solubility limit at 300°C is $TaO_{1.9}$. Our results do not show substantial sputter reduction due to the relatively uniform metal:oxygen ratio with depth within each (sub)oxide layer. Dashed vertical guidelines convey 30 at% and 60 at% Ta. Image reproduced with permission from ref.[51]. Copyright 2024. 43

Figure 3.8: Auger electron spectroscopy depth profile on $Ta_2O_5/TaO_{0.7}$ bilayer stack (a) before and after annealing at (b) 300°C for 48 hours and (c) 450°C for 24 hours. Image reproduced with permission from ref.[51]. Copyright 2024. 44

Figure 3.9: Auger electron spectroscopy (AES) depth profile of $HfO_2/HfO_{0.4}$ shows composition phase separation. a) Schematic of the bilayer sample $HfO_2/HfO_{0.4}$ with (b) and without (c-e) 60 nm Pt blocking layer. We included the Pt interlayer in (b) to suppress O diffusion between the two Hafnia layers. b) The AES depth profile of $HfO_2/Pt/HfO_{0.4}$ shows the compositions of a "pristine" material. c) Without a Pt blocking layer, the $HfO_2/HfO_{0.4}$ bilayer would exchange oxygen even at room temperature, such that the HfO_2 layer is reduced to $HfO_{1.6}$ d-e) After annealing at 300°C, the composition gradient persists, which suggests amorphous phase separation like for TaOx bilayer (Figure 3.7). Unlike the case for TaOx, the HfOx suboxide layer became more oxidised over time due to residual oxygen during annealing. However, the top $HfO_{1.6}$ layer composition remains unchanged despite annealing, just as the $TaO_{1.9}$ layer in Figure 3.7, indicating phase separation. In addition to the anneal, these samples also resided at RT for 27 days before the AES measurement. f) The Hf atomic fraction for the samples in (b-e). Without a blocking Pt layer, HfO_2 is reduced to $HfO_{1.6}$ for all conditions tested. We anticipate $HfO_{1.6}$ to be one stable phase in the amorphous Hf-O system, just as $TaO_{1.9}$ is a stable phase in amorphous Ta-O system (Figure 3.7). This composition phase separation result is broadly similar to that of the Ta-O bilayer tested in Figure 3.7. Image reproduced with permission from ref.[51]. Copyright 2024. 45

Figure 3.10: Atomistic calculation and phase-field simulation of Ta-O system. a) Mixing free energy of TaO_X across a series of compositions including enthalpy and entropy at 300°C (see Experimental Proecdures). These energies are referenced that of amorphous Ta (X*=0) and Ta_2O_5 (X*=1) at 0K. The common tangent and the convex hull indicate phase separation between ~$TaO_{1.9}$ (X*~0.74) and Ta (X*~0). The insert is the amorphous structure generated. b-c) Phase-field simulation of oxygen diffusion in bilayer stacks of (b) $Ta_2O_5/TaO_{0.7}$ and (c) Ta_2O_5/TaO which incorporates phase separation with the formation energy fitted from (a). These simulations qualitatively capture the Auger depth profile in Figure 3.7b. The light color line is the simulation results, and the dark color line is the 5-nm average value to account for

depth- and lateral-average of AES measurement. Image reproduced with permission from ref.[51]. Copyright 2024.....46

Figure 3.11: X-ray reflectivity characterizations on TaO_X thin film thickness and density. (a) X-ray reflectivity result of Ta_2O_5 thin film grown on Si chip with fitted curve. (b) Density of TaO_X of different compositions derived from X-ray reflectivity. A linear fitting between density and oxygen percentage is used to calculate the volume/atom for DFT calculation. Image reproduced with permission from ref.[51]. Copyright 2024.....47

Figure 3.12: Amorphous Formation Energy at 0K calculated by DFT referenced to the elemental states of Ta and O. The plot includes the convex hull of crystalline phases. To obtain the mixing free energy (Figure 3.10a), we subtract the formation energy from the red dashed line connecting a-Ta_2O_5 and a-Ta. In other words, the free energy of mixing is referenced to the amorphous Ta_2O_5 and Ta phases at 0 K. Image reproduced with permission from ref.[51]. Copyright 2024. 48

Figure 3.13: Free energy curve fitted from DFT free energy points at 300ºC and corresponding oxygen chemical potential. (a) The DFT enthalpy (free energy at 0K) points are fitted by the enthalpy component of the regular solution model. (b) The entropy points fitting is based on a modified entropy component of the regular solution model. (c) DFT free energy points at 300ºC and modified regular solution model based on enthalpy component of (a) and entropy component of (b). (d) Chemical potential of oxygen and tantalum is calculated from the slope of the Gibbs free energy of $TaO_{2.5x*}$ and then divided by the number of oxygen atoms in a unit cell (2.5). Chemical potential of tantalum is calculated from the intercept of the Gibbs free energy of $TaO_{2.5x*}$ at Ta side. Image reproduced with permission from ref.[51]. Copyright 2024...50

Figure 3.14: Phase-field simulation of $Ta_2O_5/TaO_{1.5}$ shows it converges to a single layer with ~$TaO_{1.9}$ (35 at% Ta). Image reproduced with permission from ref.[51]. Copyright 2024. 50

Figure 3.15: (a-b) A simple ideal Fickian diffusion model based on $J = -D\nabla c$ for $Ta_2O_5/TaO_{0.7}$ (a) and Ta_2O_5/TaO (b) will yield a homogeneous depth profile. This ideal Fickian diffusion model contradicts the AES experiments in Figure 3.7. Image reproduced with permission from ref.[51]. Copyright 2024. 51

Figure 3.16: 2D Phase-field model for $Ta_2O_5/TaO_{0.5}$ device during retention. Retention simulations on pristine state, LRS (filament width = 5 nm) and HRS (filament gap = 0.3 nm) based on (a) Fickian diffusion, (b) modified Fickian diffusion that suppresses diffusion between the two layers, and (c) the phase separation model with calculated Gibbs free energy curve. Scale bar is 5 nm. These simulations are in broad agreement with the schemes shown in Figure 3.1, reproduced here; however, only (c) is consistent with the experimental results (Figure 3.3b). The simulated electronic conductance uses eqn. 4 and combines the bulk conductance (Table 2.1), interpolated in part (d), and the Poole-Frenkel model[50]. The scale bar is 5 nm. Image reproduced with permission from ref.[51]. Copyright 2024. 52

Figure 3.17: Origin of HRS and LRS Retention Failure with 2D Phase field model for $Ta_2O_5/TaO_{0.5}$ bilayer memristor. a-c) Retention measurement simulation on LRS and HRS with different filament gap and filament width. Scale bar is 5 nm. d) The simulated stability of LRS

and HRS as functions of the filament width and gap. Each circle represents one simulation that maps to the schematic shown in a, b, or c. e) The experimental retention results at 250 ºC using different RESET voltage (1.5 and 2.5 V). The inset shows a clear decrease in the HRS conductance upon baking for one hour, consistent with the predictions of (c). Image reproduced with permission from ref.[51]. Copyright 2024. 54

Figure 3.18: The critical parameters as functions of gradient energy penalty with 2D Phase field model for $Ta_2O_5/TaO_{0.5}$ bilayer memristor. The critical filament width and gap can be controlled using the gradient energy penalty in the simulation. Δf_{homo} is assumed to equal 0.1 eV/(Ta atom) based on the calculated difference in formation energy between the solid solution and the phase-separated convex hull in Figure 3.10a. Image reproduced with permission from ref.[51]. Copyright 2024.....55

Figure 3.19: Filament size and stability under different compliance currents. (a) Typical resistive switching behaviour of a device with a 1 mA compliance current. (b) Retention characteristics of devices from the pristine state, HRS, and LRS baked at 250 ºC. HRS devices failed to the low-resistance state. (c) Conductive Atomic Force Microscopy (C-AFM) in LRS devices with 1 mA compliance current shows a larger filament with a diameter ~8 nm. Scale bar is 20 nm. (d) Typical resistive switching behaviour of a device with a smaller 100 μA compliance current. (e) Retention characteristics of devices from the pristine state, HRS, and LRS baked at 250 ºC. LRS devices are unstable and fail during the retention measurement. (f) C-AFM maps in LRS devices with 100 μA compliance current show a smaller filament with diameter ~3 nm. Scale bar is 20 nm. See Figure 3.6 for all C-AFM images. Image reproduced with permission from ref.[51]. Copyright 2024. 56

Figure 3.20: Switching and retention properties of the bilayer TaO_X-based memristors using different RESET voltage. (a-c) Retention characteristics of devices from the pristine state, HRS, and LRS baked at 250 ºC with RESET voltage of (a) 1.5 V, (b) 2 V, and (c) 2.5 V. (d-f) Typical resistive switching behaviour with RESET voltage of (d) 1.5 V, (e) 2 V, and (f) 2.5 V. The 2V RESET shows that about half the devices failed after 48 hours. Image reproduced with permission from ref.[51]. Copyright 2024. 58

Figure 3.21: Results of the Simmons equation[74] with different calculated barrier heights. Based on the c-AFM results, we estimate the diameter of the filament to be 8 nm. The barrier should be less than half of the bandgap (~4 eV in Ta_2O_5). The average measured resistances of the HRS devices from Figure 3.17e are marked as horizontal dashed lines. Image reproduced with permission from ref.[51]. Copyright 2024. 58

Figure 4.1: Review of the literature on RRAM retention based on TaO_X[5,7,38,39] and HfO_X[36,55,78]. While it is difficult to obtain an activation energy in our work, our retention times are similar to past work which suggests an activation energy of around 1.5 eV (blue line). Our LRS retention failure time is much longer than previously reported because most work only identifies the state that fails faster (LRS or HRS). Image reproduced with permission from ref.[51]. Copyright 2024.....60

Figure 4.2: Ten orders of magnitude discrepancy between standard model and published experiment results. 61

Figure 4.3: Diffusion kinetics of TaO_X with ToF-SIMS and effects on retention failure. a) We develop a novel trilayer sample structure that embeds the ^{18}O tracer into the film stack, eliminating gas-phase reaction and enabling suboxide tracer diffusion measurements. b-c) Tracer diffusion results of Ta_2O_5 (b) and $TaO_{1.5}$ (c) trilayer samples. Black dotted line shows the fitted Fourier series solution to the diffusion equation. Sub-oxide $TaO_{1.5}$ shows much slower diffusivity compared with that of oxidised Ta_2O_5. d) Fitted activation energy of oxygen tracer diffusivity in TaO_X. Ta_2O_5 shows ~0.6 eV lower activation energy (E_A) than that of sub-oxides. The error indicates the 95% confidence error for the activation energy fits. **e)** Comparison of characteristic diffusion time with the vacancy diffusivity estimated from the tracer diffusion activation energy in ToF-SIMS experiments with experimental retention times. The diffusion time activation energy of sub-stoichiometric oxides match well with retention time of TaO_X devices from literature (light purple)[5,7,38,79]. Image reproduced with permission from ref.[51]. Copyright 2024. 62

Figure 4.4: ToF-SIMS results and fitting for tracer diffusivities of (a) Ta_2O_5, (b) $TaO_{1.5}$, and (c) $TaO_{0.7}$ at different temperatures. Image reproduced with permission from ref.[51]. Copyright 2024. 63

Figure 4.5: Simulated evolution in LRS and HRS devices with composition-dependent diffusion parameter. (a) The assumed composition-dependent oxygen diffusivity based on the tracer diffusion measurements in Figure 4.3. (b-d) The simulation of three different retention regions shows essentially identical results with that in Figure 3.17. Image reproduced with permission from ref.[51]. Copyright 2024. 64

Figure 4.6: Simulated evolution in LRS and HRS devices with composition-dependent diffusion parameters. (a) The composition-dependent oxygen diffusivity interpolated from the tracer diffusion measurements in Figure 4.3. (b) Simulation of Fickian diffusion model without suppressing oxygen transport at the interface. Here, the filament dissolves, in contrast to Figure 3.16a, because there is not enough time to equilibrate with the deeper metal-rich suboxide with low oxygen diffusivity. (c) The modified Fickian diffuison model suppresses oxygen transport between the two layers, and results in the rapid failure of the LRS state, consistent with Figure 3.16b. (d) Like Figure 3.16c, only the regular solution phase separation model can predict the stability of the LRS and the failure of the HRS. Image reproduced with permission from ref.[51]. Copyright 2024. 65

Figure 5.1: Binary switching and retention behaviors of ECRAM devices. (a) Schematic depicting the structure of the ECRAM device, featuring a stacked configuration of TaO_X/YSZ/Ta. This design utilizes an electric field to facilitate the movement of oxygen ions through the YSZ electrolyte, effectively modulating the oxygen concentration in the TaO_X channel oxide to enable the storage of information through the creation of varying resistance states in the device. (b) Binary switching behavior from HRS to LRS with one pulse (2V, 1s) at 350°C showing a higher than 100 on/off ratio. (c) 50 cycle switching between LRS and HRS with minimal cycle-to-cycle variation. (d-e) The retention measurements of two resistance states at 400°C (d) and 600°C (e) for 24 hours without failure. (f) Retention times of various memory devices including our ECRAM with TaO_X, Pt nanogap devices[18], $Al_{0.7}Sc_{0.3}N$ ferroelectric capacitors[29,83], ReRAMs based on TaO_X[5], and ECRAMs utilizing TiO_X[9] and

WO_X[43], showcasing our device's exceptional performance of our device in data retention capabilities across these diverse technologies. 68

Figure 5.2: 50 cycle switching between LRS and HRS with minimal cycle-to-cycle variation across a broad temperature range, spanning from 200°C to 600°C. 70

Figure 5.3: Endurance tests of 10000 pulses at 400°C. 70

Figure 5.4: 50 cycle switching between LRS and HRS with ±2V 1s pulse across a broad temperature range, spanning from 300°C to 550°C. The device operated at 350-400°C shows the largest on/off ratio. 71

Figure 5.5: 50 cycle switching between LRS and HRS with ±2V 100ms pulse across a broad temperature range, spanning from 300°C to 600°C. Results from both 100 ms and 1 ms pulses demonstrate that the device operated at 350-400°C shows the largest on/off ratio. 71

Figure 5.6: Retention test over 24 hours at 450°C and 500°C. No significant change in conductance was observed in both LRS and HRS. 72

Figure 5.7: Field-directed migration and redistribution of oxygen ions showing the mechanism of switching and retention. (a-b) STEM (a), and the corresponding EDS mapping of O and Ta (b) in pristine devices. (c-d) STEM (c), and the corresponding EDS mapping of O and Ta (d) in LRS devices. (e-f) STEM (e), and the corresponding EDS mapping of O and Ta (f) in LRS device after 400ºC annealing for 12hr. (g–h) STEM (g), and the corresponding EDS mapping of O and Ta (h) in HRS devices. Scale bar: 20 nm. 74

Figure 5.8: Computed formation energy and chemical potential of amorphous tantalum oxideS1. (a) Free energy curve fitted from DFT free energy points at 300oC and (b) corresponding oxygen chemical potential. ~Ta ($\boldsymbol{\alpha}$) and TaO1.9 ($\boldsymbol{\beta}$) are identified as two stable phases in the amorphous tantalum-oxygen system. 75

Figure 5.9: Phase-field model of migration and redistribution of oxygen ions during switching and retention. (a-c) Simulation of conductance and tantalum concentration dynamics during switching (a), LRS retention (b), and HRS retention (c). (d) The corresponding concentration mapping of Ta at different times in (a-c). Scale bar, 10 nm. 77

Figure 5.10: Analog switching and retention characterizations of the ECRAM. (a) Linear and symmetric conductance update in an ECRAM using a series of up/down pulsing cycles of different pulse widths at 400ºC (100 pulses, ±8 V, 800 μs). (b) Retention test of >10 analog states over a wide switching window. 78

Figure 5.11: Analog behavior across a broad conductance range, spanning from µS to mS, demonstrating the device's potential for reliable analog switching in various computational tasks. 79

Figure 5.12: Analog switching at approximately 1 µS. This characteristic enables the device to be used for low energy-consumption computation. 80

Figure 5.13: Analog switching with different pulse widths. Conductance can be finely tuned by the applied pulses with different pulse widths.....81

Figure 5.14: Analog switching with different pulse amplitudes. The conductance change is linearly proportional to the pulse amplitude, which enables precise control with pulse width.....82

Figure 5.15: Analog switching with 8V pulse across a broad temperature range, spanning from 300°C to 550°C.....82

Figure 5.16: (a-g) Analog switching with 4V pulse across a broad temperature range, spanning from 250°C to 550°C. (h) Nonlinearity (α) factors for both potentiation and depression. When α is close to 1, the conductance modulation approaches ideal linearity. The analog switching exhibited better linear behavior at temperatures $\leqslant$ 400°C compared to those at $\geqslant$ 450°C.....84

Figure 5.17: Endurance test of 10000 pulses at 300°C for analog switching with 100 multistate. 85

List of Appendices

Appendix A: Thermodynamic Considerations of Amorphous Materials 93

Appendix B: Thermodynamic Origins of $J = -D\nabla c$ 96

Abstract

Resistive memory technologies, specifically Resistive Random Access Memory (ReRAM) and Electrochemical Random Access Memory (ECRAM), hold significant potential for revolutionizing post-digital electronics due to their scalability, low power consumption, and high retention. This dissertation explores the underlying thermodynamic principles and engineering aspects of these technologies, with a focus on amorphous tantalum oxide (TaOx) as a core material.

The study begins by addressing the challenges in ReRAM, particularly the formation and stability of conductive filaments driven by oxygen vacancy migration. Through a combination of electrical measurements, scanning probe microscopy, chemical spectroscopy, first-principles calculations, and phase-field modeling, it is revealed that the stability of these filaments is critically dependent on the thermodynamic stability of amorphous oxygen-rich and oxygen-poor compounds, which undergo composition phase separation. This phase separation significantly influences the retention performance of ReRAM, enabling much longer retention times than current models predict.

In addition, this dissertation delves into the concept of composition-dependent diffusion in ReRAM. It is demonstrated that the diffusion behavior of oxygen within the TaOx layer is not uniform but rather composition-dependent. By incorporating this variable diffusivity into retention simulations, the study successfully reconciles previously unexplained discrepancies between experimental results and theoretical predictions. This finding further enhances the understanding

of oxygen vacancy migration and retention stability in ReRAM, highlighting the need to account for compositional effects in the design of reliable memory devices.

Building on these findings, the dissertation extends the principles of phase separation to ECRAM, introducing a high-temperature stable ECRAM device utilizing amorphous TaOx. This device demonstrates reliable operation at temperatures up to 600°C, with both binary and multi-level switching capabilities. The ability to maintain stable performance under such extreme conditions is attributed to the controlled phase separation within the material, which stabilizes the conductive pathways against thermal degradation.

The insights gained from this research provide a framework for the predictive design of memory devices, emphasizing the importance of non-ideal thermodynamic interactions in the performance and reliability of next-generation non-volatile memory technologies. The combination of experimental and theoretical approaches used in this study contributes to the advancement of ReRAM and ECRAM, paving the way for innovations in high-performance memory systems suitable for demanding applications.

Chapter 1 Nonvolatile Memory

Non-volatile memory technologies are crucial for modern computing systems due to their ability to retain data without power[1]. Several types of non-volatile memory have emerged, each with unique mechanisms and applications (Figure 1.1).

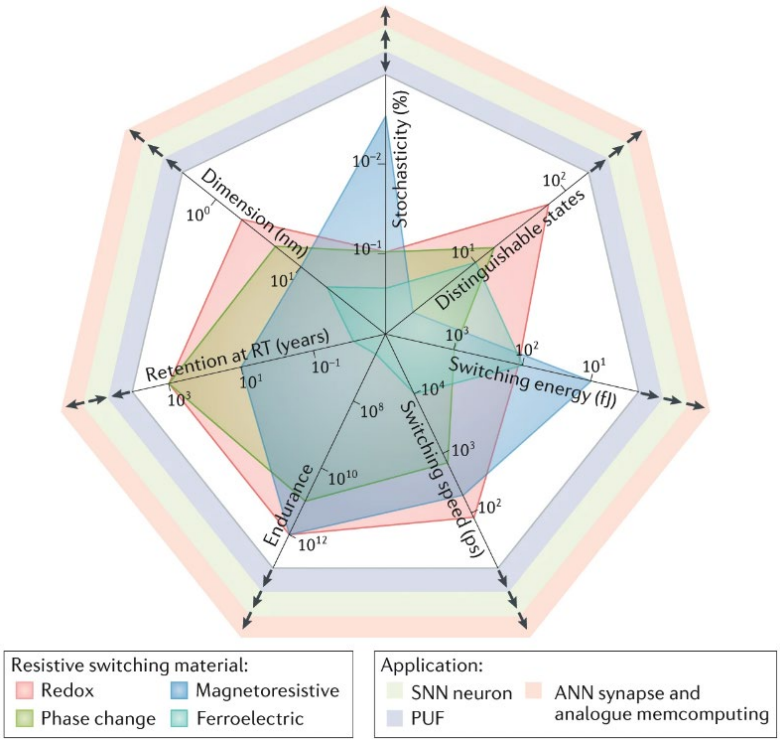


Figure 1.1: Properties of nonvolatile memories and application requirements[2]. Image reproduced with permission from ref.[2]. Copyright 2020.

Flash memory, widely used in consumer electronics, operates by trapping electrons in a floating gate to store data. Resistive random-access memory (ReRAM), based on resistive switching materials, stores data by changing the resistance states of a material, with applications in neuromorphic and in-memory computing. Phase-change memory (PCM) utilizes the reversible phase transition between amorphous and crystalline states in chalcogenide materials to store

information, offering high-speed and high-endurance performance. Magnetic random-access memory (MRAM) employs magnetic tunnel junctions to store data through the alignment of magnetic states, providing high endurance and fast switching speeds. Ferroelectric random-access memory (FeRAM) uses the polarization states of ferroelectric materials to represent data, offering low power consumption and high-speed operation. Each type of non-volatile memory addresses specific challenges and requirements in data storage and processing, making them integral to the advancement of next-generation computing architectures.

Here, we will mainly focus on one type of non-volatile memory: resistive memory. Leveraging the resistive switching properties of materials, resistive memory offers high-speed data storage, low power consumption, and scalability, making it ideal for applications in in-memory computing, neuromorphic computing, and high-temperature environments.

1.1 Resistive Memory

Resistive memory, a type of non-volatile memory, operates by leveraging the resistive switching properties of materials to store data[3]. This technology can be categorized into two-terminal and three-terminal resistive memories based on the number of terminals involved (Figure 1.2).

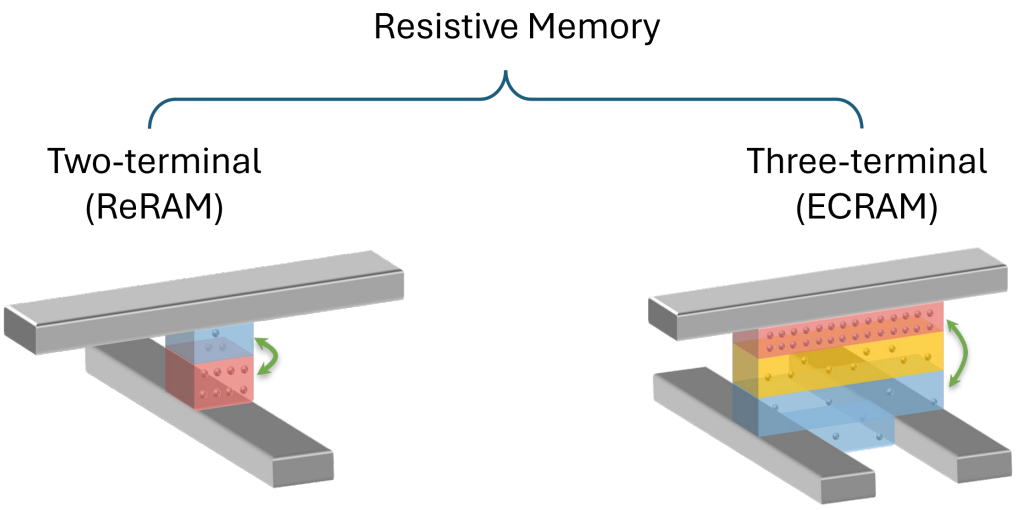


Figure 1.2: Category of Resistive memory based on the number of terminals involved.

1.1.1 Resistive Random Access Memory

Two-terminal resistive memory is also known as resistive random-access memory (ReRAM), with the potential to revolutionize future memory and computing technologies due to their high scalability, low power consumption, and excellent compatibility with complementary metal oxide semiconductor (CMOS) technology[4]. ReRAM consists of a thin film of metal oxide or other materials sandwiched between two electrodes. When a voltage is applied across these electrodes, the material undergoes a change in its resistance state, which can be toggled between a high resistance state (HRS) and a low resistance state (LRS). This change in resistance is non-volatile, meaning it retains its state even when the power is turned off, allowing data to be stored permanently. The switching process is typically attributed to the formation and rupture of conductive filaments or the migration of ions within the material. ReRAM can be broadly classified into cation-based and anion-based types (Figure 1.3), depending on the nature of the mobile species that induce resistive switching[3].

Cation-based ReRAM involves the migration of metal cations (such as silver or copper) within the dielectric layer. When a voltage is applied, these cations migrate and form metallic

filaments, creating a conductive path and switching the device to a low resistance state. Reversing the voltage causes the dissolution of the metallic filaments, returning the device to a high resistance state. Cation-based ReRAM typically exhibits fast switching speeds and good endurance.

Anion-based ReRAM, on the other hand, relies on the movement of anions, such as oxygen ions or vacancies, within the oxide layer. The creation and annihilation of conductive filaments composed of oxygen vacancies lead to resistive switching. This type of ReRAM is particularly valued for its stability and retention characteristics.

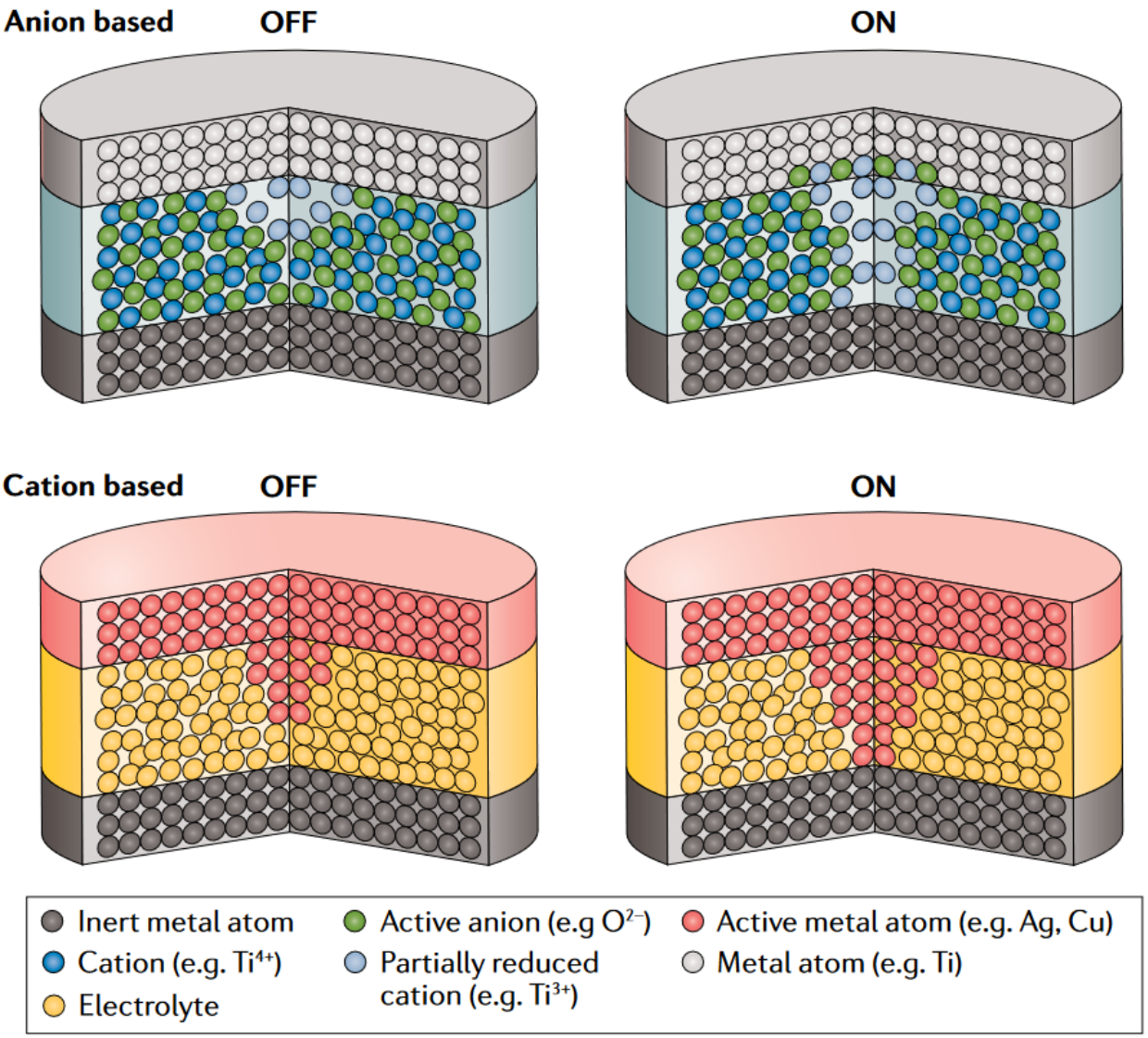


Figure 1.3: Illustration of an filament in the OFF state (HRS) and ON state (LRS) in an anion-type (top) and cation-type (bottom) ReRAM device[2]. Image reproduced with permission from ref.[2]. Copyright 2020.

Oxygen vacancies based ReRAM is a prevalent form of anion-based ReRAM, leveraging the movement and redistribution of oxygen vacancies within metal oxides, such as tantalum oxide (TaOx)[5] or hafnium oxide (HfOx)[6,7], to achieve resistive switching. When a voltage is applied, oxygen ions migrate, creating oxygen vacancies that form a conductive filament within the oxide layer, switching the device to a low resistance state. Reversing the voltage causes the oxygen ions to return, disrupting the filament and restoring the high resistance state. This type of ReRAM is

known for its robust retention, meaning it can maintain its resistance state for extended periods without power, which is crucial for reliable data storage. Additionally, oxygen vacancies-based ReRAM offers high endurance, capable of sustaining billions of switching cycles, making it suitable for applications that require frequent read/write operations.

1.1.2 Electrochemical Random Access Memory

Three-terminal resistive memory, also known as electrochemical random-access memory (ECRAM), involves a three-layer structure comprising an active material, an electrolyte, and electrodes (Figure 1.4)[8–11]. When a voltage is applied across the electrodes, ions from the electrolyte migrate into or out of the active material, causing a reversible change in its resistance. This ion migration process alters the electronic properties of the active material, allowing it to switch between different resistance states. This mechanism is analogous to traditional battery chemistry but on a much smaller, faster, and more reversible scale, making ECRAM suitable for high-speed and low-power applications.

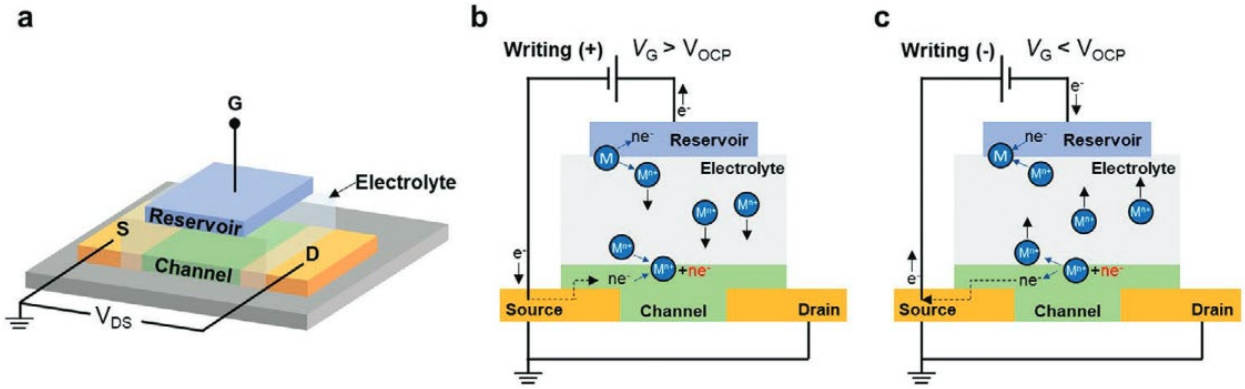


Figure 1.4: Device structure and operation principle of a ECRAM device based on cation intercalation[10]. Image reproduced with permission from ref.[10]. Copyright 2023.

ECRAM devices can be classified based on the type of ions used for electrochemical switching. Proton-based ECRAM utilizes hydrogen ions (protons) as the mobile species[12]. Protons are inserted into or extracted from the active material through an electrolyte under an applied

voltage, changing the material's resistance. Proton-based ECRAM benefits from fast ion mobility, enabling rapid switching speeds and low operating voltages, which are advantageous for energy-efficient memory applications. Lithium-based ECRAM operates using lithium ions[13]. Similar to lithium-ion batteries, lithium ions are inserted into or extracted from the active material, such as lithium cobalt oxide or other lithium-intercalating compounds, to modulate its resistance.

Oxygen vacancy based ECRAM leverages the migration and redistribution of oxygen vacancies within an oxide material to achieve resistive switching. In these devices, an external voltage drives the movement of oxygen ions, creating or annihilating oxygen vacancies in the active layer, such as titanium oxide (TiOx)[9] or tungsten oxide (WOx)[8]. The concentration and distribution of these vacancies directly affect the material's resistance state. Oxygen vacancies based ECRAM is particularly notable for its reliable switching characteristics and excellent compatibility with CMOS technology. Compared with proton and lithium ion based ECRAM, oxygen vacancies based ECRAM offers a significant advantage in terms of retention. This type of ECRAM can maintain its resistance state for extended periods without power due to the slow diffusion of oxygen vacancies, which have a relatively large ionic size. However, this same property can result in slower switching speeds. Additionally, the use of oxygen vacancies in oxide materials enables high-density memory integration, making it a strong candidate for advanced applications in high-performance computing and data storage.

1.2 Application

Resistive memory, a promising non-volatile memory, has garnered significant attention for its diverse functionalities (Figure 1.5). The von Neumann bottleneck, a limitation of traditional computer architectures, arises from the data transmission between computing units and memory, leading to inefficiencies[14]. To mitigate this bottleneck, several non-von Neumann architectures

with next-generation memory technologies have been proposed[15]. One such approach is in-memory computing, where resistive memory allows data processing to occur directly within the memory cells, significantly reducing data transfer bottlenecks and improving computational speed and energy efficiency[16]. Another approach is neuromorphic computing, in which resistive memory mimics the synaptic functionalities of the human brain, enabling the development of energy-efficient and highly parallel computing architectures[17]. These applications are particularly valuable for advancing artificial intelligence and machine learning by facilitating more efficient data processing and storage.

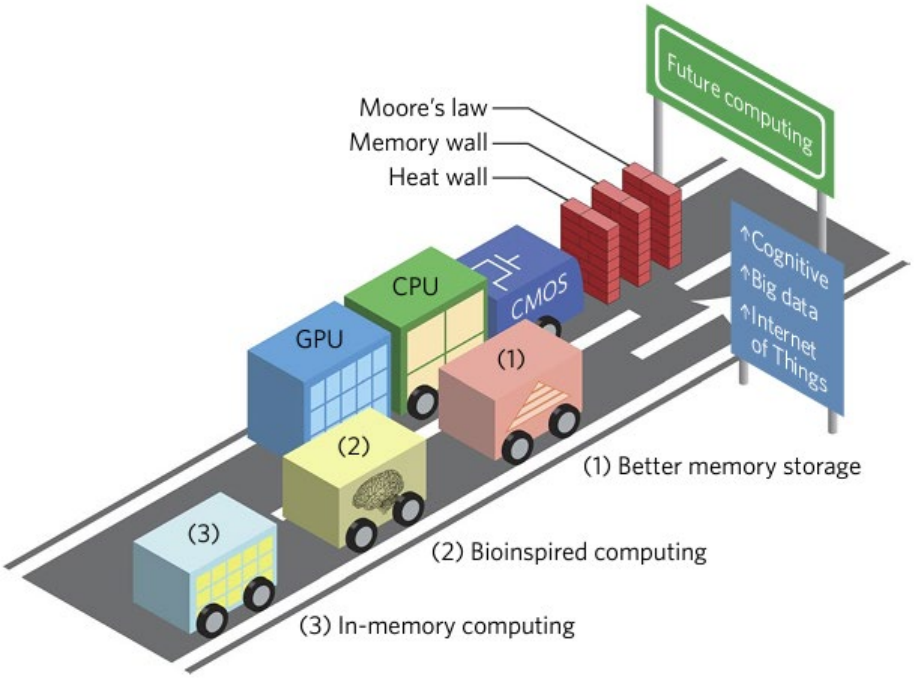


Figure 1.5: The race towards future computing solutions[14]. Image reproduced with permission from ref.[14]. Copyright 2018.

Furthermore, resistive memory can serve as traditional memory in various electronic devices, offering benefits such as faster read and write speeds, lower power consumption, and higher endurance compared to traditional flash memory. Compared with traditional memory based on silicon technology, resistive memory's robust performance at high temperatures makes it ideal

for use in harsh environments, such as aerospace, automotive, and industrial applications, where conventional memory technologies may fail[18]. By leveraging the resistive switching properties of materials, resistive memory provides a versatile and reliable solution for a wide range of cutting-edge technological applications.

1.2.1 Neuromorphic Computing

Memristors, short for “memory resistor”, was first theoretically proposed in 1971 by Leon Chua[19]. In this groundbreaking work, Chua postulated the existence of a fourth fundamental passive circuit element, alongside the resistor, capacitor, and inductor. The memristor is characterized by its ability to retain a history of the electrical charge that has passed through it, effectively "remembering" its past states. In 2008, HP Labs connected the concept of memristors with experimentally observed ReRAM devices[20]. Since then, their application in non-von Neumann computing paradigms, particularly neuromorphic computing, has been extensively explored. In these neuromorphic systems, memristors often serve as compact synaptic elements, facilitating learning and memory in neural networks. The device-level synaptic plasticity achievable with memristors fundamentally determines the functionality of these networks. Various synaptic functions have been emulated using memristors, such as spike-timing-dependent plasticity[21], paired pulse facilitation[22], and heterosynaptic plasticity[23].

It is important to note that the requirements for device characteristics in neuromorphic computing differ significantly from those in nonvolatile memory applications, particularly regarding the number of analog states that can be reliably accessed during resistive switching.

1.2.2 High-temperature Memory

The operational components in high-temperature extreme environments, typically beyond the standard commercial temperature range (0°C to 85°C) and the military-specification range (−55°C to +125°C), are critical in several key sectors, including aerospace electronics, energy exploration, and automotive electronics[24]. Within these sectors, the robust functioning of electronic systems at elevated temperatures, particularly in the range of 200°C–300°C and extending up to 600°C in specific applications, is a significant challenge[25]. A crucial aspect of these systems is the performance of logic and memory units. While advancements in high-temperature logic units have been achieved through wide bandgap semiconductors (e.g. Silicon Carbide (SiC)[26] & Gallium Nitride (GaN)[27]) and carbon nanotubes[28], the development of memory units for such extreme conditions has been more challenging. Current emerging memory technologies, including ReRAM based on Pt nanogaps operational at 600 °C[18] and nitride-based ferroelectric capacitors at 400 °C[29], exhibit limitations such as large cycle-to-cycle variations, destructive read, and high operational constraints (60V operational voltage).

1.3 Device Fabrication

The ReRAM devices in this work have a cross-point area of ~1.5 × 1.5 μm^2 and are fabricated on SiO_2 (500 nm)/Si substrates in the Lurie Nanofabrication Facility (LNF) at the University of Michigan, following our previous work[23]. First, a 35 nm bottom Pd electrode with 5 nm NiCr adhesion layer is deposited by photolithography (1500/4000 rpm PMGI SF6/SPR220-3 μm photoresist with GCA AS200 AutoStep), electron beam evaporation (Angstrom Engineering Evovac Evaporator), and lift-off processes (Remover PG and Isopropanol) as shown in Figure 1.6. Next, a 30 nm $TaO_{0.5}$ reservoir layer is deposited by direct current (DC) reactive sputtering with a Kurt J. Lesker Lab 18 system using a 51 mm diameter Ta metal target, a power of 200 W for 150s, and a setpoint temperature of 400°C. The sputter pressure was 5 mTorr, and the gas was an Ar/O_2

mixture at a ratio of 32:1. Next, the sputter chamber was cooled to room temperature, and a 4 nm Ta_2O_5 switching layer is then deposited by radio frequency (RF) sputtering using a 51 mm diameter Ta_2O_5 target in Ar gas with a pressure of ~5 mTorr and a power of 30 W for 1059s. A 30/30 nm Au/Pd top electrode is then deposited by photolithography, e-beam evaporation, and lift-off processes. This top electrode also acts as a hard etch mask for the two tantalum oxide layers. A reactive ion etching process using SF_6 (Plasmatherm 790) is used to etch the two tantalum oxide layers to expose the bottom contacts. A third photolithography process is used to deposit a larger (150 by 150 μm^2), 200/10 nm Au/Ni pad by electron beam evaporation, which is used to contact the probe station.

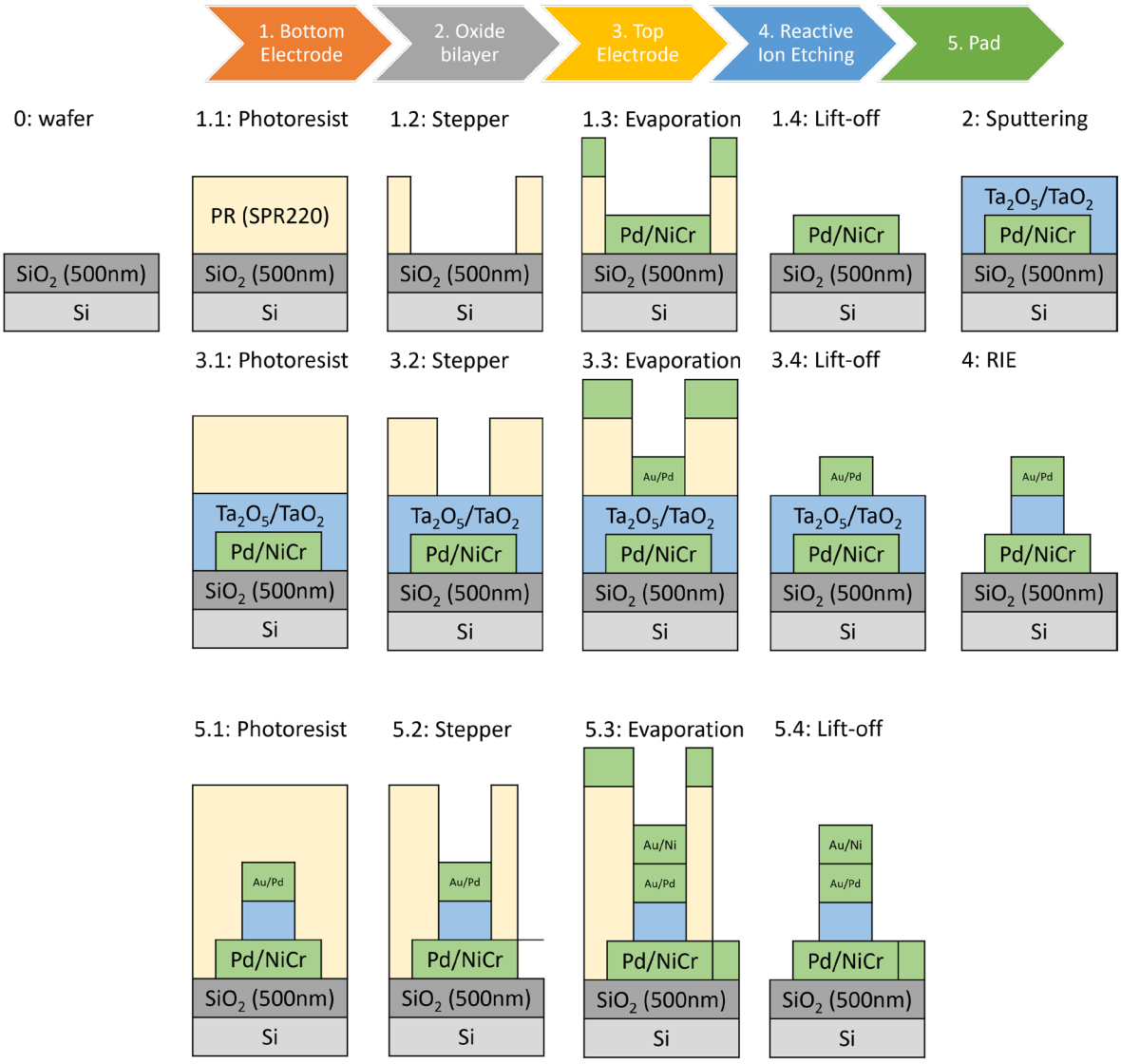


Figure 1.6: Illustration of ReRAM fabrication workflow.

The ECRAM devices comprising thin-film YSZ were fabricated by employing shadow masks to delineate the bottom 5 nm Ta and 20 nm Pt contacts on a Si/SiO_2 substrate. Successive layers of TaO_X switching layer (DC-reactive), YSZ electrolyte (RF), and Ta gate layer (DC-reactive) were sputtered using shadow masks. Utilizing an AJA Orion-8 sputter system, 20 nm of TaO_X was sputtered onto bottom contacts employing a 3-in. Ta target (99.95% purity) from Plasmaterials (Livermore, CA), operating at a target power of 100 W with a sputter gas mixture of $Ar:O_2$ at a 37:3 ratio regulated by mass flow controllers. The sputter gas pressure was maintained

at 5 mtorr, with a substrate-to-target distance of approximately 15 cm. The 140 nm YSZ electrolyte was grown by RF sputtering on a 3-in. YSZ target (8 mol% Y_2O_3 in ZrO_2, Plasmaterials LLC) using a sputter power of 150 W and 5 mtorr of pure argon. The 20 nm Ta gate layer was grown by DC sputtering on a 3-in. Ta target is using a sputter power of 100 W and 5 mtorr of pure argon. Next, 30-nm-thick gate Pt current collectors were sputtered using a 2-in. Pt target at 3 mtorr of pure argon with a gate electrode shadow mask. No additional annealing was performed during the room temperature sputtering process. Finally, for environmental protection against oxidation, a 60 nm Si_3N_4 layer was deposited on the ECRAM device's channel side using plasma-enhanced chemical vapor deposition (PECVD) at 200°C in the Lurie Nanofabrication Facility via a Plasmatherm 790.

1.4 Electrical Characterization

1.4.1 Switching

The ReRAM devices were characterised using a Keithley 4200 semiconductor parameter analyser with a probe station. The voltage is applied to the top electrode and the bottom electrode is grounded during electrical measurements. A compliance current of 1 mA and -5 V stop voltage was set during electroforming. After electroforming, we switch the device 20 times between the high-resistance and low-resistance states by I-V sweeps.

Following fabrication, the ECRAM underwent testing in a custom-built, six-probe Nextron MPS-Ceramic Heater CHH750 probe station, where the two channel electrodes made direct contact with Rh probes. The gate current collector contacted a Si substrate with 50 nm of Pt, while the Rh probe interfaced with the Pt. The environment was meticulously regulated by flowing 5N ultra high-purity Ar at a controlled rate of 87 sccm using an Omega mass flow controller. A Swagelok check valve maintained chamber pressure at ≈50 torr above ambient, effectively

preventing air backflow. Monitoring with a Zirox ZR5 oxygen sensor indicated an Ar flow gas oxygen concentration of about 3 parts per million. Notably, the flowing Ar proved more efficient in forming thermal contact between the heater and chip compared to vacuum techniques. Device measurements were conducted utilizing a Bio-logic SP300 bipotentiostat or a National Instruments Data Acquisition Device (DAQ-6358) system.

1.4.2 Endurance

Endurance is a critical parameter in non-volatile memory technologies such as ReRAM and ECRAM. It refers to the ability of the memory device to undergo numerous read-write cycles without significant degradation in performance. High endurance is essential for ensuring the reliability and longevity of memory devices in various applications, from consumer electronics to industrial systems and advanced computing architectures.

In ReRAM, endurance is primarily influenced by the repeated formation and dissolution of conductive filaments within the metal oxide layer. These filaments, composed of oxygen vacancies or metal ions, switch the device between high resistance (HRS) and low resistance (LRS) states. Each switching cycle subjects the material to electrical stress, which can lead to the gradual degradation of the switching layer. Factors such as the composition of the metal oxide, the quality of the electrodes, and the control of filament formation significantly impact the endurance of ReRAM devices.

ECRAM devices operate based on the reversible insertion and extraction of ions into an active material, modulating its resistance state. The endurance of ECRAM is determined by the ability of the device to sustain numerous ion insertion and extraction cycles without significant loss of performance. This involves ensuring that the electrolyte and electrode materials can withstand repeated ion movement without degradation. Key factors affecting ECRAM endurance

include the stability of the electrolyte, the robustness of the electrode materials, and the control of ion diffusion pathways. Enhancing endurance in ECRAM involves optimizing these materials and interfaces to minimize degradation and maintain consistent switching behavior over extended cycles.

1.4.3 Retention

Retention performance is a critical attribute of non-volatile memory technologies, determining how long data can be reliably stored without power. ReRAM, which operates by changing the resistance states of metal oxides through the formation and rupture of conductive filaments or migration of oxygen vacancies, typically offers robust retention capabilities. These resistance states are stable and can retain data for over ten years under optimal conditions. ECRAM, on the other hand, relies on electrochemical reactions to modulate the resistance states of the memory cell. The retention performance of ECRAM is determined by the open circuit voltage of the ionic configurations within the switching and reservoir layers. Due to the reversible nature of ion migration and redox reactions, ECRAM can only achieve short retention times.

For ReRAM retention measurement, we SET some devices on the die into the LRS, while we RESET others into the HRS. The pristine devices did not undergo any electroforming, setting, or resetting. The die was annealed in an Everbeing CG-196 environmentally-controlled probe station under ~ 300 Torr of ultra-high purity Ar. No electrical measurements were taken at elevated temperatures. After cooling the device to room temperature, we measure the conductance of each device using a small probing voltage of 0.1 V with the Keithley 4200. Each die was only annealed at one temperature; because it was annealed and measured several times, and the total annealing time is recorded.

1.5 Device Characterization

1.5.1 Transmission Electron Microscopy

Scanning transmission electron microscopy (STEM) is a type of transmission electron microscopy (TEM) in which the electron beam is focused to a fine spot for high-resolution imaging. I utilized Z-contrast annular dark-field (ADF) imaging and spectroscopic mapping with STEM, combined with energy dispersive X-ray (EDX) spectroscopy, to visualize the changes in oxygen ion distribution across different resistance states of ECRAM. This approach allowed for detailed analysis of how oxygen ions contribute to the switching mechanisms and retention performance of the memory device.

STEM measurements at the University of Michigan were taken using a Thermo Fisher Talos F200X G2, a 200 kV FEG scanning transmission electron microscope operated in STEM mode. The Velox software was used for STEM images and EDS data acquisitions. The TEM specimen was prepared using a Thermo-Fisher Helios 650 Xe Plasma FIB. The final beam condition was set at 12 keV 10 pA for the liftout polishing.

1.5.2 Conductive Atomic Force Microscopy

Conductive atomic force microscopy (c-AFM) is a mode of atomic force microscopy (AFM) that measures the electric current flow at the contact point between the tip and the surface of the sample when applying voltage. I utilized c-AFM to visualize the changes in the shape of conductive filaments across different resistance states (pristine, LRS, HRS) and before and after retention. The workflow includes sample preparation, which involves removing the top electrode, followed by the c-AFM measurement process (Figure 1.7). This technique allowed for detailed

observation of how the conductive filaments evolve during the device's operation and retention process.

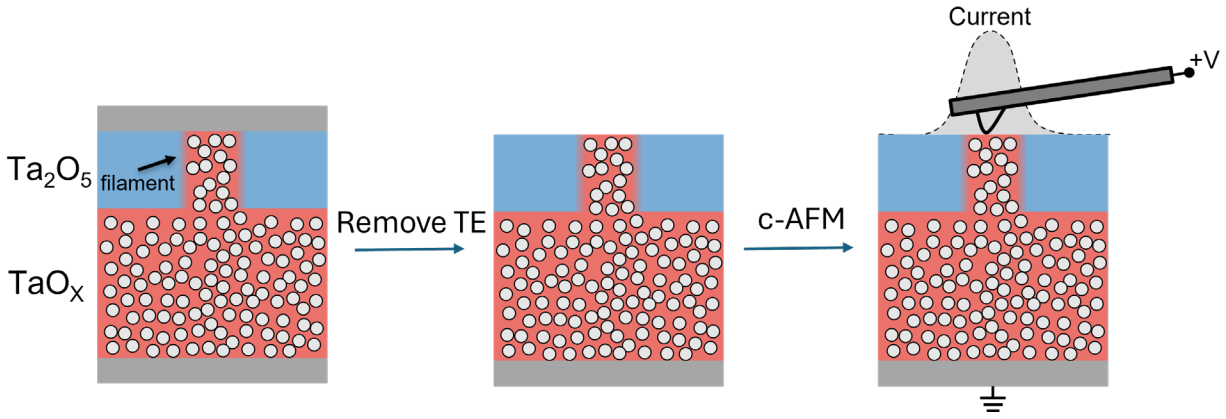


Figure 1.7: Illustration of c-AFM measurement on ReRAM device with LRS after removing top electrode.

The Au/Pd top electrode of TaO_X ReRAM is removed by 9 min Ar ion beam sputtering with an AJA Orion-8 Sputter System at room temperature. The gas pressure was 5 mTorr while the RF power was 50 W. The etching time is estimated by the etch rate of Au/Pd is ~7 nm/s and that of Ta_2O_5 ~2 nm/min.

The conductive AFM was done using the NT-MDT Ntegra Prima microscope with platinum-coated tips (MikroMasch, HQ:CSC37/Pt) and diamond-coated tips (Nanosensors, DT-NCHR), operated in contact mode. The conductive tip was grounded while the sample was biased with a constant voltage (0.5 V) through the conductive bottom electrode. The topography information and the current value were tracked simultaneously for constructing the electric current mapping.

For all samples, we initially scan a $(3\ \mu m)^2$ area with 256 × 256 pixels with a constant 0.5V. This enables us to localise the filaments in the LRS and HRS samples. To measure the size of the filament, we then conduct a $(500\ nm)^2$ scan area around the filament with 256 × 256 pixels with 0.5V. The diameter of filaments are determined by counting the total number of pixels with a

current higher than 1nA under a circular assumption in the $(500\ nm)^2$ scan area measurement. Each pixel is taken to equal $(1.95\ nm)^2$.

Chapter 2 Diffusion

2.1 Diffusion

Diffusion is a fundamental process that describes the movement of particles from regions of high concentration to regions of low concentration, driven by concentration gradients (Figure 2.1a). This natural tendency towards equilibrium plays a crucial role in various scientific and industrial applications, from biological systems and chemical reactions to materials engineering and environmental science. The principles of diffusion are governed by Fick's laws, which provide a mathematical framework for understanding how particles distribute themselves over time. In more complex systems, diffusion can interact with other phenomena, such as phase separation, where a homogeneous mixture separates into distinct phases, leading to intricate patterns and structures (Figure 2.1b). Understanding diffusion and its various manifestations is essential for advancing technologies and optimizing processes across multiple disciplines.

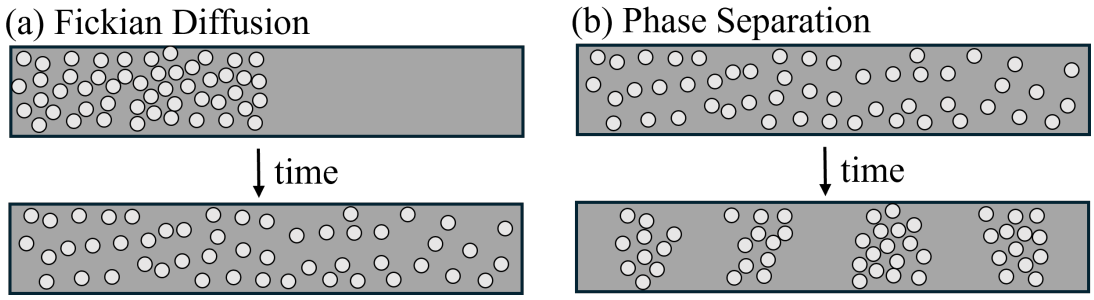


Figure 2.1: Schematic illustrating (a) Fickian diffusion and (b) phase separation.

2.1.1 Fickian Diffusion

Fickian diffusion, governed by Fick's laws, describes the process of particle movement from regions of high concentration to regions of low concentration, driven by concentration

gradients. Fick's First Law states that the flux of particles is proportional to the concentration gradient. Fick's Second Law describes the time dependence of diffusion, predicting how the concentration of particles changes over time.

In Fickian diffusion, the primary driving force is the concentration gradient, leading to linear transport where the flux of particles is directly proportional to the concentration gradient. Over time, the system approaches equilibrium, with the concentration becoming uniform throughout. This diffusion process is predictable and uniform under constant conditions. Fickian diffusion is commonly observed in gases, such as gas exchange in the lungs; in liquids, like the diffusion of solutes; and in solids, including heat transfer and impurity diffusion in materials. The predictability and uniformity of Fickian diffusion make it a fundamental process in understanding various natural and industrial phenomena.

2.1.2 Phase Separation

In contrast, phase separation involves more complex dynamics that cannot be captured by Fickian diffusion. Phase separation occurs when a homogeneous mixture becomes unstable and segregates into distinct regions with different compositions or phases. This process is driven by the system's tendency to minimize its free energy and can proceed through mechanisms like nucleation and growth or spinodal decomposition.

The generalized diffusion equation that can describe phase separation is the Cahn-Hilliard equation. This equation accounts for both the diffusion of particles and the free energy landscape of the system. This generalized diffusion equation, particularly the Cahn-Hilliard equation, effectively models the dynamics of phase separation, including the formation of interfaces and the evolution of microstructures over time. It captures the complex interplay between diffusion and

thermodynamics, enabling the study of phenomena such as spinodal decomposition, where a homogeneous mixture separates into distinct phases without a nucleation barrier.

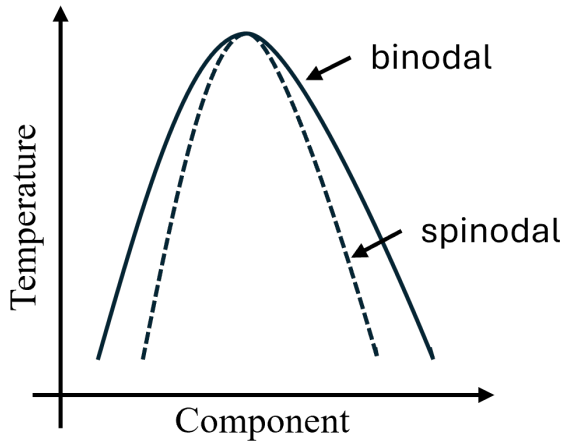


Figure 2.2: Phase diagram, governed by thermodynamic variables, has guided strategies for controlling materials microstructure. The discovery of spinodal decomposition (dotted line) introduced a new understanding beyond nucleation and growth below the binodal line.

Phase separation is a well-known and highly useful phenomenon, playing a critical role in various scientific and industrial processes. Phase separation occurs when a homogeneous mixture becomes unstable and separates into distinct regions with different compositions or phases. This process is driven by the system's tendency to minimize its free energy (Figure 2.2). It is an evergreen subject that continually reinvents itself, starting early on when scientists and engineers sought to control items such as steel microstructure and to understand everyday occurrences like why oil floats on water[30]. In the 19th and early 20th centuries, research focused on nucleation and growth, but a significant surprise came with the identification of spinodal decomposition. This discovery led to an era of exploring spinodal decomposition formalism in many manifestations, a pattern that continues to some extent today.

Despite its widespread familiarity, the opportunities to manipulate phase separation are surprisingly subtle and complex, involving intricate interactions at the molecular and macroscopic levels. Understanding and controlling phase separation requires a deep knowledge of

thermodynamics, kinetics, and material properties, as well as sophisticated techniques to influence these parameters. The ability to finely tune phase separation can lead to significant advancements in fields such as materials science, biotechnology, and chemical engineering, enabling the development of new materials with tailored properties, improved drug delivery systems, and more efficient separation processes. The challenges in manipulating phase separation lie in the precise control of factors such as temperature, concentration, and external fields, which can lead to a wide range of outcomes from homogeneous mixtures to distinct phases with unique characteristics.

2.2 Material System

Resistive memory leverages a variety of materials to achieve its resistive switching properties, each offering unique benefits and challenges. Common materials used in ReRAM include transition metal oxides (Figure 2.3) like titanium dioxide (TiO_2)[31,32], tungsten oxide (WO_3)[33–35], hafnium dioxide (HfO_2)[36,37], and tantalum oxide (Ta_2O_5)[38,39]. These materials are chosen for their ability to undergo reversible resistance changes when subjected to an electric field, driven by mechanisms such as the formation and rupture of conductive filaments or the migration of oxygen vacancies. Other materials like perovskites and chalcogenides are also explored for their distinct switching behaviors and potential to enhance device performance. The selection of materials significantly influences the memory device's characteristics, including switching speed, endurance, retention, and scalability, making material engineering a critical aspect of ReRAM development.

Tungsten oxide (WOx) is one significant material used in ReRAM and ECRAM due to its versatile switching properties and stability. In ReRAM applications, WOx typically undergoes resistive switching through the formation and dissolution of conductive filaments or the migration of oxygen vacancies. Its fast oxygen diffusion, multiple metastable states (“Magnéli phases” as

shown in Figure 2.3a)[40], and reliable switching, makes WOx a strong candidate for volatile memory devices. In ECRAM, WOx leverages its electrochemical properties, where the resistive states are modulated by different ion insertion and extraction (H^+, Li^+ and O^{2-}) within the material[41–43]. This capability allows WOx-based ECRAM devices to achieve efficient and reversible resistance changes, making them suitable for applications in neuromorphic computing and other advanced memory technologies. The dual utility of WOx in both ReRAM and ECRAM underscores its importance in the development of next-generation memory solutions.

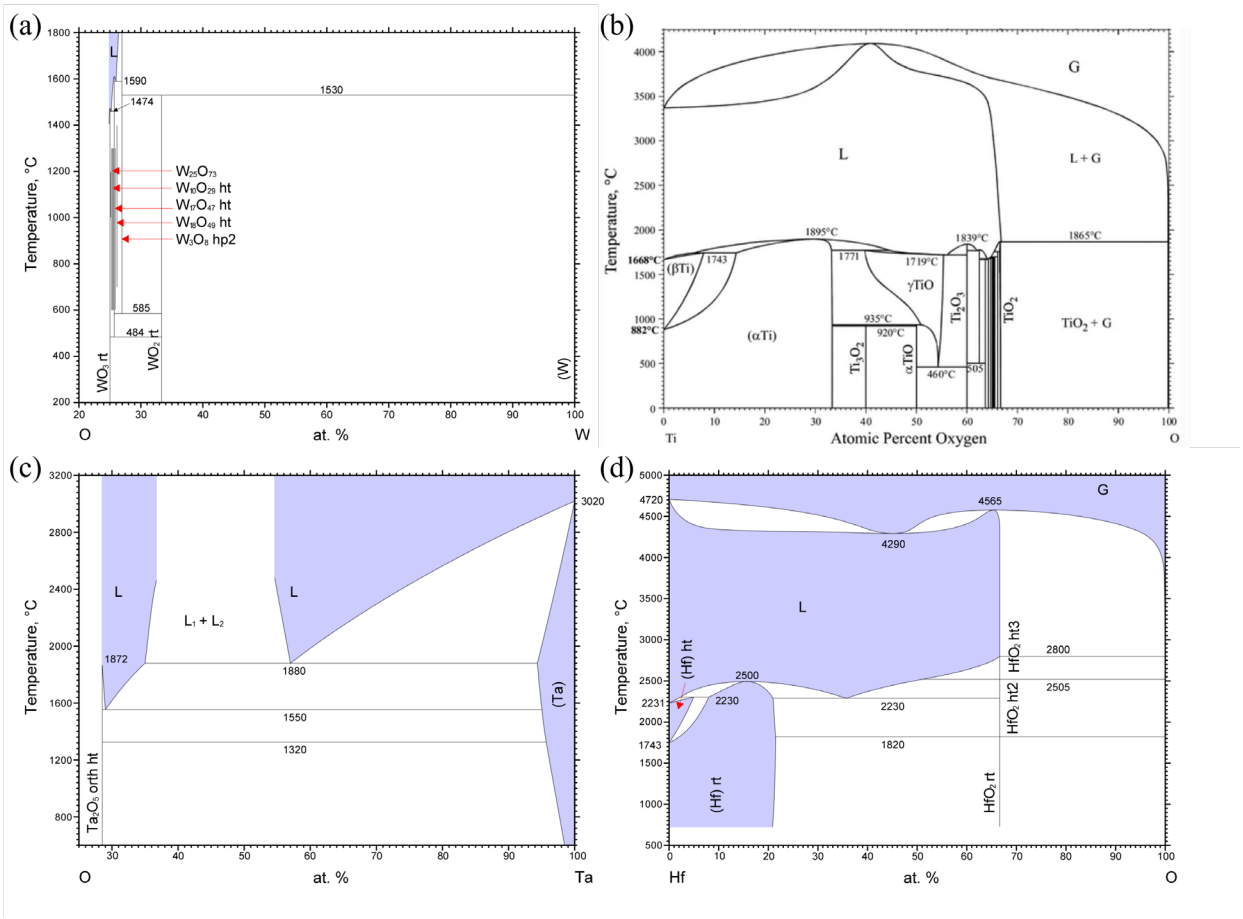


Figure 2.3: Phase Diagrams of four transition metal oxide systems, including of (a) Tungsten-Oxygen[40], (b) Titanium-Oxygen[44], (c) Tantalum-Oxygen[45], and (d) Hafnium-Oxygen[46].

Tantalum oxide (TaOx) is another particularly notable material in the realm of ReRAM due to its excellent switching properties and stability. In ReRAM devices, TaOx is typically used

in an amorphous form within a metal-insulator-metal structure where it serves as the active switching layer. The resistive switching in amorphous TaOx is often attributed to the formation and dissolution of conductive filaments composed of oxygen vacancies or metallic tantalum. These devices are known for their high endurance, often enduring billions of switching cycles, and strong retention characteristics, maintaining data integrity for over a decade. Additionally, amorphous TaOx offers good thermal stability, making it suitable for applications requiring reliable performance under varying environmental conditions. The precise control over the oxygen vacancy distribution and filament formation in TaOx is key to optimizing its performance, highlighting the material's potential in next-generation non-volatile memory technologies.

2.3 Diffusion in Resistive Memory

2.3.1 Fickian Diffusion in Resistive Memory

Fickian diffusion is a widely used concept in the semiconductor field, particularly in understanding and controlling the doping process. Doping involves introducing impurity atoms into a semiconductor material to modify its electrical properties, typically by creating regions of p-type or n-type conductivity. The diffusion of dopants, such as phosphorus, boron, or arsenic, into silicon substrates is governed by Fick's laws, which describe how these atoms move from regions of high concentration to low concentration. This process is crucial for forming the desired junction depths and concentration profiles in semiconductor devices. Precise control over dopant diffusion, achieved through techniques like thermal diffusion and ion implantation followed by annealing, is essential for optimizing device performance, ensuring consistent electrical characteristics, and improving yield in semiconductor manufacturing.

In ReRAM, Fickian diffusion plays a significant role in the behavior of oxygen vacancies, particularly during retention. ReRAM devices rely on the formation and dissolution of conductive

filaments composed of oxygen vacancies within a metal oxide layer, such as TaOx or HfOx. During retention, the stability of these filaments is crucial for maintaining the stored data. Fickian diffusion describes how oxygen vacancies can migrate within the oxide layer due to concentration gradients, potentially leading to changes in the resistance state of the device over time. Understanding and controlling this diffusion process is vital for enhancing the retention performance of ReRAM, ensuring that the memory state remains stable without power for extended periods. Advanced material engineering and optimization of the oxide layer composition are often employed to minimize undesirable vacancy migration and improve data retention.

ECRAM also heavily relies on diffusion processes, particularly the movement of ions during switching and retention. ECRAM devices function by modulating the resistance of an active material through the reversible insertion and extraction of ions, such as lithium or protons, facilitated by an electrolyte. During the switching process, ions migrate according to Fickian diffusion principles, moving from regions of high concentration in the electrolyte to lower concentrations within the active material. This ion movement changes the electronic properties of the material, thereby altering its resistance state. Similarly, during retention, the stability of the ions' positions is critical for maintaining the stored information. Fickian diffusion helps in understanding how ions might gradually diffuse back towards equilibrium positions, potentially affecting the device's retention performance. Strategies to enhance retention often involve optimizing the electrolyte composition and engineering the electrode interfaces to reduce unwanted ion migration, thereby ensuring stable and reliable memory operation over time.

Fickian diffusion is a foundational concept in understanding and optimizing various processes in advanced memory and semiconductor technologies. In semiconductor doping, it provides insights into the precise control of impurity profiles, essential for device performance. In

ReRAM, it explains the behavior of oxygen vacancies during retention, while in ECRAM, it describes the movement of ions during switching and retention.

2.3.2 Phase Separation in Resistive Memory

The phase separation in ReRAM during switching, particularly in TaOx-based devices, involves the formation and dissolution of conductive filaments driven by thermal gradients and ion migration. According to the study by Ma et al.[47], the electroformation process begins with the application of voltage, leading to the formation of a small-diameter hotspot due to current constriction and Joule heating (Figure 2.4). This creates a significant temperature gradient, which drives the lateral migration of ions, notably tantalum (Ta) and oxygen (O). The high-angle annular dark-field microscopy (HAADF) and X-ray energy-dispersive spectroscopy (EDS) analyses revealed an accumulation of tantalum ions in the core of the filament and a depletion in the surrounding ring, indicating a temperature-gradient-induced phase separation. This phenomenon, known as the Soret effect, results in a permanent change in the local composition, stabilizing the filament and enhancing the device's switching characteristics. The fine-scale intensity contrast observed within the filament further suggests the presence of phase-separated regions, critical for the device's long-term stability and performance. Understanding and controlling this phase separation is essential for optimizing the reliability and functionality of ReRAM devices.

This phase separation continues with repeated switching cycles, leading to a gradual increase in the filament's diameter and the further development of Ta-rich and O-rich areas. The instability of TaOx, driven by the tendency of the material to separate into stable Ta and $TaO_{2.5}$ phases, exacerbates this process, resulting in the continuous growth and evolution of the filament structure. The instability and phase separation within TaOx are critical factors affecting the endurance and reliability of ReRAM devices. As the devices undergo multiple switching cycles,

the filament's structure evolves, potentially leading to device failure modes such as stuck-in-low resistance state (LRS) or stuck-in-high resistance state (HRS) due to the formation of highly conducting or insufficiently conductive filaments, respectively. Understanding and controlling these phase separation dynamics are essential for optimizing the performance and longevity of TaOx-based ReRAM devices.

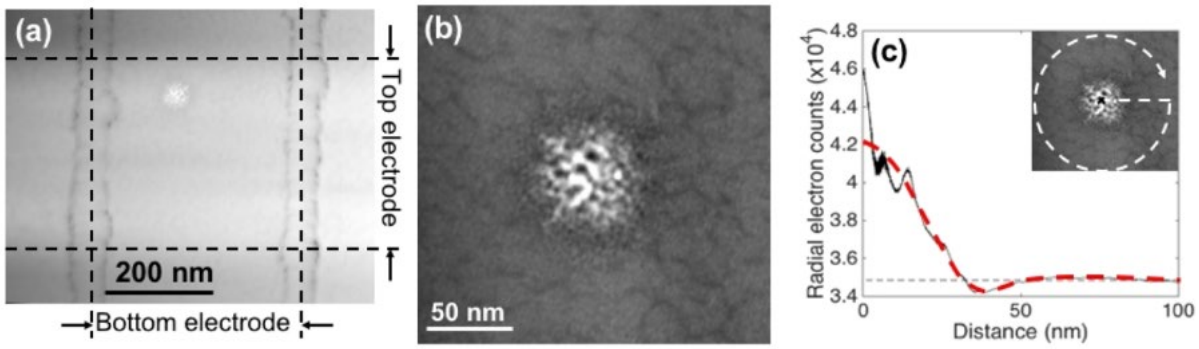


Figure 2.4: HAADF image of the active area of the TaOx device showing phase separation[47].

2.4 Phase-field Model

A phase-field model is a finite-element model for solving diffusion problems[48]. It can be used to diffusion dynamics, and phase separation[49]. Here, I used phase-field model to simulate the switching/retention behaviors in ReRAM and ECRAM devices.

The ReRAM device structure consists of 30 nm top electrode layer Pd (TE), 4 nm switching layer Ta_2O_5, a 30 nm $TaO_{0.5}$ reservoir layer, and 30 nm bottom electrode layer Pd (BE), as shown in Figure 2.5a. The simulation depth is 20 nm.

The initial condition of the pristine device is based on our experimentally fabricated device with a 4 nm near-stoichiometric Ta_2O_5 switching layer ($X^* = 0.95$) and a 30 nm $TaO_{0.5}$ reservoir layer ($X^* = 0.2$). For LRS, a filament spans the switching layer at the center with the composition of $TaO_{0.4}$ ($X^* = 0.16$). A smoothing region of approximately 1nm is introduced between areas of varying concentration to ensure continuous first spatial derivatives. For HRS, there exists a gap

between the broken filament and TE. To maintain the metal-to-oxygen ratio in the LRS (intact filament) equal to that in the HRS (broken filament), it is assumed that the oxygen vacancies in the gap area disperse into a larger region. This dispersion is linearly proportional to the gap size in both the horizontal and vertical directions (Figure 2.5b). All boundaries are labelled in Figure 2.5c and boundary conditions will be provided in the following sections for each model.

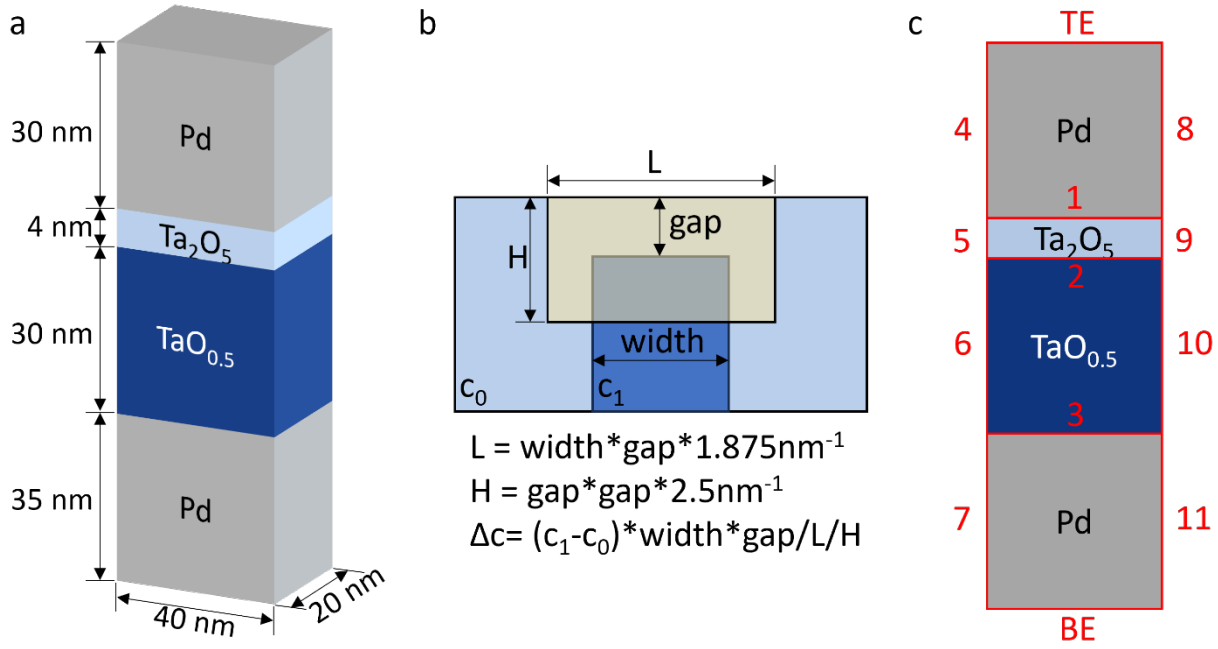


Figure 2.5: Device and switching layer geometry used in the simulation. (a) Device geometry for 2D retention simulation. (b) Dispersion is assumed to be linearly proportional to the gap size in both the horizontal and vertical directions. (c) Boundary labels in 2D device.

2.4.1 Phase Separation Model

The time-dependent evolution of oxygen concentration (c) can be solved with the diffusion equation, which will only include diffusion flux term. We set the diffusion flux term with the generalised transport equation based on chemical potentials. This diffusion equation accounting for phase separation is given by

$$\frac{\partial c}{\partial t} = -\nabla \cdot J = \nabla \cdot \left(\frac{Dc}{k_B T} \nabla \mu\right) \qquad (1)$$

where $\mu(X^*)$ is the chemical potential, k_B is the Boltzmann constant, T is the temperature (300°C), and D is diffusion coefficient. We assume that the diffusion coefficient *D* is a constant 1 $nm^2\ s^{-1}$. We use $\sqrt{Dt}$ (t = time; units in nm) to represent the progression of diffusion so that our results can be generalised to different absolute values of the diffusion coefficient *D*. The boundary 1,3,5,6,9,10 are zero-flux.

2.4.2 Fickian Diffusion Models

For the Fickian diffusion models based on an ideal solution assumption, we set the diffusion flux term to equal the oxygen concentration gradient. Then the diffusion equation is given by

$$\frac{\partial c}{\partial t} = -\nabla \cdot J = \nabla \cdot (D\nabla c) \qquad (2)$$

where c is oxygen concentration that equals c_0X^*, where c_0 is the oxygen concentration in $TaO_{2.5}$, and D is the diffusion coefficient. In Figure 3.14a and 4.6b, diffusion between the switching layer and the reservoir layer is allowed; this is labelled “Fickian Diffusion —Bilayer Instability” because oxygen vacancies would diffuse from the $TaO_{0.5}$ reservoir to the Ta_2O_5 switching layer. Boundaries 1, 3, 5, 6, 9, and 10 are designated as zero-flux boundaries. Conversely, in Figures 3.14b and 4.6c, diffusion between the switching and reservoir layer is suppressed, so the diffusion process only occurs in the switching layer. Boundaries 1, 2, 3, 5, 6, 9, and 10 are set as zero-flux. This is identified as the "Modified Fickian Diffusion--Filament Dissolution" case.

2.4.3 Electronic Conductance Models

The device conductance is calculated with the continuity equation for electrical conduction is given by

$$\nabla \cdot \sigma \nabla \Psi = 0 \quad (3)$$

where Ψ is the electric potential and σ is the electrical conductivity. The boundary conditions for above equation include that BE is always grounded during simulation, while 0.1V read voltage is applied to the top of TE. Boundaries 4-11 are electrical insulation. Here, the electrical conductivity of the tantalum oxide (σ_{TaO_X}) at room temperature is calculated by

$$\sigma_{TaO_X} = \sigma_0(X^*) + exp(293/T \cdot (\alpha\sqrt{E} + \beta)) \quad (4)$$

where σ_0 is the bulk conductivity from our experiment with linear interpolation (Table 2-1), X^* is the $TaO_{2.5}$ fraction as defined in the main text, the second term is Poole-Frenkel (PF) conduction term, the same with the model in our previous work[50], T is the temperature set as Room temperature (293 K), E is the electrical field, α and β are PF coefficients, which are 5.48e-4 and -5.70, respectively[50]. The conductivity of Pd is set as 1e7 S/m[50].

In the resistive switching model, the three PDEs (eqn. 1, 3, 4) or (eqn. 2-4) are self-consistently solved to calculate c and Ψ using the finite element method using COMSOL Multiphysics 6.0.2.

Table 2.1: Table of sputtering condition, composition, and conductance. The composition was measured using AES, while the resistivity was measured using a four-point measurement. Table reproduced with permission from ref.[51]. Copyright 2024.

Composition	O_2 Gas Flow Percentage 100W @5mTorr	Resistivity (Ωm)
Ta	0% O_2	8.07e-6
$TaO_{0.7}$	1.5% O_2	2.15e-4
TaO	2.5% O_2	2.51e-2
$TaO_{1.5}$	5% O_2	3.32
~TaO_2	10%O_2	~948
Ta_2O_5	50%O_2	~1228

2.5 Material Characterization

To assess the dynamics of oxygen movement, materials characterization techniques, like Time-of-Flight, secondary-ion mass spectrometry (ToF-SIMS) and Auger electron spectroscopy (AES) were employed to estimate and quantify the speed and direction of oxygen transport in the amorphous TaOx. Together, these techniques offered complementary insights into the mechanisms of oxygen diffusion, enabling a comprehensive analysis of the transport properties in the model structures.

2.5.1 Auger Electron Spectroscopy

AES can analyze the elemental composition and chemical states of surfaces with high spatial resolution (Figure 2.6). This technique involves the emission of Auger electrons from the surface, providing valuable insights into the elemental distribution and electronic structure of the materials under study. By using AES companying with sputtering etch, I can precisely identify and quantify in-depth profiles of the sample's composition, which is essential for understanding the chemical composition in the TaOx thin films before and after annealing.

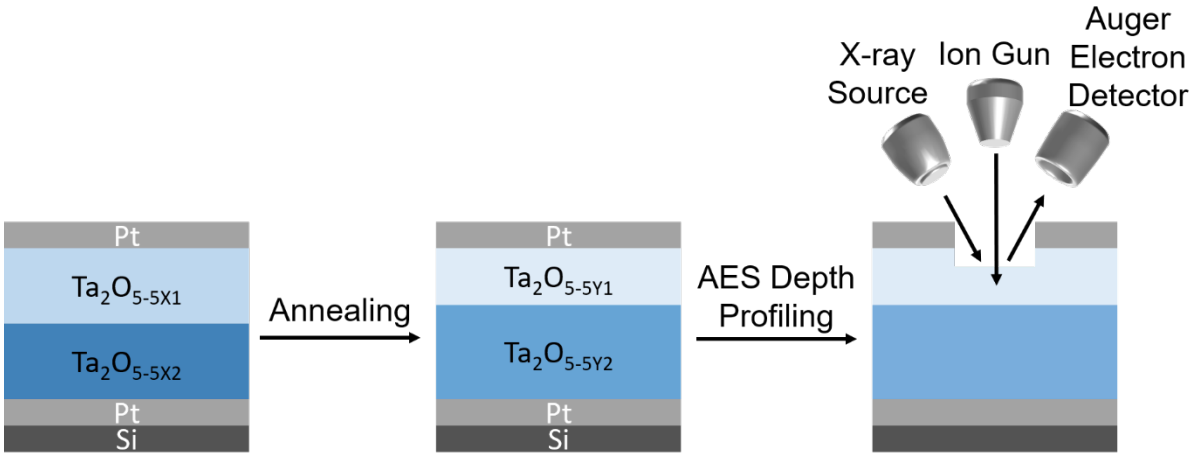


Figure 2.6: Experimental setup for AES depth profiling on oxide bilayer before and after annealing treatment. The Pt cap layer is grown to block oxidation in the air.

Ta_2O_5/TaO_X bilayer (~35/45 nm) samples for the AES were deposited using DC reactive sputtering using a 76 mm Ta metal target (Plasmaterials, 99.95% purity) with an AJA Orion-8 Sputter System at room temperature. The gas pressure was 5 mTorr while the power was 100 W for all depositions. The oxygen concentration X is controlled by the $Ar:O_2$ ratio in the sputtering chamber. The total gas flow rate was 40 sccm. Table 2.1 shows the effects of different $Ar:O_2$ ratio in the sputter chamber on the Ta:O ratios measured in the films using AES. Annealing was conducted in ~300 Torr of Argon at elevated temperatures in the Everbeing C-196 Probe Station.

$HfO_2/HfO_{0.4}$ bilayer (~35/35 nm) samples were deposited using DC reactive sputtering using a 76 mm Hf metal target (AJA International Inc, 99.9% purity) with an AJA Orion-8 Sputter System at room temperature The gas pressure was 5 mTorr while the power was 100 W for all depositions. HfO_2 and $HfO_{0.4}$ layers were grown with 1:1 (50% O_2) and 397:3 (0.75% O_2) $Ar:O_2$ ratio, respectively. The total gas flow rate was 40 sccm. Annealing was conducted in ~300 Torr of Argon at 300ºC in the Everbeing C-196 Probe Station. All Pt layers are also DC sputtered at 100W on a 51-mm Pt target at an Ar gas pressure of 5 mTorr.

The elemental composition of the TaO_x samples was characterised via AES using a Phi 680 scanning Auger nanoprobe from Physical Electronics (Chanhassen, MN) at Ford Research (Dearborn, MI). Data was collected using a 10 kV, 10 nA electron beam from an ~ 20 μm^2 area. Sputter depth profiling with a 2 kV argon ion gun was employed to characterise the thin film chemistry. Sputter depth was calibrated using a 100 nm SiO_2 standard sample. Our films do not show substantial sputter reduction due to the uniform Ta:O ratio with depth within each layer.

2.5.2 Time-of-Flight, Secondary Ion Mass Spectrometry

ToF-SIMS, on the other hand, is utilized to obtain in-depth profiles of the sample's composition by sputtering the surface with a focused ion beam and analyzing the ejected secondary

ions. This method offers high sensitivity and depth resolution, allowing for the detection of trace elements and the examination of compositional variations with depth. In my research, ToF-SIMS with is instrumental in mapping the distribution of trace ^{18}O after diffusion. By directly incorporating the tracer ^{18}O into the film, we can perform tracer diffusion measurements in highly reduced sub-oxides, which cannot be accessed in more conventional gas-phase isotope exchange (Figure 2.7). The detailed compositional profiles obtained through ToF-SIMS help in qualifying the diffusivity value in TaOx system across a wide range of compositions.

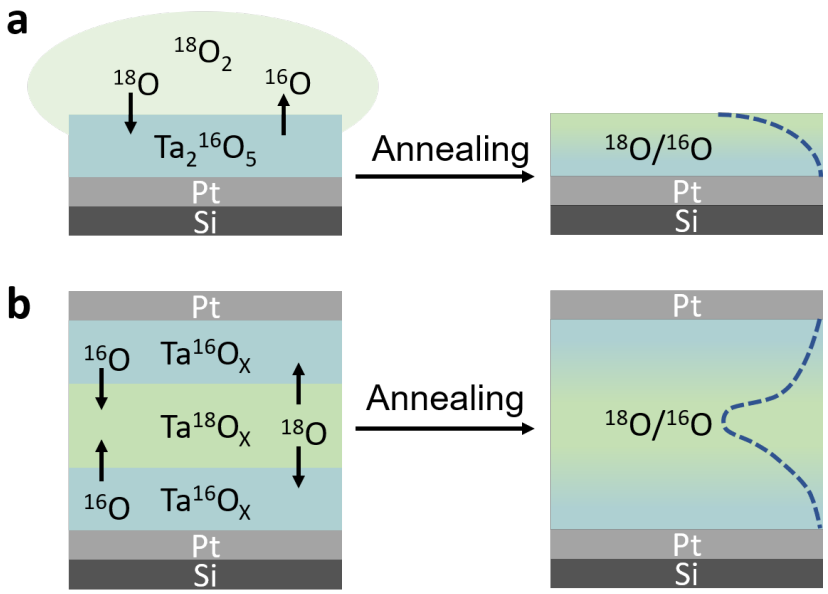


Figure 2.7: Sample preparation for ToF-SIMS. (a) Tracer diffusion samples are traditionally conducted by annealing a natural-abundance (^{16}O) film in $^{18}O_2$-enriched gas at elevated temperatures. (b) Our novel trilayer structure that embeds the ^{18}O tracer into the film stack enables tracer diffusivity measurement in sub-oxide films.

The $Ta^{16}O_X/Ta^{18}O_X/Ta^{16}O_X$ trilayer (~30 nm each) samples used for ToF-SIMS analysis were also grown using the AJA Orion-8 with the same target, power, and gas pressure. All three layers used the same $Ar:O_2$ ratio: Ta_2O_5 used 1:1 ratio of $Ar:O_2$; $TaO_{1.5}$ used 20:1 ratio; $TaO_{0.7}$ used 65:1 ratio. While the top and bottom layers used natural abundance oxygen (~99.8% $^{16}O_2$), the middle $Ta^{18}O_X$ layer was enriched with 99% $^{18}O_2$ (Sigma-Aldrich). The enriched Ta_2O_5 layers used 1:9 ratio of natural to $^{18}O_2$-enriched gas; the enriched $TaO_{1.5}$ used 1:1 ratio of natural to $^{18}O_2$-

enriched gas; the enriched $TaO_{0.7}$ layer used 100% $^{18}O_2$-enriched gas. This approach minimises the use of $^{18}O_2$ to reduce cost. A protective Pt film (~20 nm) is also sputtered above and below the trilayer. The films are annealed at different temperatures in the Everbeing C-196 Probe Station under Ar to initiate tracer (self) diffusion.

The ToF-SIMS measurements for the Ta_2O_5 samples were conducted using a PHI Model Thrift IV from Physical Electronics (Chanhassen, MN) at Ford Research (Dearborn, MI). Samples were analysed using a 30 kV Au+ primary ion beam over a 300 μm × 300 μm area for chemical analysis. Negative ion spectra were acquired without charge compensation. Depth profiling was executed using a 2 kV Argon sputter gun rastered over a 500 μm × 500 μm area. Data acquisition times were limited to ensure the data was collected under static SIMS conditions.

The ToF-SIMS measurements for the two suboxides ($TaO_{1.5}$, $TaO_{0.7}$) were conducted using ToF.SIMS.5-NSC instrument (ION.TOF Gmb) at Oak Ridge National Laboratory. Bi^{3+} liquid metal ion gun operating at 30 keV energy, 0.5 nA current (DC mode) and spot size ~120 nm was used as a primary source for chemical analysis. It was complemented by Cs^+ sputter ion gun operating at 1 keV energy and ~70 nA current for depth profiling and low energy electron flood gun for charge compensation. The measurements were carried out at non-interlaced mode, where each analysis scan by Bi^{3+} (100×100 μm) was followed by 2 s of sputtering with Cs^+ (300 × 300 μm). Secondary ions were analysed by time-of-flight mass analysers with mass resolution $m/\Delta m$ = 100 - 300.

Chapter 3 Thermodynamic Origin of Nonvolatility in ReRAM

3.1 Phase Separation Hypothesis

Oxygen vacancies-based ReRAM, or memristor, is a promising nonvolatile memory that utilizes exceptionally high point defect concentrations (>10%). In these ReRAM, an applied voltage induces the movement of oxygen ions (vacancies) to form or break a conducting filament, changing the tunnel distance at the Schottky barrier, and changing the resistance state[32,52].

The ideal diffusion equation $J = -D\,\nabla c$, which assumes that defects are noninteracting and follow ideal solution thermodynamics, has been universally used to describe oxygen diffusion in ReRAM[7,39,53–55]. Under no applied voltages, Figure 3.1a schematically illustrates the most direct application of ideal Fickian diffusion to a bilayer ReRAM, whereby oxygen vacancies diffuse from the oxygen-deficient conductive reservoir into the initially insulating (near-)stoichiometric switching oxide. Because this bilayer mixing model predicts that pristine devices would become conducting and therefore fail after fabrication[56], it is not used to model retention. Instead, it is generally assumed that oxygen vacancies do not migrate between the stoichiometric and suboxide layers during retention[53,57]. This modified ideal diffusion model predicts that oxygen vacancies diffuse out of the high-concentration filament (Figure 3.1b), resulting in a dissolution of the (broken) filament and a slow change from the LRS and HRS to a more resistive state over time, and is consistent with some experiments[7,53].

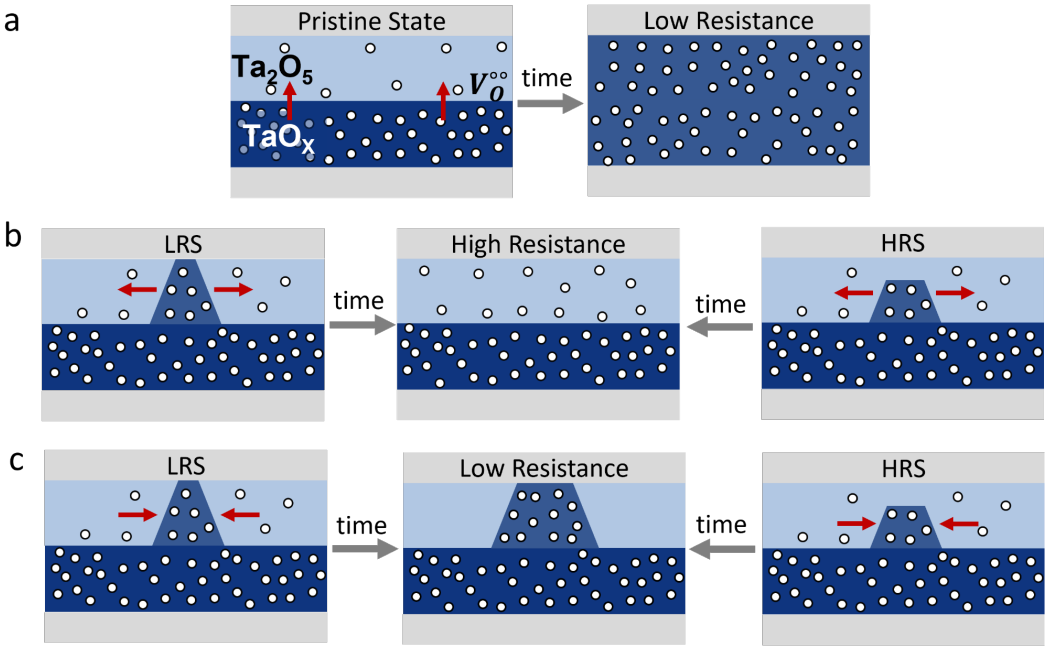


Figure 3.1: Schematic of potential oxygen vacancy migration pathways under no applied voltage in bilayer TaOx ReRAM. a) Fick's first law for ideal solutions, which states that mobile species diffuse from high to low concentration, suggests that the Ta_2O_5 will rapidly gain oxygen vacancies when in contact with a suboxide, resulting in failure shortly after fabrication. b) Most models assume that oxygen vacancies do not migrate between the two oxide layers during retention. Under this diffusion model, the filament dissolves, resulting in increased resistance over time, a result consistent with some experiments. **c)** Other experiments suggest that the filament strengthens over time, yielding a decrease in resistance. This result cannot be explained by either ideal solution Fickian diffusion model, and represents a knowledge gap. We propose this behaviour results from phase separation. Image reproduced with permission from ref.[51]. Copyright 2024.

Although this modified ideal diffusion model is commonly used to describe oxygen transport in ReRAM, there are substantial unexplained inconsistencies with experimental data on tantalum oxide ReRAM. While this model predicts filament dissolution, experimental measurements have shown evidence for both higher resistance from filament dissolution[7,39,53,58] (Figure 3.1b) and lower resistance from filament strengthening[39,54,59,60] (Figure 3.1c). Filament strengthening and the associated decrease in resistance cannot be predicted using ideal Fickian diffusion. Despite decades of research, there is no physical explanation for these substantial deviations in direction from ideal diffusion in ReRAM.

3.2 Retention Measurements in TaO_X-based ReRAM

We assess retention behavior under different annealing (baking) temperatures and times. Because no driving voltages are applied, retention studies eliminate the convoluting factors of electric field and temperature gradients. Our bilayer ReRAM consists of ~4 nm near-stoichiometric Ta_2O_5 above a ~30 nm sub-stoichiometric $TaO_{0.5}$ suboxide (see Experimental Procedures for fabrication details). X-ray diffraction and transmission electron microscopy show that both tantalum (sub-)oxide layers are amorphous due to the low deposition temperatures (Figure 3.2).

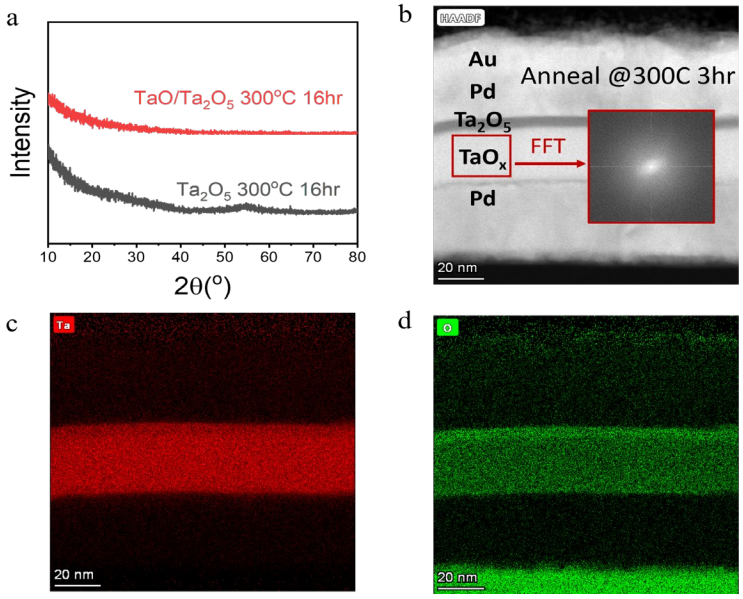


Figure 3.2: (a) X-ray diffraction, (b) cross-section TEM and EDS images of (c) Ta signal and (d) Oxygen signal on TaO_X samples annealed at 300°C. Both the X-ray diffraction and the TEM-fast Fourier transform indicate that the sample remains largely amorphous. Image reproduced with permission from ref.[51]. Copyright 2024.

In Figure 3.3a, our devices show the ability to switch between the low resistance state (LRS, ~1,000 μS) and high resistance state (HRS, 10-100 μS). Figure 3.4 shows the switching statistics. After confirming the switching characteristics, we anneal the devices at different temperatures in inert Ar. We define failure as when the conductance crosses 500 μS. We first consider pristine devices: after baking for 24 hours at 250°C, the conductance increases, but remains substantially more insulating than either the LRS or HRS, and does not fail (Figure 3.3b).

Because the devices remain insulating, it does not follow the bilayer mixing pathway illustrated in Figure 3.1a even at this comparatively high temperature.

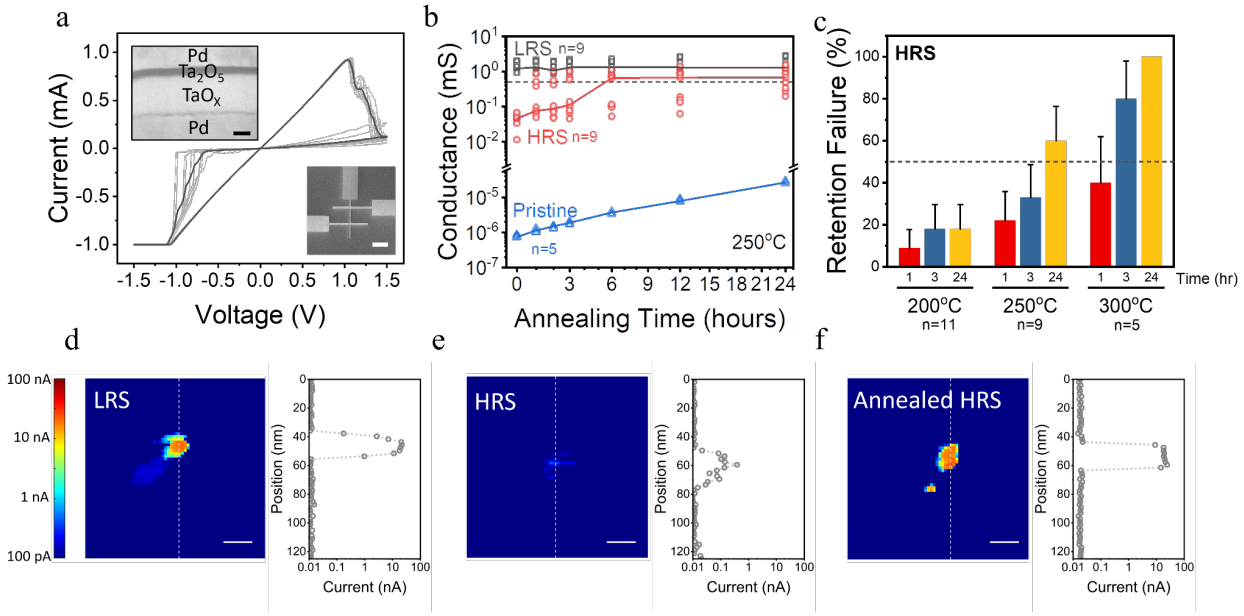


Figure 3.3: Switching, retention, and conductive AFM characterization of the bilayer TaO_X-based memristors. a) A typical switching curve from the ~2 μm^2 crossbar device shows typical resistive switching behaviour. The inserts show cross-section TEM (top left, 10 nm scale bar) and planar SEM image (bottom right, 10 μm scale bar) b) Retention characteristics of devices from the pristine state, HRS, and LRS baked at 250 °C. LRS and pristine state devices are stable, while HRS devices fail over time. The grey dashed line represents the failure threshold. c) HRS retention failure statistics show accelerated device failure as the bake temperature increases. The error bar represents one standard deviation for a binomial distribution (fail or not fail). d-f) C-AFM of the conductive filaments in devices with LRS device (d), HRS device (e), and HRS device annealed at 300°C for 3 hours (f). The broken HRS filament re-forms after annealing in (f). Scale bar is 20 nm. Image reproduced with permission from ref.[51]. Copyright 2024.

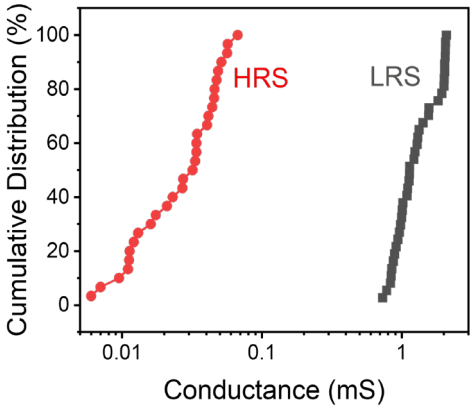


Figure 3.4: Conductance cumulative probability distribution of Pd/TaO_X/Ta_2O_5/Pd devices in HRS and LRS. Image reproduced with permission from ref.[51]. Copyright 2024.

Next, we assess the devices starting in the LRS, where the conductance does not decrease over time as predicted by the widely-used modified Fickian pathway (Figure 3.1b). Instead the conductance increases. This stability is consistent with filament strengthening as depicted schematically in Figure 3.1c. Additionally, none of the LRS or pristine devices baked at temperatures below 350ºC fails (Figure 3.5). We next consider HRS retention. At 250ºC, our HRS devices fail within 6 hours, reverting to a higher-conducting state (Figure 3.3b). This HRS failure indicates oxygen vacancies diffuse into the filament gap, which decreases the tunnel gap at the Schottky barrier between the oxide and the high work function Pd electrode[61]. In Figure 3.3c, we quantify the fraction of HRS devices that fail (>500 μS), and show that the failure time increases at lower temperatures, consistent with previous work[5,7,39]. The stability of the pristine sample shows the reversion to the LRS is not a result of bilayer mixing. Moreover, devices annealed in air also show the same results (Figure 3.5b), confirming that HRS retention failure is not a result of environmental reduction.

We use conductive atomic force microscopy (c-AFM) to directly visualize filament changes. Rather than using the AFM tip to switch the device, as often done in this field, we electrically SET or RESET the device to the desired state (Figure 3.3a), then use an Ar ion beam to remove the top contact. This ensures that we measure the filaments that exist under standard electrical forming and switching conditions, as opposed to filaments made using an AFM tip. Under a 0.5 V bias, our results show an ~8 nm filament with a peak current of ~20 nA in the LRS device (Figure 3.3d), a much weaker filament (~1 nA) in the HRS device (Figure 3.3e), and the re-emergence of the filament in an annealed HRS device (Figure 3.3f). Importantly, the ~10-100× lower c-AFM current in the HRS device is consistent with the ~20× ON/OFF ratio in the devices. Therefore, even though the before (Figure 3.3e) and after (Figure 3.3f) anneal measurements were

conducted on different devices, the consistency between the c-AFM and electronic conductance measurement suggest that the filament has indeed re-formed. More statistics are given in Figure 3.6, which also shows the topology and currents of all imaged devices; no filaments were observed in the pristine devices which were not cycled (Figure 3.6). The absence of filaments in the pristine, unformed samples (Figure 3.6a,b) shows that the imaged filaments (Figure 3.3d-f) were not created by the Ar ion beam; however, we cannot rule out possible surface damage by the Ar ion beam on the underlying oxide layer.

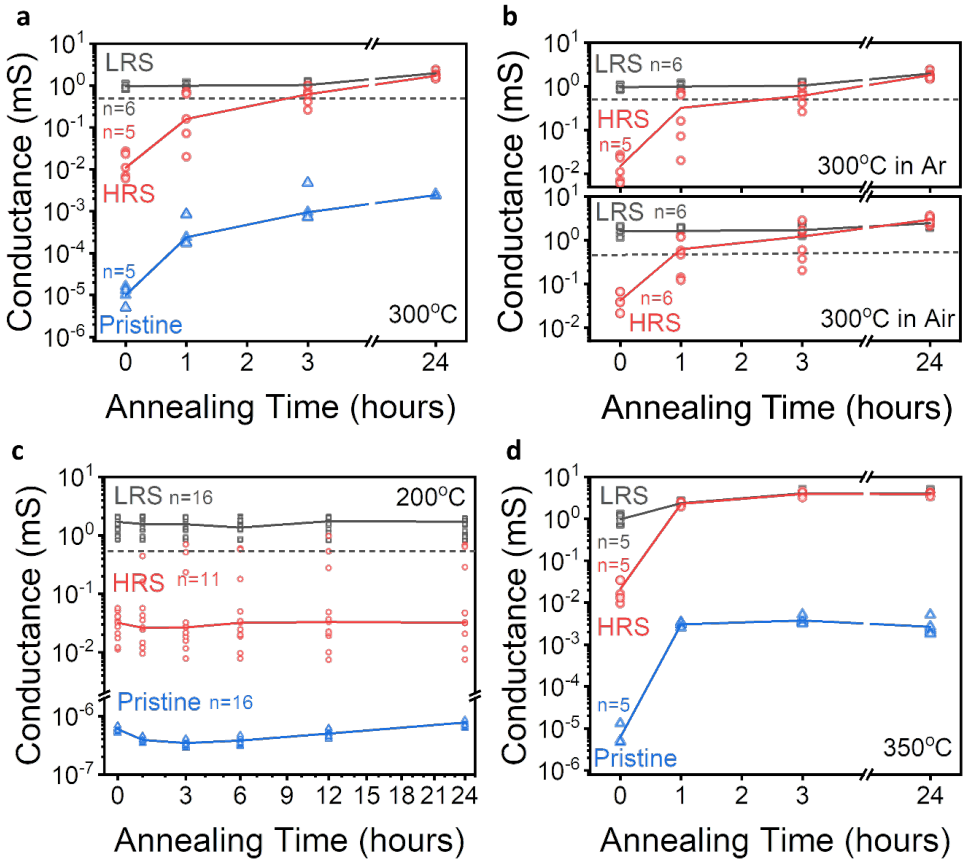


Figure 3.5: (a) Retention measurements of devices from the pristine state, HRS, LRS baked at 300ºC in Ar. (b) The same LRS and HRS retention results are observed in both Ar and air environments, confirming that our observations are not a result of environmental reduction. (c-d) Retention measurements of devices from the pristine state, HRS, LRS baked at 200ºC (c) and 350ºC in Ar. Image reproduced with permission from ref.[51]. Copyright 2024.

Our results in this section show that both the LRS and the pristine devices are stable for >24 hours at 200-350ºC. The HRS, on the other hand, fails; c-AFM measurements show this failure

results from the re-formation of the nanoscale filament. Combined, these results show that the filaments revert from a nonequilibrium, frozen-in state after switching to a stable state with an intact filament and low device resistance after annealing.

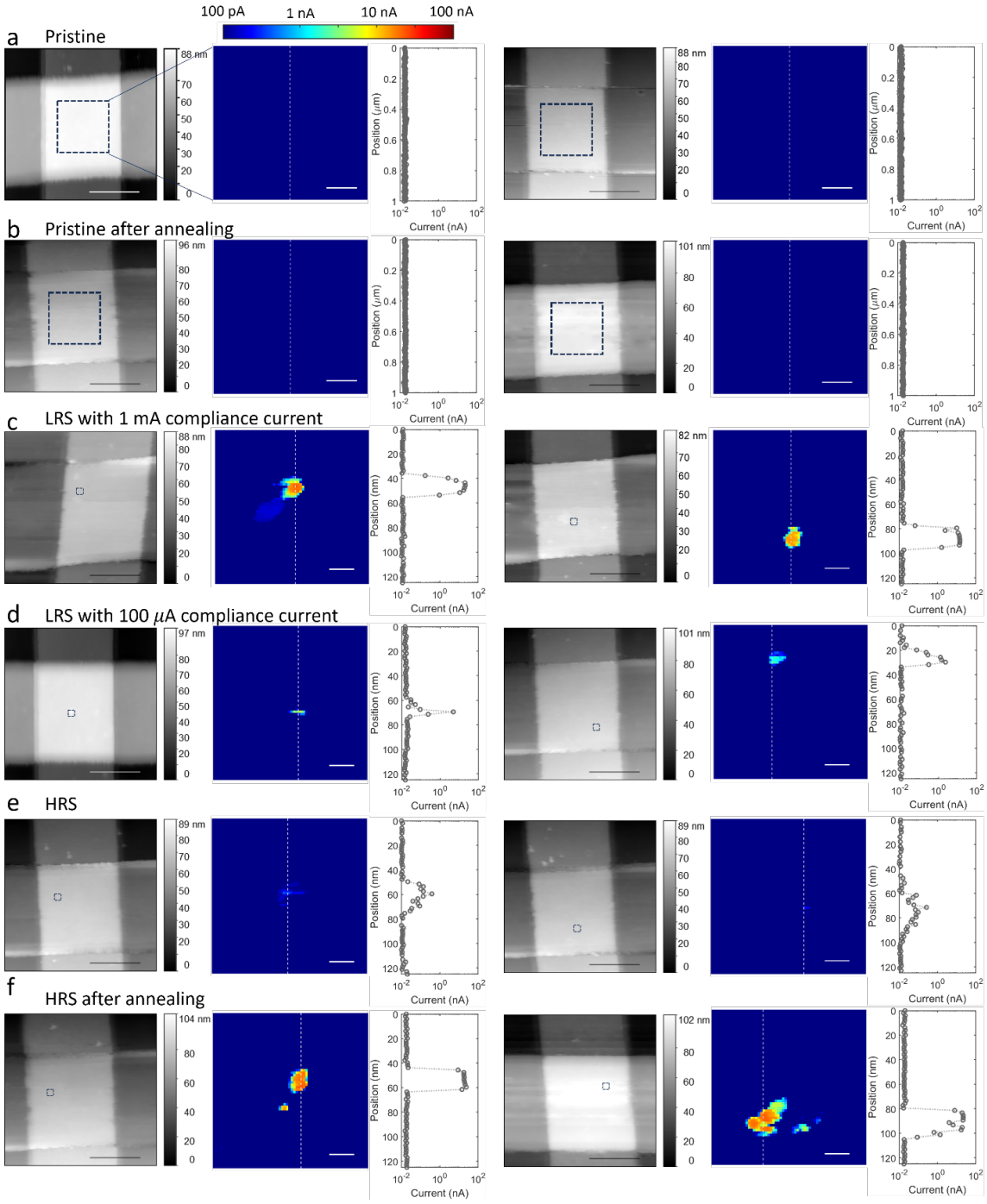


Figure 3.6: Atomic force microscopy images on all devices. (a) Pristine (not switched) ReRAM devices, (b) pristine devices after annealing at 300°C for 3 hours, (c) LRS devices with 1mA compliance current, (d) LRS devices with 100 μA compliance current, (e) HRS with 1mA compliance current and 1.5 V RESET voltage, (f) HRS with 1mA

compliance current and 1.5 V RESET voltage after annealing at 300°C for 3 hours. Image reproduced with permission from ref.[51]. Copyright 2024.

These observations are inconsistent with either Fickian diffusion pathways (Figure 3.1a,b). We will later explain these differences in the context of phase separation, which can explain why some experiments show HRS retention failure[39,54,59,62] like ours, while others yield LRS retention failure[7,53,58].

3.3 Composition Phase Separation in Amorphous Ta-O System

Our observation of increased conductance of both LRS and HRS during retention (Figure 3.3) suggests that oxygen (vacancies) may diffuse against the concentration gradient (Figure 3.1a); this "uphill diffusion" commonly arises during compositional phase separation and spinodal decomposition[48]. In our experiments, phase separation describes the coexistence of two compositionally distinct materials with no net mass flux between the two layers, or "flux equilibrium" where $J=0$ (see Appendix A). Here, the two phases are both amorphous with different Ta:O ratios[63]. Although these amorphous compounds are metastable and have higher energy than the inaccessible crystalline states, mass transport follows the chemical potential of the amorphous states when the crystalline states are inaccessible below 600ºC[64]. While phase transformations have been studied in tantalum oxide memristors[65–67], their relationship to retention time has not been previously considered for this material.

The combination of amorphous materials and the highly variable nanosized filaments make it difficult to directly observe the effects of phase separation on oxygen transport of the filaments. Instead of probing nanosized filaments, we construct a bilayer film with different metal to oxygen ratios as a model system to assess compositional phase separation. Recent X-ray photoelectron spectroscopy results by Heisig et al.[68] showed that the chemistry of a filament is nearly identical to that of a directly sputtered suboxide. Additionally, TEM studies show that the filament is also

amorphous[69]. Building on these results, we anticipate a sputtered amorphous suboxide will have similar thermodynamics as an amorphous oxygen-deficient filament[63].

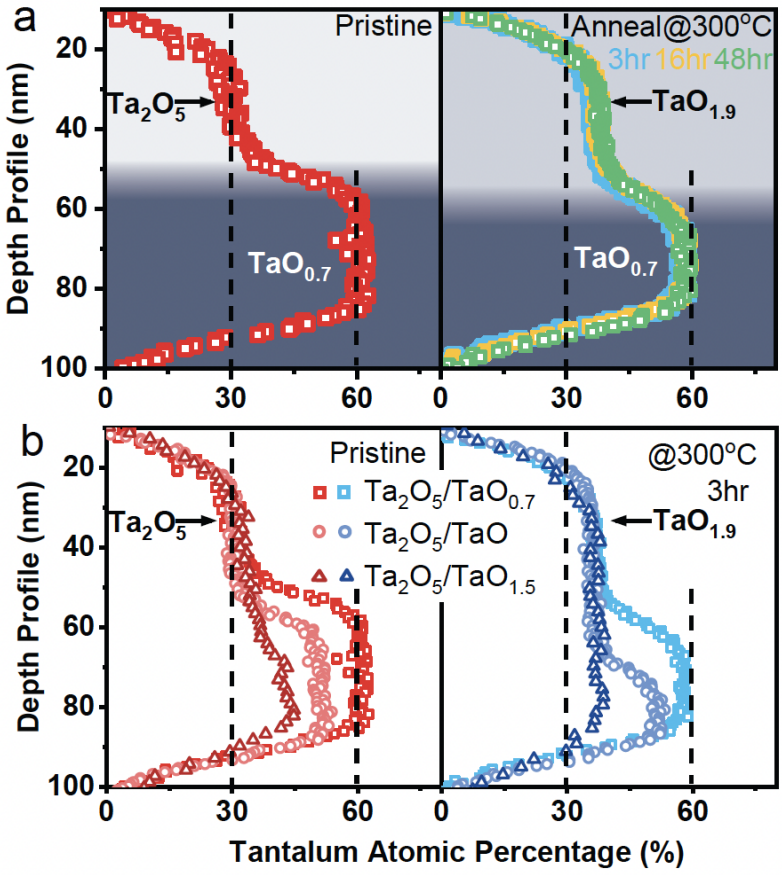


Figure 3.7: Compositional phase separation probed by Auger electron spectroscopy (AES) depth profile of bilayer stack Ta_2O_5/TaO_X. a) The AES depth profile results of $Ta_2O_5/TaO_{0.7}$ before (left panel) and after annealing at 300°C for 3, 16 and 48 hours (right panel). While the Ta_2O_5 is initially oxidised to $TaO_{1.9}$, it does not undergo further exchange of oxygen with the suboxide; this persistent interface after annealing indicates compositional phase separation. A darker plot background colour indicates higher Ta content. b) The AES depth profile results of three bilayer stacks before (left panel) and after annealing at 300 °C for 3 hours (right panel) suggest that the solubility limit at 300°C is $TaO_{1.9}$. Our results do not show substantial sputter reduction due to the relatively uniform metal:oxygen ratio with depth within each (sub)oxide layer. Dashed vertical guidelines convey 30 at% and 60 at% Ta. Image reproduced with permission from ref.[51]. Copyright 2024.

We fabricate bilayer films using a ~35 nm stoichiometric Ta_2O_5 layer on top of ~45 nm tantalum sub-oxides TaO_X with different compositions (X) to investigate phase separation over time. We first investigate the $TaO_{0.7}$ sub-oxide (~60 at% Ta). After annealing the sample at 300°C for 3 hours, the top Ta_2O_5 layer reduces to $TaO_{1.9}$ (~35 at% Ta), while the bottom sub-oxide

remains $TaO_{0.7}$ (Figure 3.7a). The compositional interface between the two layers persists, but moves in position to conserve mass. Importantly, samples annealed at 16 and 48 hours show essentially identical depth profiles (Figure 3.7a). Under the premise that the crystalline state is kinetically unattainable at this temperature[64], our results show that these amorphous samples have reached a state of "flux equilibrium" (J=0) in less than 3 hours. This state shows that composition phase separation is the favored configuration; in contrast, Fick's First Law would predict a progression to a homogeneous single phase.

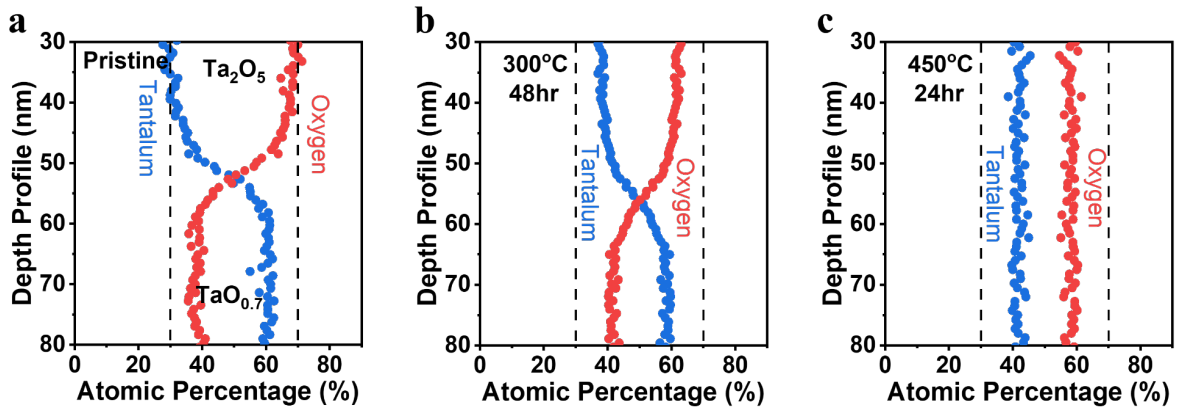


Figure 3.8: Auger electron spectroscopy depth profile on $Ta_2O_5/TaO_{0.7}$ bilayer stack (a) before and after annealing at (b) 300°C for 48 hours and (c) 450°C for 24 hours. Image reproduced with permission from ref.[51]. Copyright 2024.

We next change the bottom suboxide to TaO and $TaO_{1.5}$. After annealing, the oxidized top layer all converts to $TaO_{1.9}$ and expands over the bottom layer while conserving oxygen (Figure 3.7b). The results for all samples suggest that the $TaO_{1.9}$ sub-oxide is the solubility limit at 300°C in amorphous tantalum-oxide; this solubility limit increases to at least $TaO_{1.4}$ at 450°C (Figure 3.8), consistent with an increase in the solubility for most materials at higher temperatures. In contrast, the crystalline phase diagram of tantalum oxide exhibits negligible solubility below 1000°C[45]. Even though the filament and suboxide film may possess some chemical differences, the persistent compositional interfaces (Figure 3.7) and extremely stable LRS (Figure 3.3) tell a consistent story: the oxygen-rich and oxygen-poor regions will not mix (Figure 3.1b), but will

instead remain separate (Figure 3.1c). Moreover, this composition phase separation is also observed in an amorphous $HfO_2/HfO_{0.4}$ bilayer, where $HfO_{1.6}$ is measured to be a stable phase (Figure 3.9). This phase separation can also explain why certain studies also show the HRS fails to the LRS in Hf-based ReRAM devices[60,70], like the case for Ta-based ones[39,62], despite using different combinations of top and bottom electrodes.

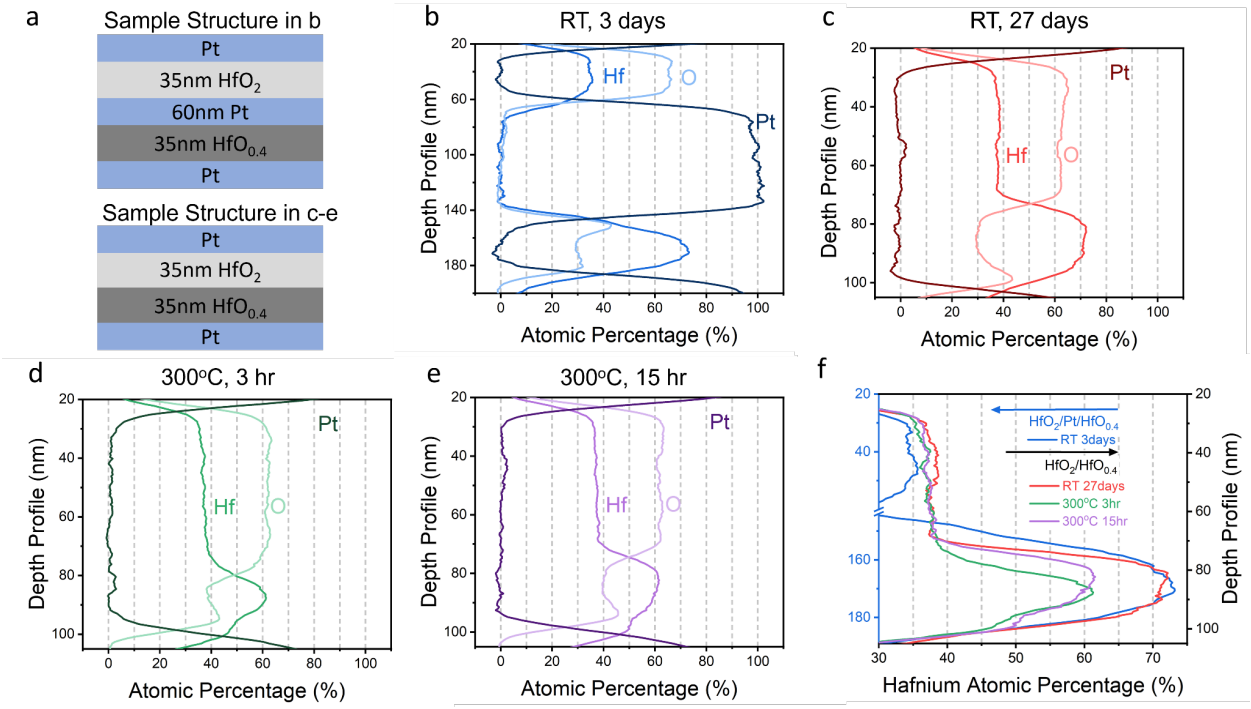


Figure 3.9: Auger electron spectroscopy (AES) depth profile of $HfO_2/HfO_{0.4}$ shows composition phase separation. a) Schematic of the bilayer sample $HfO_2/HfO_{0.4}$ with (b) and without (c-e) 60 nm Pt blocking layer. We included the Pt interlayer in (b) to suppress O diffusion between the two Hafnia layers. b) The AES depth profile of $HfO_2/Pt/HfO_{0.4}$ shows the compositions of a "pristine" material. c) Without a Pt blocking layer, the $HfO_2/HfO_{0.4}$ bilayer would exchange oxygen even at room temperature, such that the HfO_2 layer is reduced to $HfO_{1.6}$ d-e) After annealing at 300°C, the composition gradient persists, which suggests amorphous phase separation like for TaOx bilayer (Figure 3.7). Unlike the case for TaOx, the HfOx suboxide layer became more oxidised over time due to residual oxygen during annealing. However, the top $HfO_{1.6}$ layer composition remains unchanged despite annealing, just as the $TaO_{1.9}$ layer in Figure 3.7, indicating phase separation. In addition to the anneal, these samples also resided at RT for 27 days before the AES measurement. f) The Hf atomic fraction for the samples in (b-e). Without a blocking Pt layer, HfO_2 is reduced to $HfO_{1.6}$ for all conditions tested. We anticipate $HfO_{1.6}$ to be one stable phase in the amorphous Hf-O system, just as $TaO_{1.9}$ is a stable phase in amorphous Ta-O system (Figure 3.7). This composition phase separation result is broadly similar to that of the Ta-O bilayer tested in Figure 3.7. Image reproduced with permission from ref.[51]. Copyright 2024.

3.4 Ab initio Thermodynamic Calculations

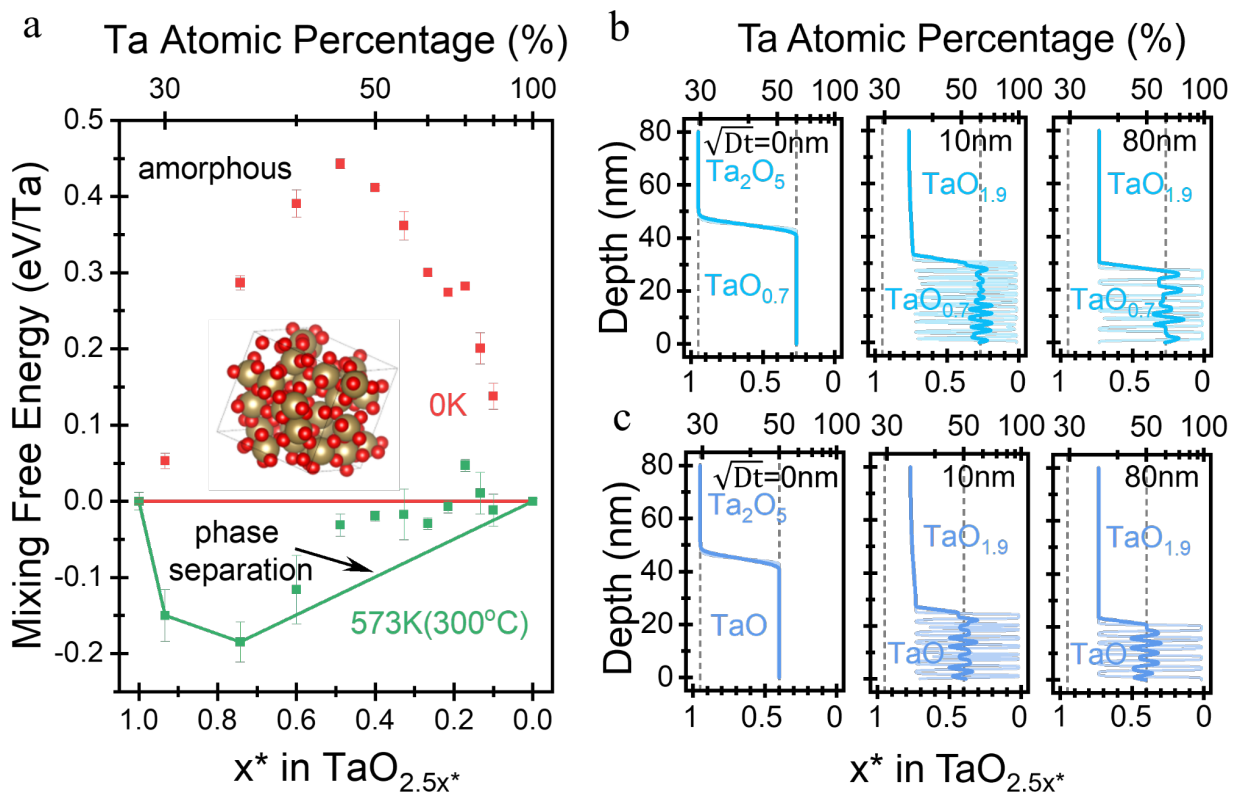


Figure 3.10: Atomistic calculation and phase-field simulation of Ta-O system. a) Mixing free energy of TaO_X across a series of compositions including enthalpy and entropy at 300°C (see Experimental Proecdures). These energies are referenced that of amorphous Ta (X*=0) and Ta_2O_5 (X*=1) at 0K. The common tangent and the convex hull indicate phase separation between ~$TaO_{1.9}$ (X*~0.74) and Ta (X*~0). The insert is the amorphous structure generated. b-c) Phase-field simulation of oxygen diffusion in bilayer stacks of (b) $Ta_2O_5/TaO_{0.7}$ and (c) Ta_2O_5/TaO which incorporates phase separation with the formation energy fitted from (a). These simulations qualitatively capture the Auger depth profile in Figure 3.7b. The light color line is the simulation results, and the dark color line is the 5-nm average value to account for depth- and lateral-average of AES measurement. Image reproduced with permission from ref.[51]. Copyright 2024.

Having experimentally shown compositional phase separation, we next investigate phase separation computationally using *ab initio* calculations and phase-field simulations. The *ab initio* calculations presented in this chapter (Figure 3.10a) were conducted in collaboration with Anirudh Appachar and Prof. Wenhao Sun, whose expertise in computational modeling significantly contributed to the analysis of phase separation in TaO_X. We first use density functional theory to compute the free energy of amorphous tantalum oxide across different oxygen compositions

between Ta and Ta_2O_5. We use *ab initio* molecular dynamics with Canonical Ensemble (NVT) conditions, where the atomic volume is determined from the experimentally measured density (Figure 3.11), to generate amorphized structures of tantalum oxide. The samples are relaxed at 0K to compute the time-averaged formation enthalpy of the amorphous phases (Figure 3.12). The amorphous formation enthalpies are all higher than that of the crystalline Ta-O convex hull energies (Figure 3.12); however, the crystalline states are not accessible for the temperature and times of our experiments[64] (Figure 3.3).

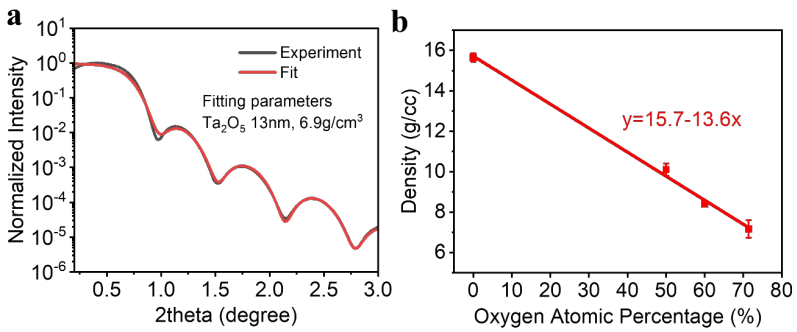


Figure 3.11: X-ray reflectivity characterizations on TaO_X thin film thickness and density. (a) X-ray reflectivity result of Ta_2O_5 thin film grown on Si chip with fitted curve. (b) Density of TaO_X of different compositions derived from X-ray reflectivity. A linear fitting between density and oxygen percentage is used to calculate the volume/atom for DFT calculation. Image reproduced with permission from ref.[51]. Copyright 2024.

To account for the entropy of mixing, we develop a two-sublattice model, where the configurational entropy of the oxygen sublattice is calculated from mixing between oxygen ions and vacancies, and the configurational entropy of the tantalum sublattice is calculated from the mixing between various Ta oxidation states. For the latter, we use a dynamic programming approach to solve for the number of microstates where the possible Ta oxidation states are charge-balanced by the oxygen composition. Finally, we compute the Gibbs energy of mixing by referencing the total Gibbs free energy to that of amorphous-Ta and amorphous-Ta_2O_5 (Figure 3.12). The resulting Gibbs free energy of mixing curves at T=300°C yield a 'w'-shaped curve, representative of a spinodal, with the local minima located at $TaO_{1.9}$ (~35 at% Ta) and ~Ta (100

at% Ta) (Figure 3.10a). These results are qualitatively consistent with previous calculations[39] that show phase separation between amorphous Ta_2O_5 and TaO_2 at 0K; however, our calculations span the entire Ta-O composition range and account for entropy.

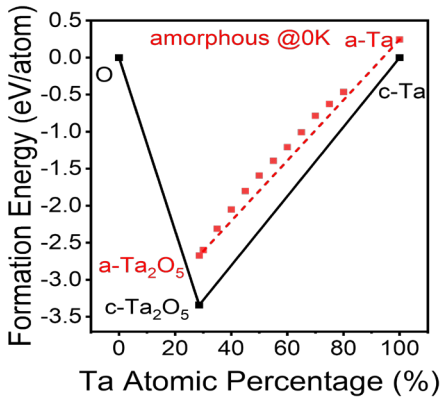


Figure 3.12: Amorphous Formation Energy at 0K calculated by DFT referenced to the elemental states of Ta and O. The plot includes the convex hull of crystalline phases. To obtain the mixing free energy (Figure 3.10a), we subtract the formation energy from the red dashed line connecting a-Ta_2O_5 and a-Ta. In other words, the free energy of mixing is referenced to the amorphous Ta_2O_5 and Ta phases at 0 K. Image reproduced with permission from ref.[51]. Copyright 2024.

Next, we combine the computed formation energy of amorphous tantalum oxide with a phase-field model to simulate the bilayer composition over time. In this phase-field model, mass flux (J) follows the gradient of the computed chemical potential μ from Figure 3.10a and Figure 3.13 via $J = -D/k_B\,T\,c\,\nabla\mu$, where c is the oxygen concentration and D the oxygen diffusivity. Because the crystalline Ta and Ta_2O_5 states (Figure 3.12) are not kinetically accessible from the amorphous state, mass transport under the thermally-constrained metastable equilibrium will follow the chemical potential of the amorphous Ta-O compound, computed from the amorphous Gibbs Free Energy of Mixing (Figure 3.10a and 3.13).

We first simulate the stacked Ta_2O_5 and sub-oxide $TaO_{0.7}$ (60 at% Ta) bilayer (Figure 3.10b) in one dimension. Here, Ta_2O_5 is reduced to the solubility limit of $TaO_{1.9}$ (35 at% Ta), consistent with experiment (Figure 3.7a). The bottom suboxide $TaO_{0.7}$ undergoes spinodal decomposition into two stable phases (lighter color), but the composition averaged over 5 nm

remains ~$TaO_{0.7}$ (60 at% Ta). Experimental evidence for spinodal decomposition into Ta-rich and O-rich regions has been observed using electron microscopy in memristive filaments[47]. However, our 1D Auger depth profile does not have lateral resolution and only captures the average composition spatially averaged over many microns; the averaged depth profiles in Figure 3.7 is consistent with a 5-nm depth-averaged simulation (darker color) in Figure 3.10b. When we replace the sub-oxide layer with TaO (50 at% Ta), the top Ta_2O_5 layer is also reduced to $TaO_{1.9}$ and bottom TaO layer is decomposed into two phases with an average 50at% Ta composition (Figure 3.10c), again matching experiment results (Figure 3.7b). The Ta_2O_5/$TaO_{1.5}$ (40 at% Ta) bilayer simulation (Figure 3.14) is again consistent with experiment (Figure 3.7b), which eventually becomes a single layer with $TaO_{1.9}$ (35 at% Ta). In contrast, if we ignore phase separation and assume ideal Fickian diffusion ($J = -D\,\nabla c$), the Ta_2O_5/$TaO_{0.7}$ and Ta_2O_5/TaO bilayers evolve to a single compositionally homogeneous layer in Figure 3.15, in stark contrast with experiment.

Our experimental (Figure 3.7) and computational (Figure 3.10) results both show persistent compositional phase separation, and independently identified the $TaO_{1.9}$ sub-oxide as one of the solubility limits at 300°C. Four-point electrical measurements show that TaO_2 is electronically insulating (Table 2.1) despite having a nominal 20% oxygen deficiency because it is amorphous; this result is consistent with other studies which utilize TaO_2 as the pristine, initially-insulating switching layer[69,71]; as a result, the conducting filaments must be more conducting and reside in the miscibility gap. Our results show that a film with 40at% Ta, quantified by Auger, is needed to create an electronically conducting film. This number is somewhat higher than ones quantified in a recent work using XPS (33at% Ta)[68], which we attribute to differences in the quantification values of Auger and XPS.

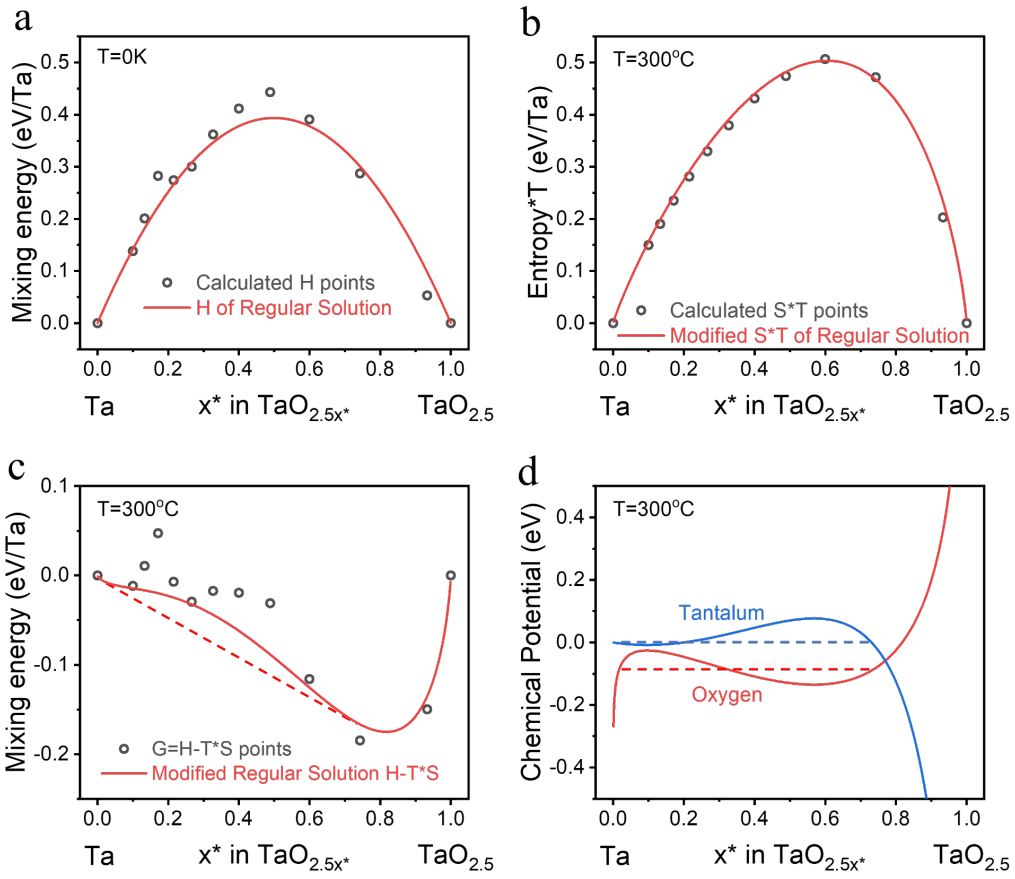


Figure 3.13: Free energy curve fitted from DFT free energy points at 300°C and corresponding oxygen chemical potential. (a) The DFT enthalpy (free energy at 0K) points are fitted by the enthalpy component of the regular solution model. (b) The entropy points fitting is based on a modified entropy component of the regular solution model. (c) DFT free energy points at 300°C and modified regular solution model based on enthalpy component of (a) and entropy component of (b). (d) Chemical potential of oxygen and tantalum is calculated from the slope of the Gibbs free energy of $TaO_{2.5x*}$ and then divided by the number of oxygen atoms in a unit cell (2.5). Chemical potential of tantalum is calculated from the intercept of the Gibbs free energy of $TaO_{2.5x*}$ at Ta side. Image reproduced with permission from ref.[51]. Copyright 2024.

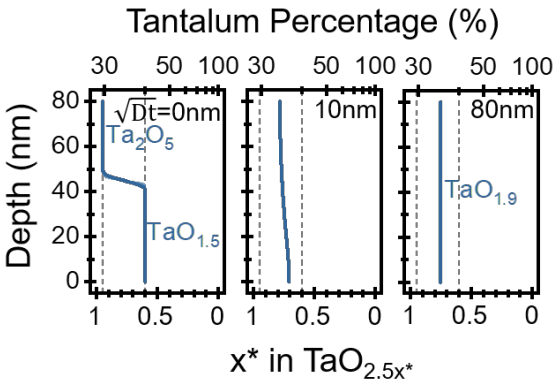


Figure 3.14: Phase-field simulation of $Ta_2O_5/TaO_{1.5}$ shows it converges to a single layer with ~$TaO_{1.9}$ (35 at% Ta). Image reproduced with permission from ref.[51]. Copyright 2024.

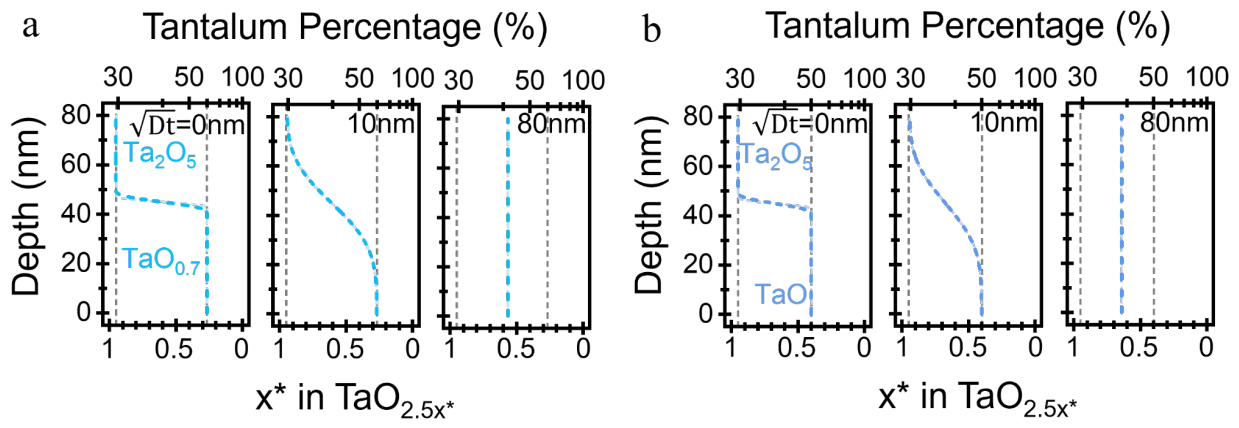


Figure 3.15: (a-b) A simple ideal Fickian diffusion model based on $J = -D\nabla c$ for $Ta_2O_5/TaO_{0.7}$ (a) and Ta_2O_5/TaO (b) will yield a homogeneous depth profile. This ideal Fickian diffusion model contradicts the AES experiments in Figure 3.7. Image reproduced with permission from ref.[51]. Copyright 2024.

3.5 Phase-field Simulations of Device Operation

Finally, we conduct 2D phase-field modeling to simulate the evolution of the conductive filament in the Ta_2O_5/TaO_X memristor over time. We consider both the ideal solid solution model that yields Fickian diffusion ($J = -D\nabla c$) used in previous work[50,72], as well as the amorphous phase separation model ($J = -D/k_B T\, c\, \nabla\mu$) based on a regular solution.

Substantial differences between the two models arise during retention simulations. I simulate the filament composition as $TaO_{0.4}$ based on recent transmission electron microscopy results by Skronowski and colleagues[69], and the reservoir suboxide as $TaO_{0.5}$, which is the experimentally measured suboxide composition of our devices. The ideal Fickian diffusion model shows that the pristine, LRS, and HRS will revert to the same low resistance state (Figure 3.16a), like in Figure 3.1a and in contrast to the pristine device results in Figure 3.3. If we suppress phase separation between the two oxide layers (Figure 3.16b), the pristine, LRS, and HRS will revert to the same HRS after annealing like the scheme in Figure 3.1b, again contradicting the LRS measured in Figure 3.3. In contrast, the regular solution model based on the calculated Gibbs free

energy (Figure 3.16c) shows that both the pristine and the LRS states are stable and will not fail, while the HRS state will fail and revert to LRS, all consistent with experiment (Figure 3.3).

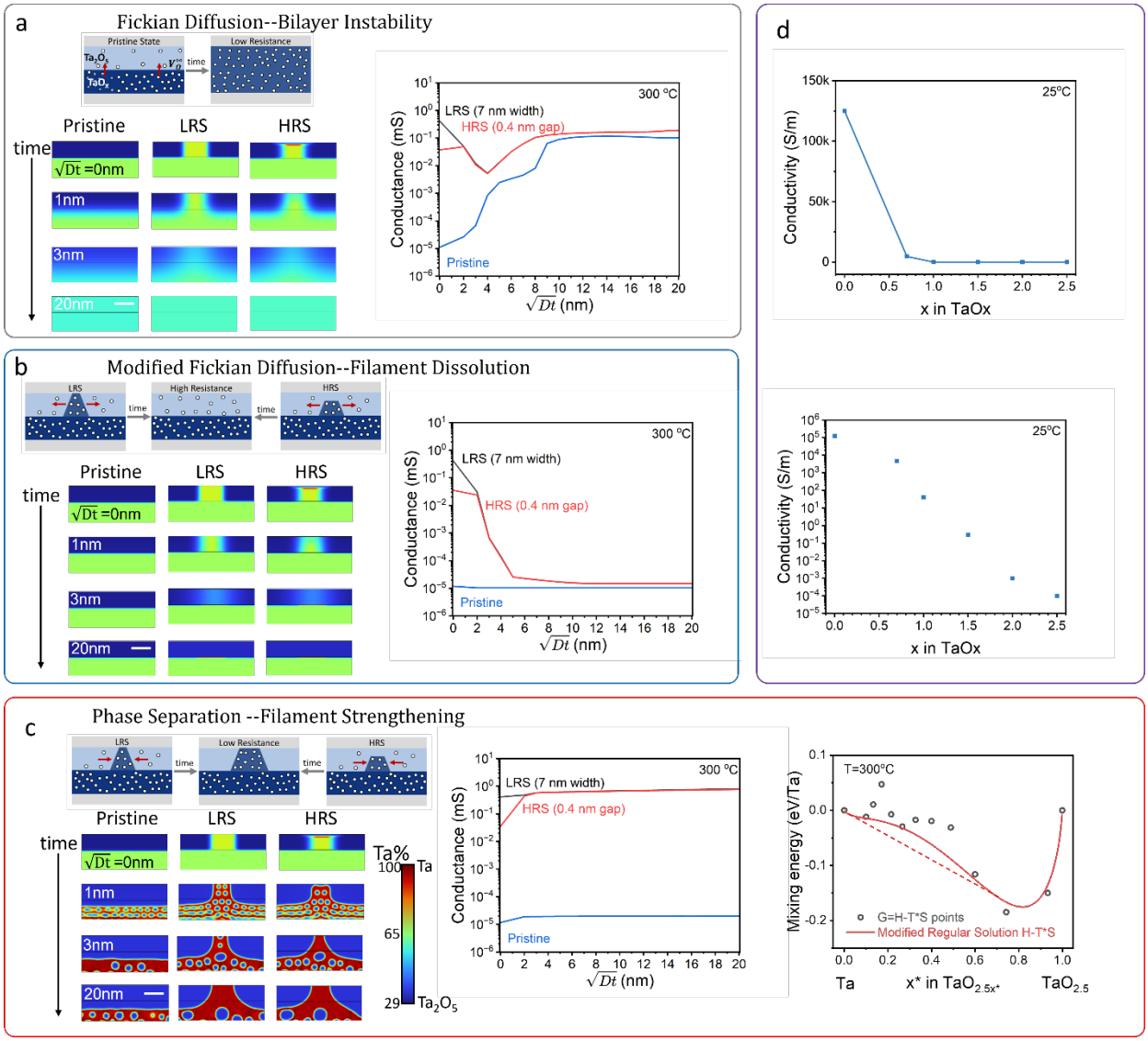


Figure 3.16: 2D Phase-field model for $Ta_2O_5/TaO_{0.5}$ device during retention. Retention simulations on pristine state, LRS (filament width = 5 nm) and HRS (filament gap = 0.3 nm) based on (a) Fickian diffusion, (b) modified Fickian diffusion that suppresses diffusion between the two layers, and (c) the phase separation model with calculated Gibbs free energy curve. Scale bar is 5 nm. These simulations are in broad agreement with the schemes shown in Figure 3.1, reproduced here; however, only (c) is consistent with the experimental results (Figure 3.3b). The simulated electronic conductance uses eqn. 4 and combines the bulk conductance (Table 2.1), interpolated in part (d), and the Poole-Frenkel model[50]. The scale bar is 5 nm. Image reproduced with permission from ref.[51]. Copyright 2024.

While these simulation conditions are consistent with our experiments in Figure 3.3, other researchers have shown LRS retention failure where devices revert to high resistance[7,53,55]. By

parametrically exploring this phase-field model, we identify the filament width, filament gap, and gradient energy penalty as the critical parameters to assess the stability of the LRS and the HRS. Figure 3.17a shows a case where the HRS fails while the LRS is stable (does not fail), which qualitatively resembles our experimental results (Figure 3.3). When the filament width is decreased from 7 nm to 3.5 nm (Figure 3.17b), the filament would dissolve over time, resulting in LRS retention failure. Finally, by increasing the gap distance from 0.4 to 0.8 nm while keeping the filament width at 7 nm, both the LRS and HRS devices remain stable in respective states for very long times due to phase separation. We will experimentally validate these three regimes in the next section. In all cases, our phase separation model ensures that the pristine devices are insulating, like in Figure 3.16c, without the need to additionally constrain transport between the reservoir and switching layers. These simulations also show the filament and suboxide layer initially separate into amorphous Ta and $TaO_{\sim 1.9}$ regions with a domain size ~2 nm as a result of the solubility limits calculated in Figure 3.10. These spinodal decomposition features are consistent with recent electron microscopy by Skowronski and colleagues[47,69,73].

Figure 3.17d plots the retention stability range of LRS and HRS as a function of the filament width and filament gap. The critical filament width W* approximately defines the boundary between filament dissolution and strengthening, which controls whether the LRS fails. When the gap is smaller than the threshold G_s (black line), a broken filament will re-form, leading to HRS retention failure. On the other hand, when the gap is larger than the threshold G_s, the broken filament will dissolve, resulting in neither LRS nor HRS retention failure (Figure 3.17c). In Figure 3.18, we simulate how the critical filament width and gap are affected by the gradient energy penalty, which represents the interfacial energy. These simulations suggest that both thresholds are related to the characteristic stability wavelength λ, and provide a design rule:

lowering the gradient energy penalty would increase the parameter space for the "green" stable regime given by Figure 3.17c, where neither the LRS nor the HRS will fail. While the exact thresholds depend on material parameters like the gradient energy penalty (Figure 3.18), the directional trends among the three failure regimes have been consistently simulated and, as we show in the next section, experimentally verified.

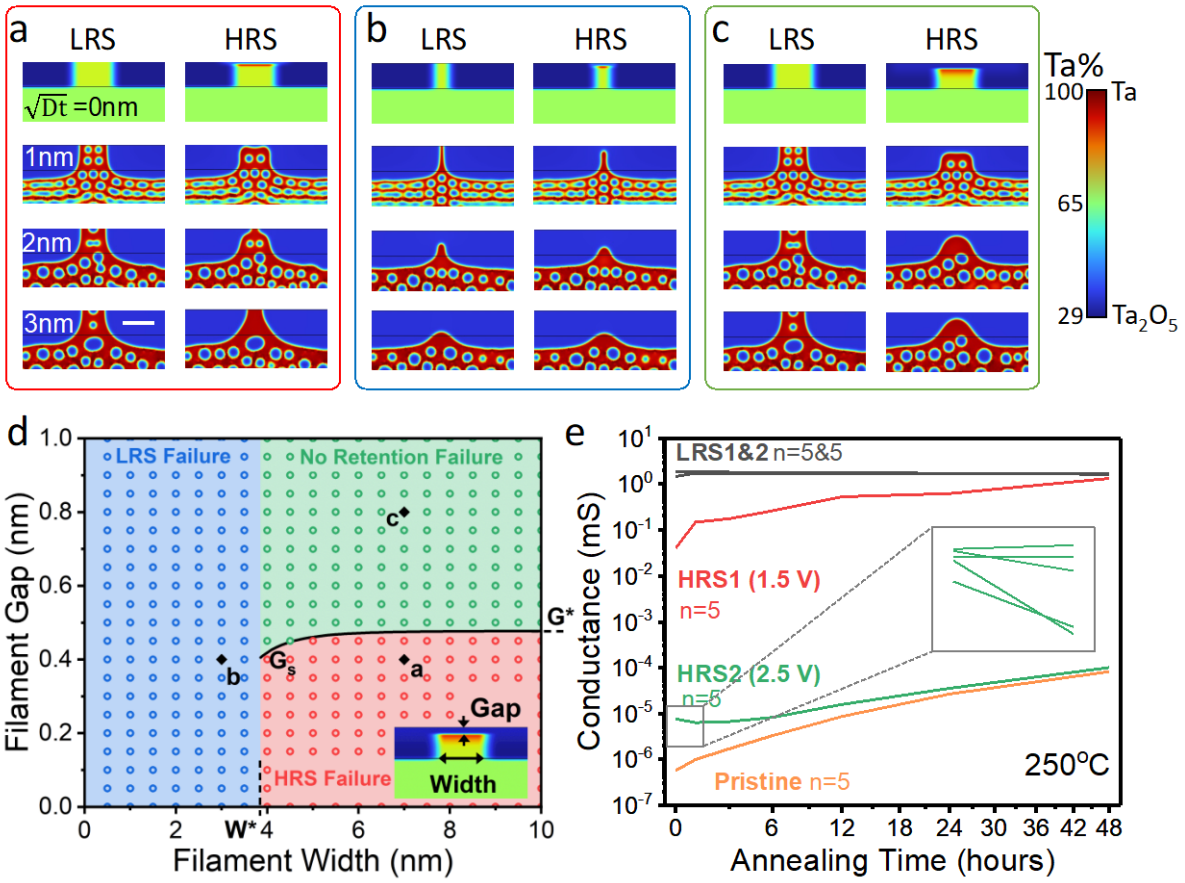


Figure 3.17: Origin of HRS and LRS Retention Failure with 2D Phase field model for $Ta_2O_5/TaO_{0.5}$ bilayer memristor. a-c) Retention measurement simulation on LRS and HRS with different filament gap and filament width. Scale bar is 5 nm. d) The simulated stability of LRS and HRS as functions of the filament width and gap. Each circle represents one simulation that maps to the schematic shown in a, b, or c. e) The experimental retention results at 250 °C using different RESET voltage (1.5 and 2.5 V). The inset shows a clear decrease in the HRS conductance upon baking for one hour, consistent with the predictions of (c). Image reproduced with permission from ref.[51]. Copyright 2024.

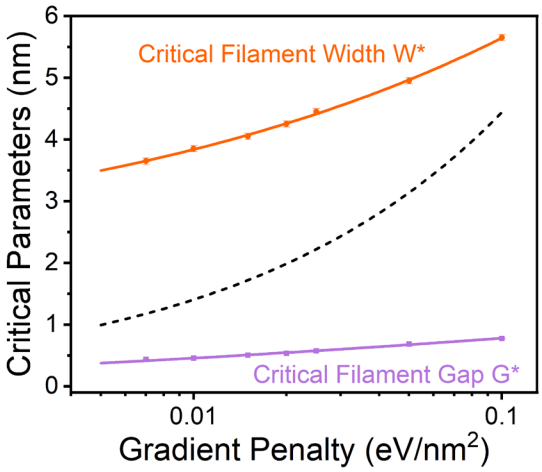


Figure 3.18: The critical parameters as functions of gradient energy penalty with 2D Phase field model for $Ta_2O_5/TaO_{0.5}$ bilayer memristor. The critical filament width and gap can be controlled using the gradient energy penalty in the simulation. Δf_{homo} is assumed to equal 0.1 eV/(Ta atom) based on the calculated difference in formation energy between the solid solution and the phase-separated convex hull in Figure 3.10a. Image reproduced with permission from ref.[51]. Copyright 2024.

3.6 Experimental Verification of Phase-field Model

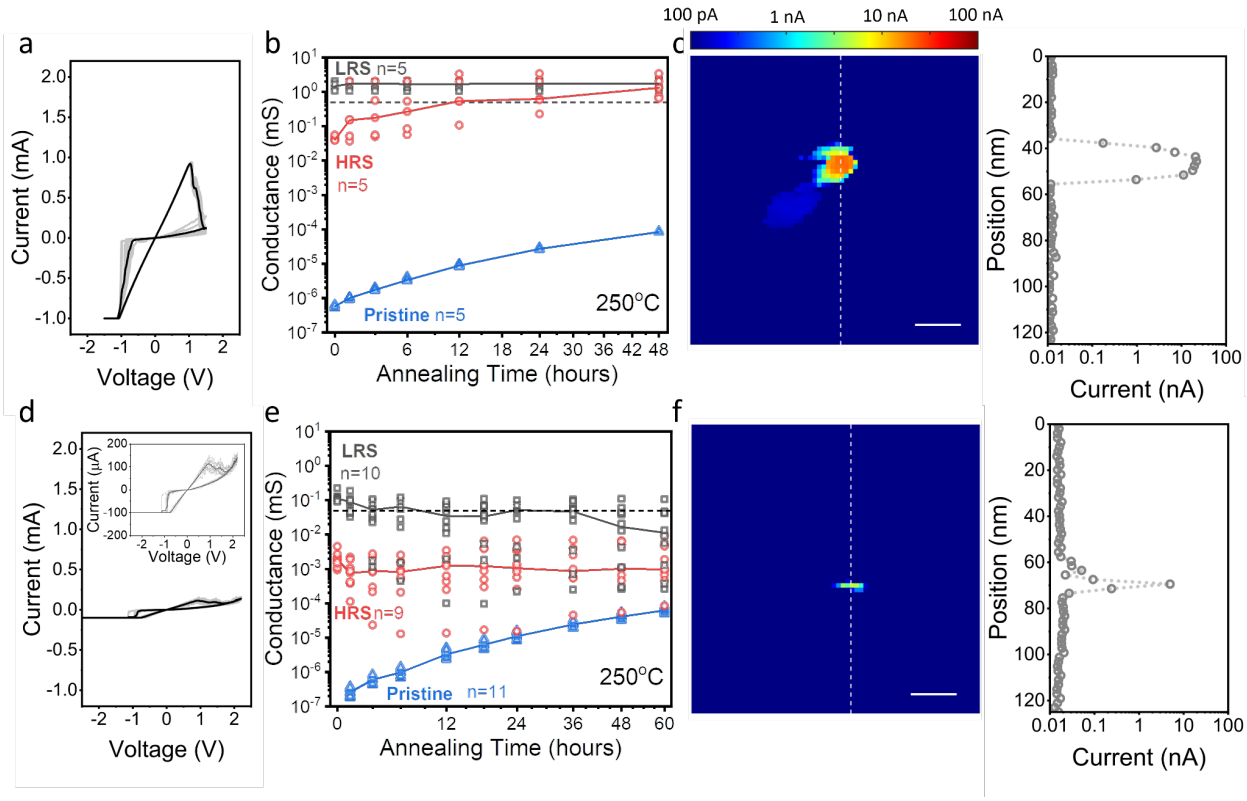


Figure 3.19: Filament size and stability under different compliance currents. (a) Typical resistive switching behaviour of a device with a 1 mA compliance current. (b) Retention characteristics of devices from the pristine state, HRS, and LRS baked at 250 °C. HRS devices failed to the low-resistance state. (c) Conductive Atomic Force Microscopy (C-AFM) in LRS devices with 1 mA compliance current shows a larger filament with a diameter ~8 nm. Scale bar is 20 nm. (d) Typical resistive switching behaviour of a device with a smaller 100 μA compliance current. (e) Retention characteristics of devices from the pristine state, HRS, and LRS baked at 250 °C. LRS devices are unstable and fail during the retention measurement. (f) C-AFM maps in LRS devices with 100 μA compliance current show a smaller filament with diameter ~3 nm. Scale bar is 20 nm. See Figure 3.6 for all C-AFM images. Image reproduced with permission from ref.[51]. Copyright 2024.

Based on our predictions from Figure 3.17, we experimentally identified the transition from HRS failure (red) to LRS failure (blue). Our results in Figure 3.19 show that reducing the compliance current from 1 mA to 100 µA not only decreases the filament conductance, but also yields in a transition from HRS failure to LRS failure. Additional c-AFM measurements show this reduction in compliance current reduces the filament size from ~8 nm to ~3 nm (Figure 3.19 c,f). The latter value (3 nm) is comparable to scalpel c-AFM images showing a ~4 nm diameter filament in a Hafnia device SET using a 50 µA compliance current[49]. These combined c-AFM and device

characterization results confirm our model prediction of a transition from HRS to LRS failure with smaller filaments (Figure 3.17d). In contrast, models based on Fick's First Law would suggest that larger filaments dissolve slower due to longer diffusion lengths, not the observed dichotomy in the direction of failure in our experiments.

Next, to experimentally obtain the predicted "green" region without retention failure, we used a larger RESET voltage of 2.5V (Figure 3.20). These 2.5V RESET devices (HRS2) have ~4 orders of magnitude higher resistance than the 1.5V RESET devices (HRS1) on the same die. Based on previous research, this vast increase in the filament resistance most likely results from an increase in the filament gap[50]. Using the Simmons equation[51] with a barrier height of 1.5 eV, a filament diameter of 8 nm, and an electron effective mass of 1, we estimate from the measured HRS resistance that the filament gap increased from ~0.4 nm to ~0.9 nm upon increasing the RESET voltage from 1.5 to 2.5V (Figure 3.21). We note that these estimates are based on idealized planar barriers, which do not account for deep traps as well as non-planar barrier shapes; additionally, while the Simmons equation may not be physically realistic for tunnel gaps <0.5 nm, the experimentally measured decrease in conductance upon a 2.5V RESET (Figure 3.17e) should correspond to an increase in the tunnel gap. After 1 hour baking at 250 ºC, the HRS2 devices showed a decrease in conductance, qualitatively consistent with the predictions in Fig 6c whereby the gap increases over time. Over 48 hours, the conductance of the HRS2 devices converges with that of the pristine devices, again consistent with the predictions in Figure 3.17c. In contrast, the resistances of the HRS1 devices will converge with the LRS, consistent with Figure 3.17a. While the longer retention times may not outweigh the higher switching voltages, our results do provide strong experimental evidence for our phase-field model.

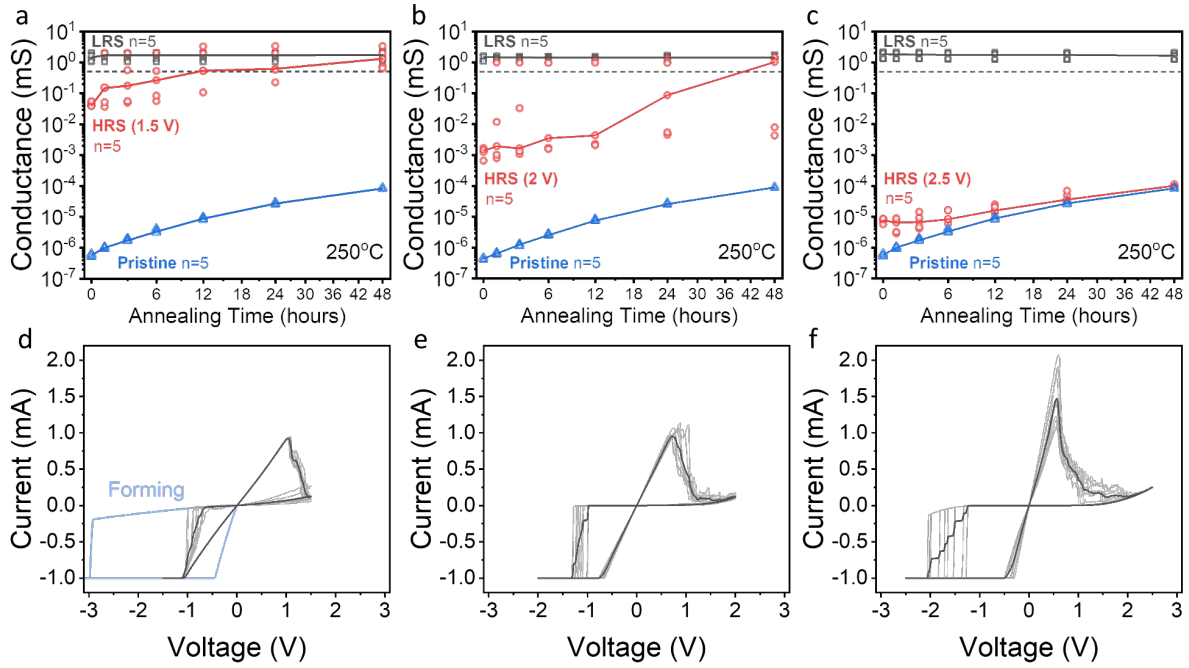


Figure 3.20: Switching and retention properties of the bilayer TaO_X-based memristors using different RESET voltage. (a-c) Retention characteristics of devices from the pristine state, HRS, and LRS baked at 250 °C with RESET voltage of (a) 1.5 V, (b) 2 V, and (c) 2.5 V. (d-f) Typical resistive switching behaviour with RESET voltage of (d) 1.5 V, (e) 2 V, and (f) 2.5 V. The 2V RESET shows that about half the devices failed after 48 hours. Image reproduced with permission from ref.[51]. Copyright 2024.

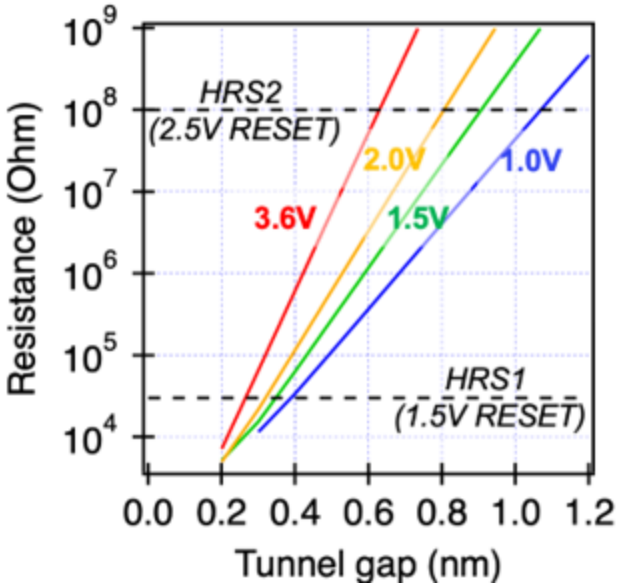


Figure 3.21: Results of the Simmons equation[74] with different calculated barrier heights. Based on the c-AFM results, we estimate the diameter of the filament to be 8 nm. The barrier should be less than half of the bandgap (~4 eV in Ta_2O_5). The average measured resistances of the HRS devices from Figure 3.17e are marked as horizontal dashed lines. Image reproduced with permission from ref.[51]. Copyright 2024.

3.7 Conclusion

In this chapter, we have explored the thermodynamic origins of nonvolatility in ReRAM through the phase separation hypothesis, particularly focusing on tantalum oxide-based devices. Our investigation highlights the limitations of the traditional Fickian diffusion model, which fails to account for the observed experimental behavior, such as the unexpected strengthening of conductive filaments and the inconsistencies in resistance states over time. Through both experimental evidence and computational simulations, we demonstrate that compositional phase separation offers a more accurate explanation for the retention characteristics of ReRAM. The identification of phase-separated regions and the stability of these regions under varying conditions suggest that the nonvolatility of ReRAM devices is deeply rooted in the thermodynamics of phase separation rather than simple diffusion processes. This understanding not only resolves long-standing discrepancies in ReRAM behavior but also provides a framework for optimizing device performance through careful control of material compositions and processing conditions. Future research can build on this foundation to further refine models of ReRAM operation and enhance the reliability and efficiency of these promising memory devices.

Chapter 4 Composition-dependent Diffusion in ReRAM

4.1 Composition-dependent Diffusion Hypothesis

With our HRS retention failure results, I also approximate the retention time using the characteristic oxygen (vacancy) diffusion time[39,53,75] and extracted the Arrhenius activation energy (E_A). Our HRS results, as well as previous literature results, suggest that the retention (diffusion) time can be modelled using E_A~1.5 eV (Figure 4.1). However, direct oxygen diffusion measurements of Ta_2O_5 show that E_A ranges between 0.8 and 1.2 eV[72,76], which predicts ~5-12 orders of magnitude faster oxygen diffusion and shorter device retention times[72,76,77].

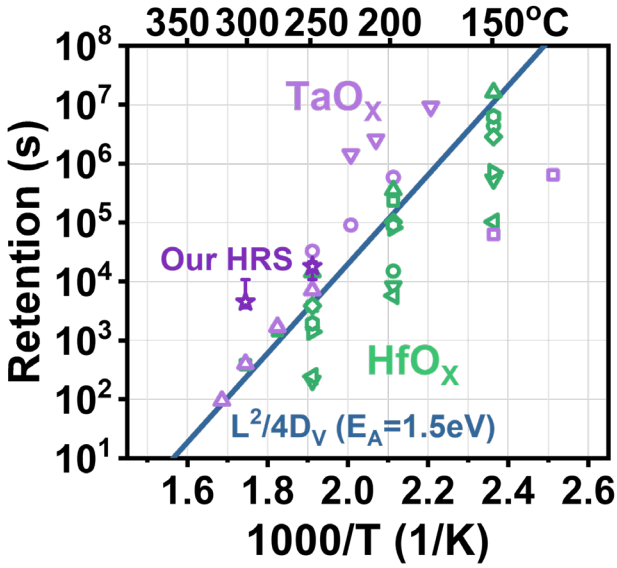


Figure 4.1: Review of the literature on RRAM retention based on TaO_X[5,7,38,39] and HfO_X[36,55,78]. While it is difficult to obtain an activation energy in our work, our retention times are similar to past work which suggests an activation energy of around 1.5 eV (blue line). Our LRS retention failure time is much longer than previously reported because most work only identifies the state that fails faster (LRS or HRS). Image reproduced with permission from ref.[51]. Copyright 2024.

Therefore, in addition to the substantial deviations in direction from ideal diffusion in ReRAM, there are unexplained inconsistencies with experimental data on retention magnitude. When using experimentally-derived diffusion constants for tantalum oxide[56,77], this model underestimates the measured retention time by 5-10 orders of magnitude[5,53] (Figure 4.2).

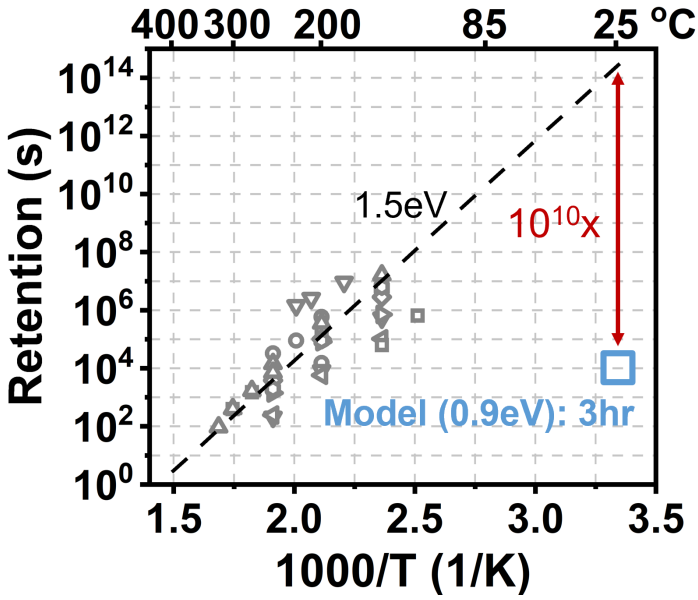


Figure 4.2: Ten orders of magnitude discrepancy between standard model and published experiment results.

We hypothesize that oxygen diffusion in tantalum sub-oxides is much slower and has higher activation energy compared to Ta_2O_5. Whereas the retention time is determined by the oxygen diffusivity of the TaO_X sub-oxides that make up the filament, past results only quantified diffusion in the oxidized Ta_2O_5.

4.2 Oxygen Tracer Diffusion in TaO_X

To test our hypothesis, we quantified oxygen tracer diffusion in Ta (sub)-oxides using trilayer structures that consist of $Ta^{16}O_X/Ta^{18}O_X/Ta^{16}O_X$ (X~0.7, 1.5, 2.5). The isotope-enriched center layer is formed using $^{18}O_2$-enriched gas in the reactive sputtering gas mixture (Figure 4.3a). We then anneal these structures and use Time-of-Flight, Secondary Ion Mass Spectrometry (ToF-

SIMS) to determine the $^{18}O/^{16}O$ ratio as a function of depth. Directly incorporating the tracer ^{18}O into the film enables tracer diffusion measurements in highly reduced sub-oxides, which cannot be accessed in standard gas-phase isotope exchange.

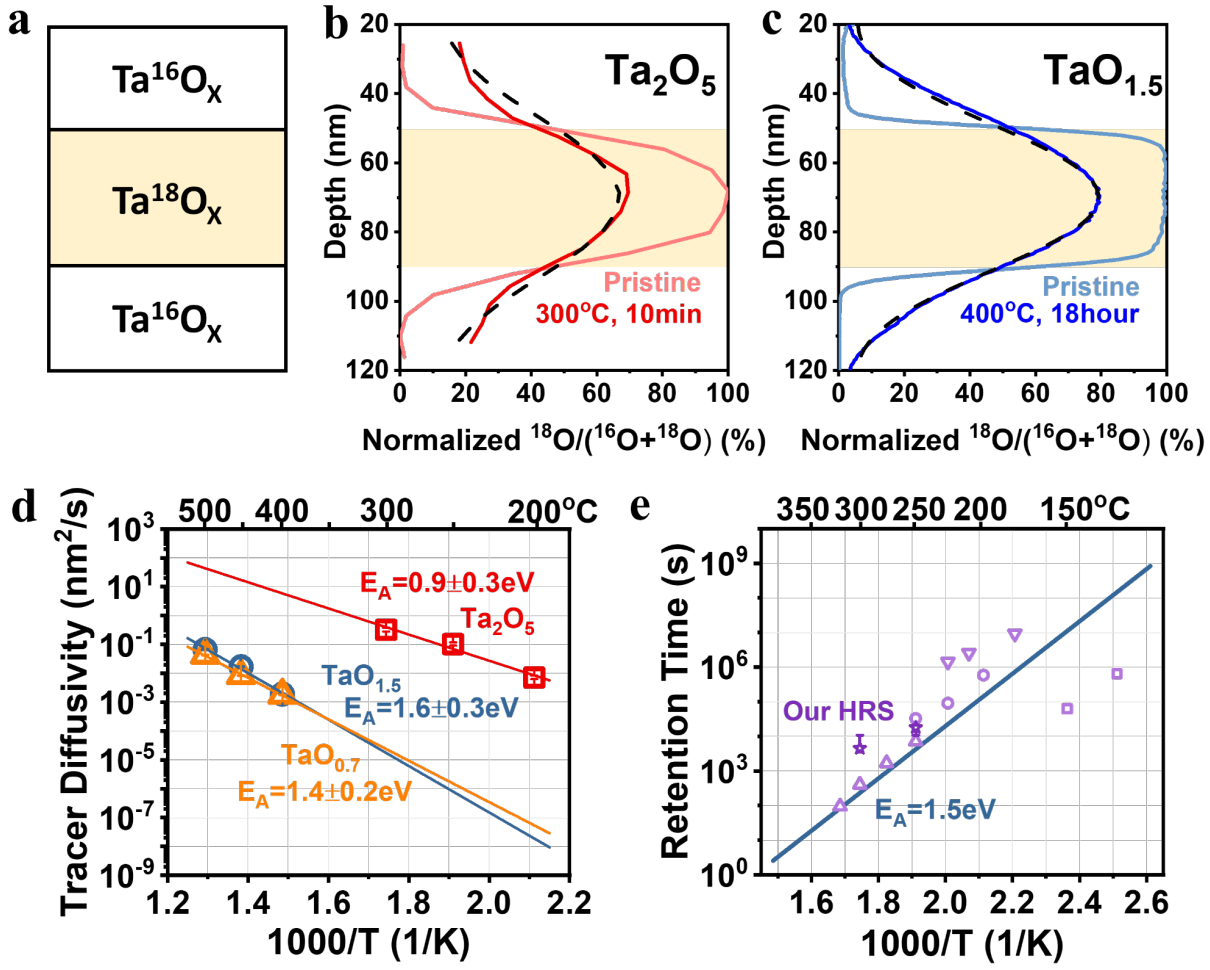


Figure 4.3: Diffusion kinetics of TaO_X with ToF-SIMS and effects on retention failure. a) We develop a novel trilayer sample structure that embeds the ^{18}O tracer into the film stack, eliminating gas-phase reaction and enabling suboxide tracer diffusion measurements. b-c) Tracer diffusion results of Ta_2O_5 (b) and $TaO_{1.5}$ (c) trilayer samples. Black dotted line shows the fitted Fourier series solution to the diffusion equation. Sub-oxide $TaO_{1.5}$ shows much slower diffusivity compared with that of oxidised Ta_2O_5. d) Fitted activation energy of oxygen tracer diffusivity in TaO_X. Ta_2O_5 shows ~0.6 eV lower activation energy (E_A) than that of sub-oxides. The error indicates the 95% confidence error for the activation energy fits. **e)** Comparison of characteristic diffusion time with the vacancy diffusivity estimated from the tracer diffusion activation energy in ToF-SIMS experiments with experimental retention times. The diffusion time activation energy of sub-stoichiometric oxides match well with retention time of TaO_X devices from literature (light purple)[5,7,38,79]. Image reproduced with permission from ref.[51]. Copyright 2024.

In Figure 4.3b and c, we show oxygen tracer diffusion profiles for the oxidised Ta_2O_5 and the $TaO_{1.5}$ sub-oxide, respectively. While the Ta_2O_5 film shows substantial tracer diffusion after

just 10 minutes at 300°C, the sub-oxide requires over 18 hours at 400°C to observe a similar tracer concentration profile. Our results yield a tracer diffusion activation energy of 0.9±0.3 eV for the amorphous Ta_2O_5 film, and between 1.4±0.2 and 1.6±0.3 eV for the two sub-oxides $TaO_{0.7}$ and $TaO_{1.5}$ (Figure 4.3d, see fitting in Figure 4.4). This reduction in diffusivity with higher oxygen vacancy concentration has also been observed in $SrTiO_3$[80].

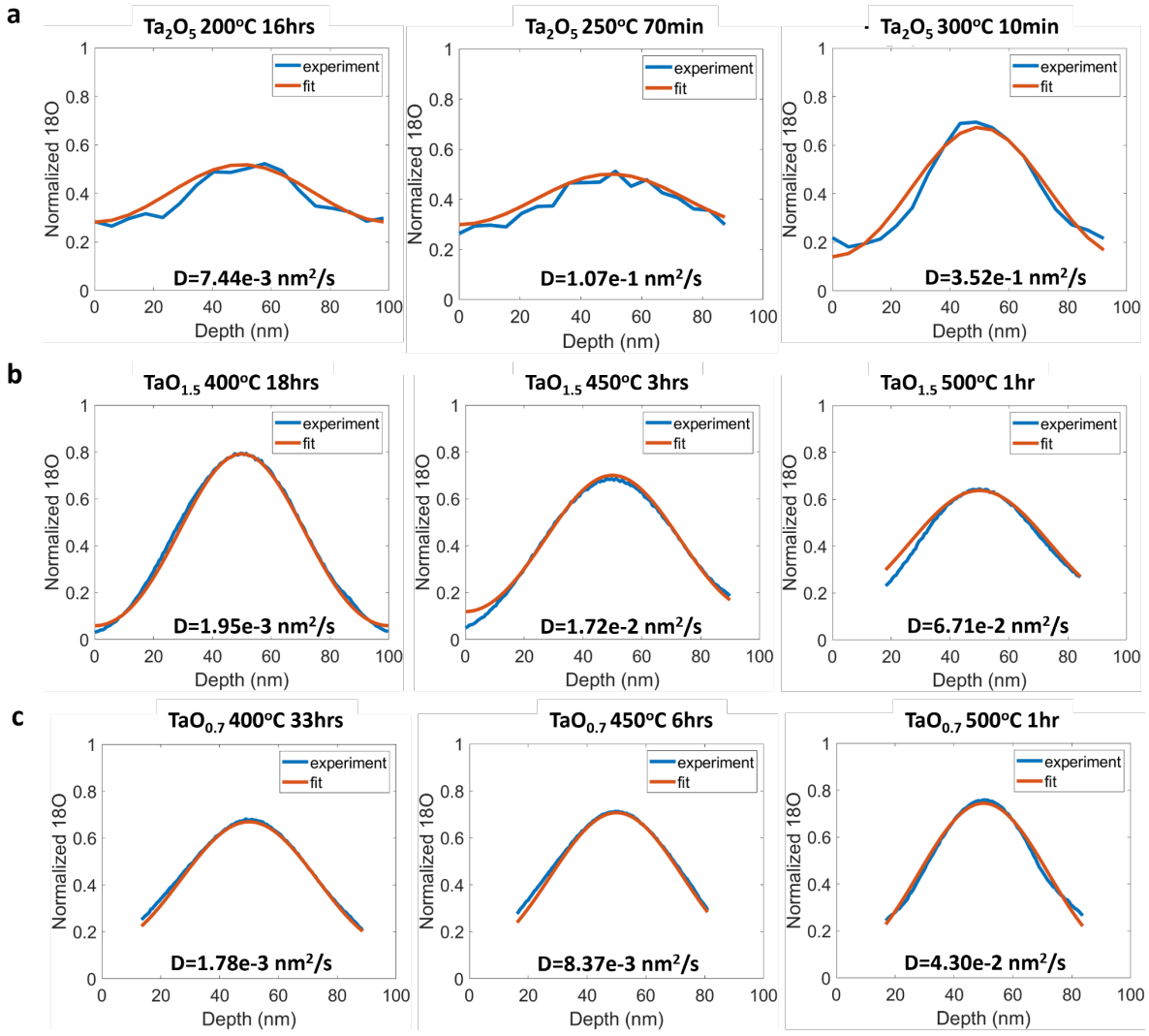


Figure 4.4: ToF-SIMS results and fitting for tracer diffusivities of (a) Ta_2O_5, (b) $TaO_{1.5}$, and (c) $TaO_{0.7}$ at different temperatures. Image reproduced with permission from ref.[51]. Copyright 2024.

The much slower oxygen diffusivity in the sub-oxides explains the excellent retention time. In Figure 4.3e, we show that the retention time activation energy for the unstable state, HRS in our

case, is ~1.5 eV, consistent with the higher ~1.5 eV activation energy of the sub-oxide. However, our stable state (LRS) has even longer retention and does not appear to fail. As we will explain next, this remarkable stability cannot be explained only by oxygen diffusion rates.

4.3 Retention Simulation with Composition-dependent Diffusivity

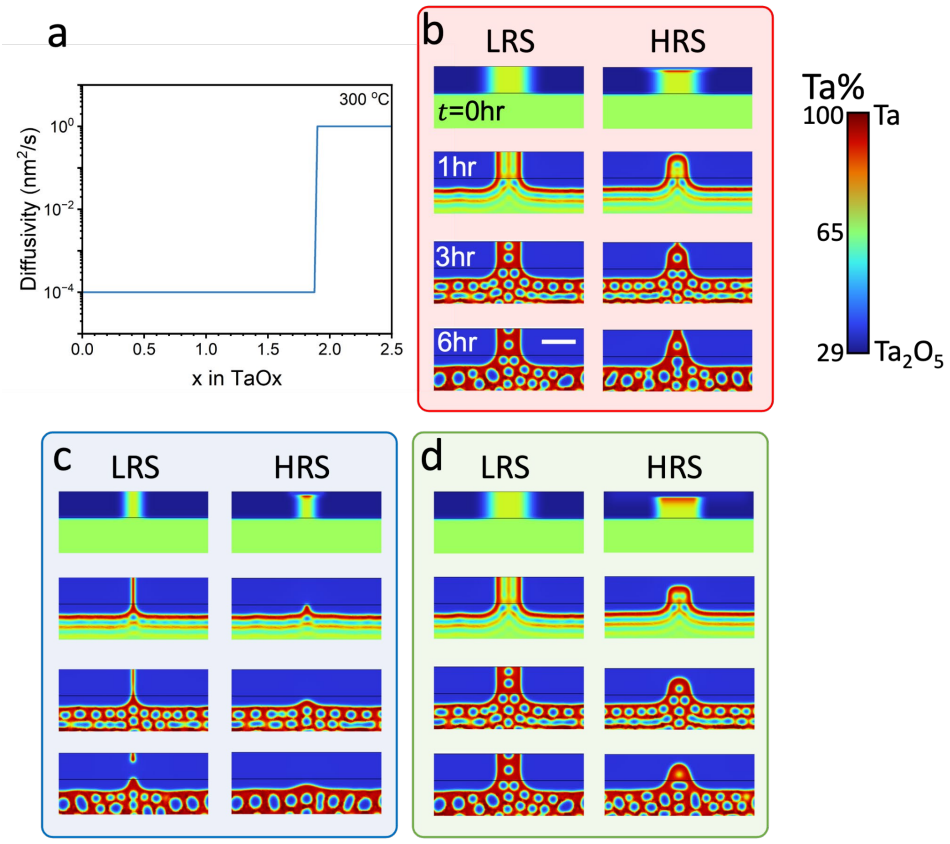


Figure 4.5: Simulated evolution in LRS and HRS devices with composition-dependent diffusion parameter. (a) The assumed composition-dependent oxygen diffusivity based on the tracer diffusion measurements in Figure 4.3. (b-d) The simulation of three different retention regions shows essentially identical results with that in Figure 3.17. Image reproduced with permission from ref.[51]. Copyright 2024.

In Figure 4.5 and 4.6, we incorporated a composition-dependent oxygen diffusivity into our model. While the magnitudes and paths differ, the overall trend is essentially identical to what was observed with a composition-independent oxygen diffusivity. This results because the final state of the system is ultimately governed by thermodynamics: changing the magnitude and shape

of diffusivity can change the time and path needed to reach this final state, but it cannot change the final form.

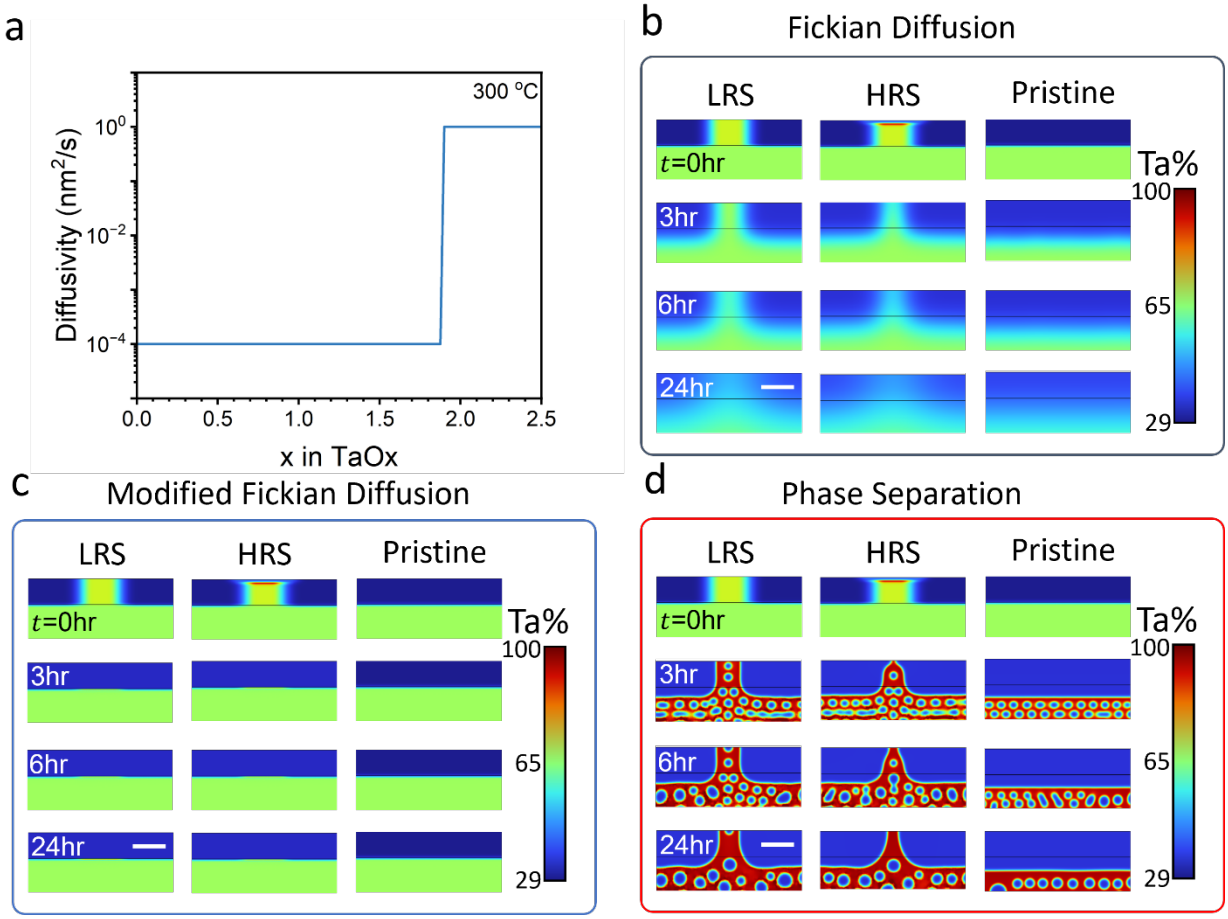


Figure 4.6: Simulated evolution in LRS and HRS devices with composition-dependent diffusion parameters. (a) The composition-dependent oxygen diffusivity interpolated from the tracer diffusion measurements in Figure 4.3. (b) Simulation of Fickian diffusion model without suppressing oxygen transport at the interface. Here, the filament dissolves, in contrast to Figure 3.16a, because there is not enough time to equilibrate with the deeper metal-rich suboxide with low oxygen diffusivity. (c) The modified Fickian diffuison model suppresses oxygen transport between the two layers, and results in the rapid failure of the LRS state, consistent with Figure 3.16b. (d) Like Figure 3.16c, only the regular solution phase separation model can predict the stability of the LRS and the failure of the HRS. Image reproduced with permission from ref.[51]. Copyright 2024.

4.4 Conclusion

In this chapter, we explored the composition-dependent diffusion hypothesis to better understand the retention behavior of ReRAM, particularly focusing on the discrepancies between ideal diffusion models and experimental data. Our findings demonstrate that traditional models

significantly underestimate retention times, likely due to the failure to account for the slower oxygen diffusion in sub-oxides compared to fully oxidized Ta_2O_5. By quantifying oxygen tracer diffusion in various TaO_X compositions, we identified a much higher activation energy for sub-oxides, which better aligns with observed retention times. Our retention simulations incorporating composition-dependent diffusivity further supported these findings, showing that while the pathway to the final state may vary, the ultimate behavior is thermodynamically determined. These insights enhance our understanding of ReRAM retention and provide a foundation for optimizing device performance through material composition control.

Chapter 5 Thermodynamic Engineering for ECRAM

5.1 Phase Separation Enables Nonvolatile Phenomena

Random-Access Memory (ECRAM) has recently emerged as a promising solution for analog computing[9,12,13,81] with oxygen ion, lithium ion, or proton. ECRAM, a three-terminal memory device, stores and switches information through ion migration and the resulting change in valence and electronic conductivity. ECRAM based on oxygen ion, operates by electrochemically transporting oxygen ions between two layers of transition metal oxides with a solid electrolyte. This mechanism allows ECRAM to switch resistance states by modulating oxygen concentration. ECRAM materials include titanium and tungsten oxide; while such materials possess analog states and are promising for neuromorphic computing, they do not fundamentally improve upon the 10 year, 85 ℃ retention time of conventional nonvolatile memory. Recently, We hypothesized that the inferior retention previously observed in ECRAM is linked to the use of solid solution materials[43]. To circumvent this, we focus on a two-phase transition oxide system, particularly the amorphous tantalum oxide system known for its exemplary retention performance in ReRAM[5,39]. Our studies reveal significant phases (Ta and $TaO_{1.9}$) in the amorphous tantalum oxide, and we demonstrate that amorphous phase separation markedly affects mass transport and composition evolution in ReRAM[82].

Building on these insights, we developed a high-temperature stable ECRAM device utilizing amorphous TaO_X, capable of functioning effectively at temperatures up to 600 °C. Comprehensive electrical measurements at these elevated temperatures revealed both binary and

multi-level switching capabilities with a stable On-Off ratio, persisting for over 24 hours at 500 °C, a notable advancement in memory device resilience. By combining transmission electron microscopy and phase-field modeling, we show that our information retention time is enabled by the compositional phase separation of amorphous tantalum oxide into multiple phases.

5.2 TaO_X-based ECRAM as High Temperature Binary Memory

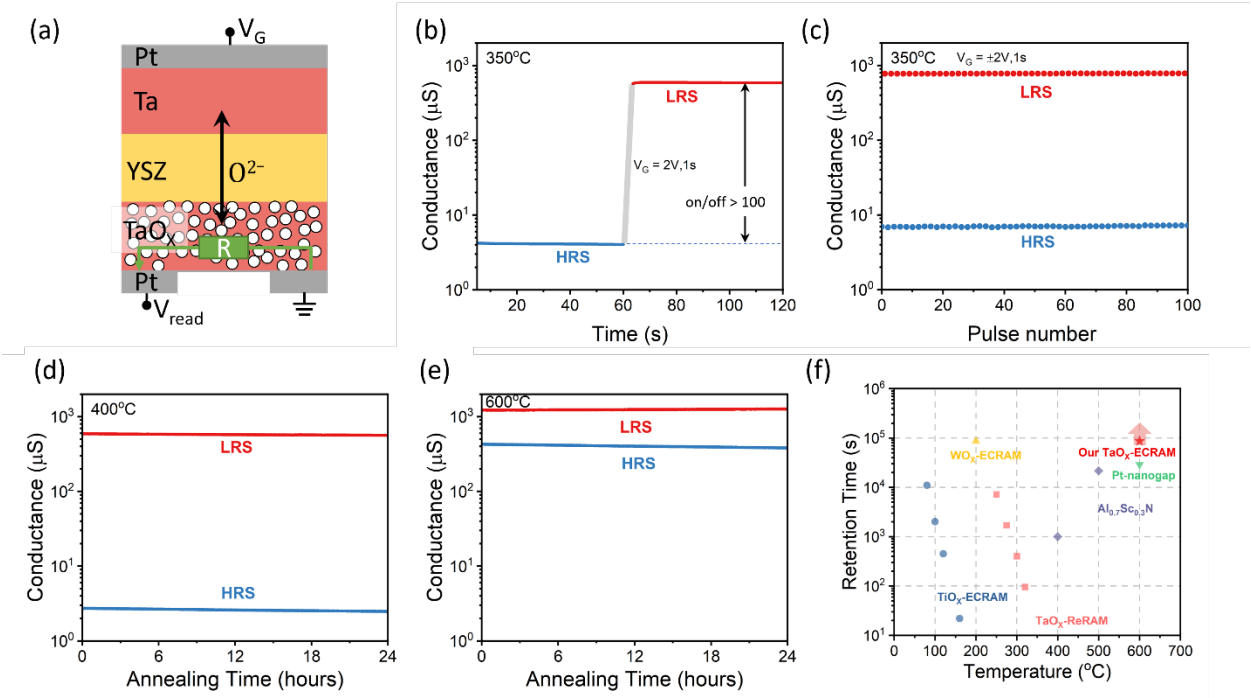


Figure 5.1: Binary switching and retention behaviors of ECRAM devices. (a) Schematic depicting the structure of the ECRAM device, featuring a stacked configuration of TaO_X/YSZ/Ta. This design utilizes an electric field to facilitate the movement of oxygen ions through the YSZ electrolyte, effectively modulating the oxygen concentration in the TaO_X channel oxide to enable the storage of information through the creation of varying resistance states in the device. (b) Binary switching behavior from HRS to LRS with one pulse (2V, 1s) at 350°C showing a higher than 100 on/off ratio. (c) 50 cycle switching between LRS and HRS with minimal cycle-to-cycle variation. (d-e) The retention measurements of two resistance states at 400°C (d) and 600°C (e) for 24 hours without failure. (f) Retention times of various memory devices including our ECRAM with TaO_X, Pt nanogap devices[18], $Al_{0.7}Sc_{0.3}N$ ferroelectric capacitors[29,83], ReRAMs based on TaO_X[5], and ECRAMs utilizing TiO_X[9] and WO_X[43], showcasing our device's exceptional performance of our device in data retention capabilities across these diverse technologies.

Our TaO_X-ECRAM cells consist of a 20 nm reservoir layer of tantalum, a 140 nm electrolyte layer of yttria stabilized zirconia (YSZ) electrolyte, and a 20 nm channel layer of amorphous oxygen-deficient tantalum suboxide (TaO_X) deposited on SiO_2 (500 nm)/Si substrates

using reactive sputtering (Figure 5.1a). Three Pt current collectors are sputtered using shadow masks. Finally, a passivation layer of SiN is deposited to reduce the oxidation of tantalum oxide with the environment. We switch this device by a positive or negative gate voltage (V_G, Figure 5.1a); during retention measurements, we ground the gate by applying 0 V, short-circuiting it to the channel. Unlike earlier works, no switch or selector was used in these experiments.

We initially focused on examining the binary switching behavior. Figure 5.1b illustrates the SET process, showcasing a >100 on/off ratio differentiating between the high resistance state (HRS) and low resistance state (LRS) with $\pm$ 2V for 1second. This SET/RESET switching is reproducibility, as evidenced by Figure 5.1c, demonstrating 50 switching cycles with minimal cycle-to-cycle variation. We observed that resistance switching could be effectively obtained across a broad temperature range, spanning from 200°C to 600°C (Figure 5.2), rendering this technology adaptable for diverse high-temperature applications. Moreover, rigorous endurance tests of 10000 pulses at 400°C further underscored the erasable nonvolatile memory's potential at high temperatures (Figure 5.3). In addition, we conducted a comprehensive examination of temperature's influence on switching behavior, utilizing a consistent 2V 1s pulse across a temperature span from 300°C to 550°C (see Figure 5.4). Our findings reveal that temperatures ranging between 350°C and 400°C exhibit the most substantial on/off ratio (>100) under the 2V 1s pulse condition. However, temperatures below 300°C impede sufficient ion migration, while temperatures exceeding 450°C elevate the HRS conductance. Similar temperature-dependent behavior was also observed with a short 2V 100 ms pulse (Figure 5.5).

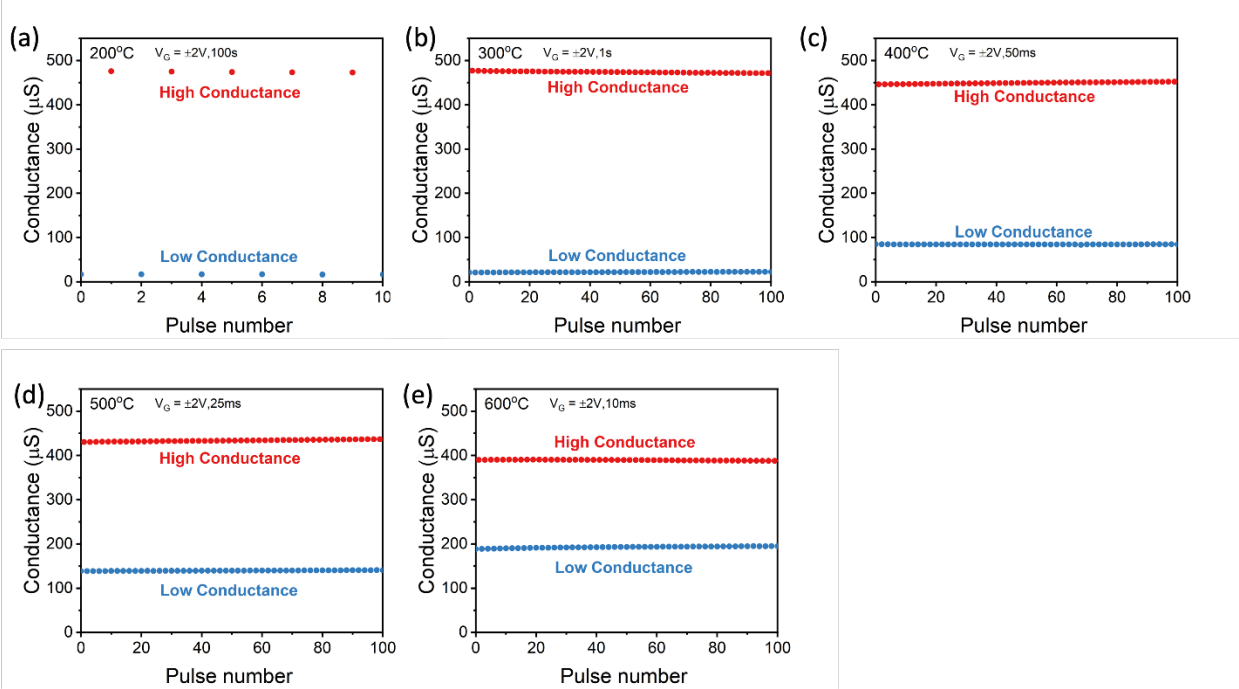


Figure 5.2: 50 cycle switching between LRS and HRS with minimal cycle-to-cycle variation across a broad temperature range, spanning from 200°C to 600°C.

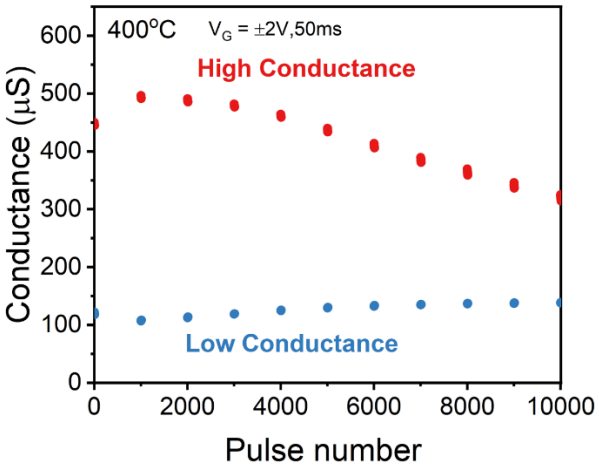


Figure 5.3: Endurance tests of 10000 pulses at 400°C.

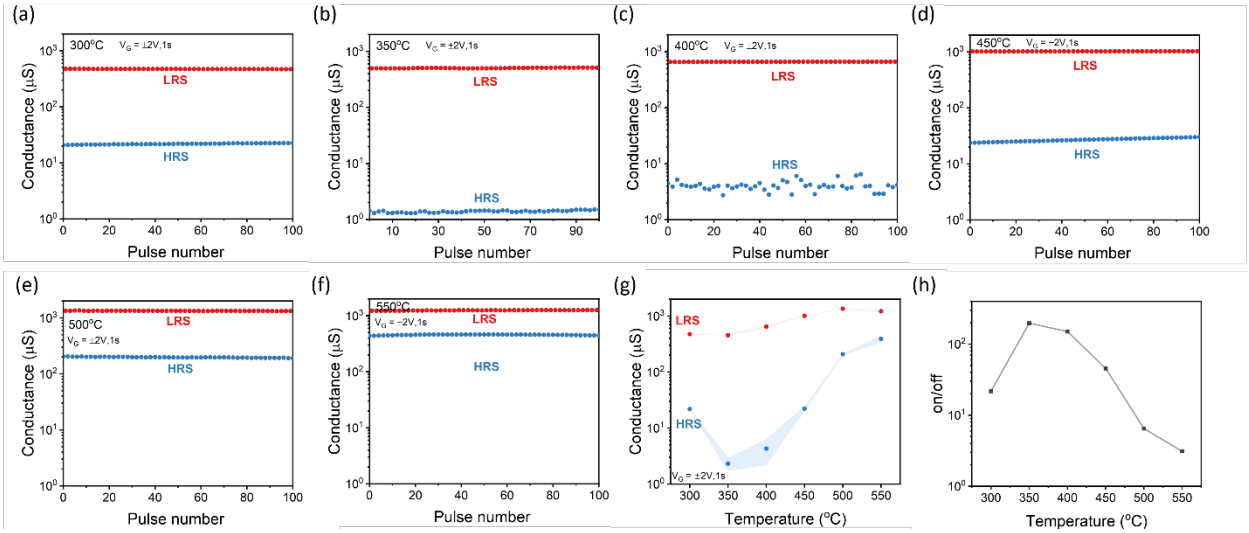


Figure 5.4: 50 cycle switching between LRS and HRS with ±2V 1s pulse across a broad temperature range, spanning from 300°C to 550°C. The device operated at 350-400°C shows the largest on/off ratio.

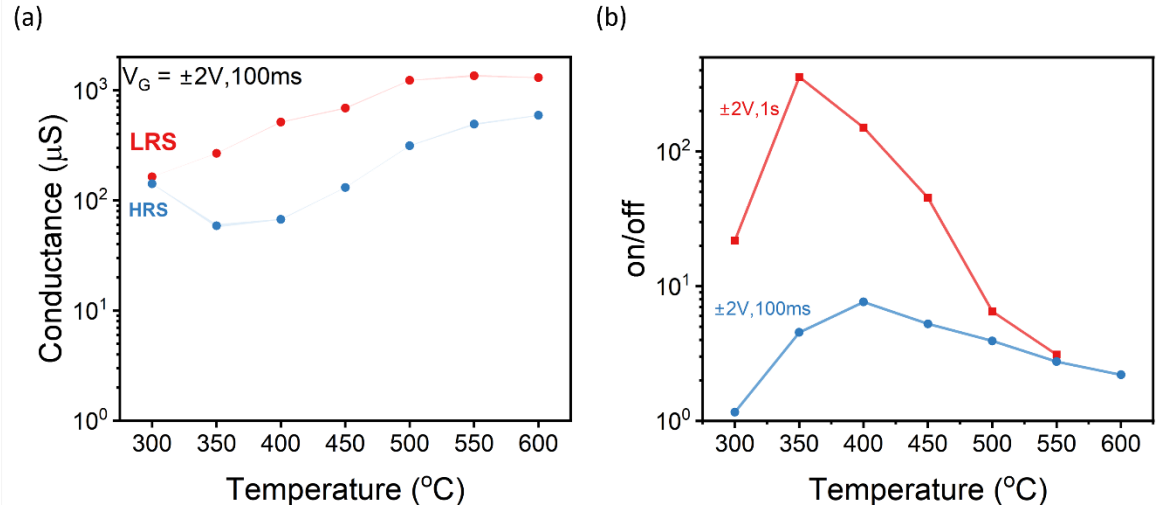


Figure 5.5: 50 cycle switching between LRS and HRS with ±2V 100ms pulse across a broad temperature range, spanning from 300°C to 600°C. Results from both 100 ms and 1 ms pulses demonstrate that the device operated at 350-400°C shows the largest on/off ratio.

Our results showed information retention exceeding 24 hours at temperatures ranging between 400°C to 600°C, affirming the stability of the programmed binary states without any sign of degradation (Figure 5.1d-e, Figure 5.6). A comparative analysis of the retention times between our TaO_X-ECRAM and other high temperature memory technologies (Figure 5.1f), highlighted our device's superior performance. Our ECRAM already surpasses other emerging high-

temperature memories, like Pt-nanogap ReRAM[18] and $Al_{0.7}Sc_{0.3}N$ ferroelectric capacitors[29], in both duration and temperature. ECRAMs utilizing TiO_X[9] and WO_X[43] show much worse retention compared to our TaO_X ones. Moreover, while these ReRAM devices yield best retention performance among emerging memory technologies at commercial temperature range, the retention times observed in our ECRAM cells, utilizing the same materials, surpassed them by more than ten orders of magnitude. This stability will be elaborated upon in subsequent sections, leveraging a comprehensive analysis encompassing materials characterization and model simulation.

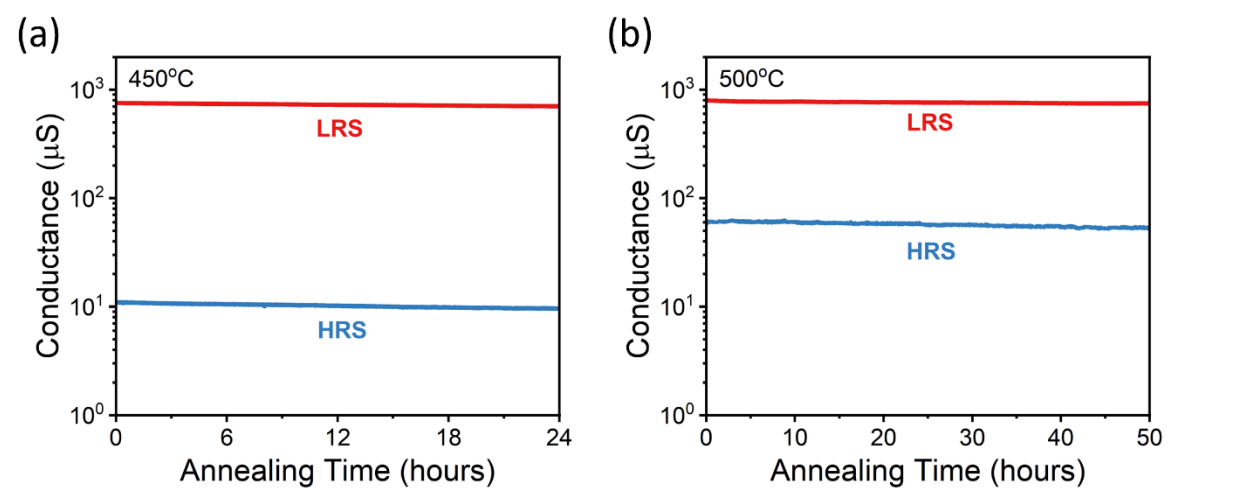


Figure 5.6: Retention test over 24 hours at 450°C and 500°C. No significant change in conductance was observed in both LRS and HRS.

5.3 Electron Microscopy Reveals Compositional Phase Separation

To shed light on the mechanism of the above resistive switching and retention behaviors in TaO_X-based ECRAM, we performed STEM and EDS on cross-sectioned devices. Figure 5.7a-b depict cross sectional STEM images and corresponding EDS mapping at the Ta K edge and O K edge from a pristine Ta/YSZ/TaO_2 device, confirming the presence of the Ta gate layer and the TaO_2 channel layer. Notably, Figure 5.7c-d illustrate STEM images and EDS mapping of Ta/O within a LRS device. A ~5 nm reduced Ta layer at the electrolyte/channel interface and a

corresponding ~15nm oxidized TaO_X at the gate/electrolyte interface are observed, indicative of the migration of oxygen ions from the channel layer through the electrolyte in response to the applied electric field, ultimately reaching the gate oxide. The increased thickness of the TaO_X interface may be attributed to the volumetric expansion occurring during the transition from Ta to TaO_X, while reduced Ta interface undergoes contraction due to the loss of oxygen ions. This intricate oxygen transport mechanism, previously posited in our prior investigations[82], is visually demonstrated for the first time through these electrochemical dynamics with ECRAM. These images not only explain the switching mechanism in ECRAM, but also contribute to comprehending the composition dynamics inherent in filamentary-type Valence Change Memory (ReRAM). In ReRAM, the existence of nanoscale conductive filaments with reduced components is believed to be pivotal for the phenomenon of resistive switching. However, such intricacies have been challenging to observe in TEM[52]. These findings bridge a critical gap in our understanding on the elusive nanoscale conductive filaments crucial for the operational principles of ReRAM-based memory devices.

We next investigate the LRS device following annealing at 400°C for 12 hours. This device remain essentially identical to those observed in the LRS device before annealing, indicating exceptional stability (Figure 5.7 c,d). This stability can be attributed to the phase separation within the device, which appears to play a crucial role in retaining the chemical state and, by extension, the electrical properties under thermal stress (Figure 5.1d-e). More specific, phase separation enables a very large, possibly continuous, number of analog equilibrium or near-equilibrium states in the miscibility gap between two stable phases (Figure 5.8), sharing the identical chemical potential, not only between the two different compositional layers in channel, but also between the

channel and gate. Therefore, no driving force exists to move the oxygen ions under short-circuit condition during retention measurements.

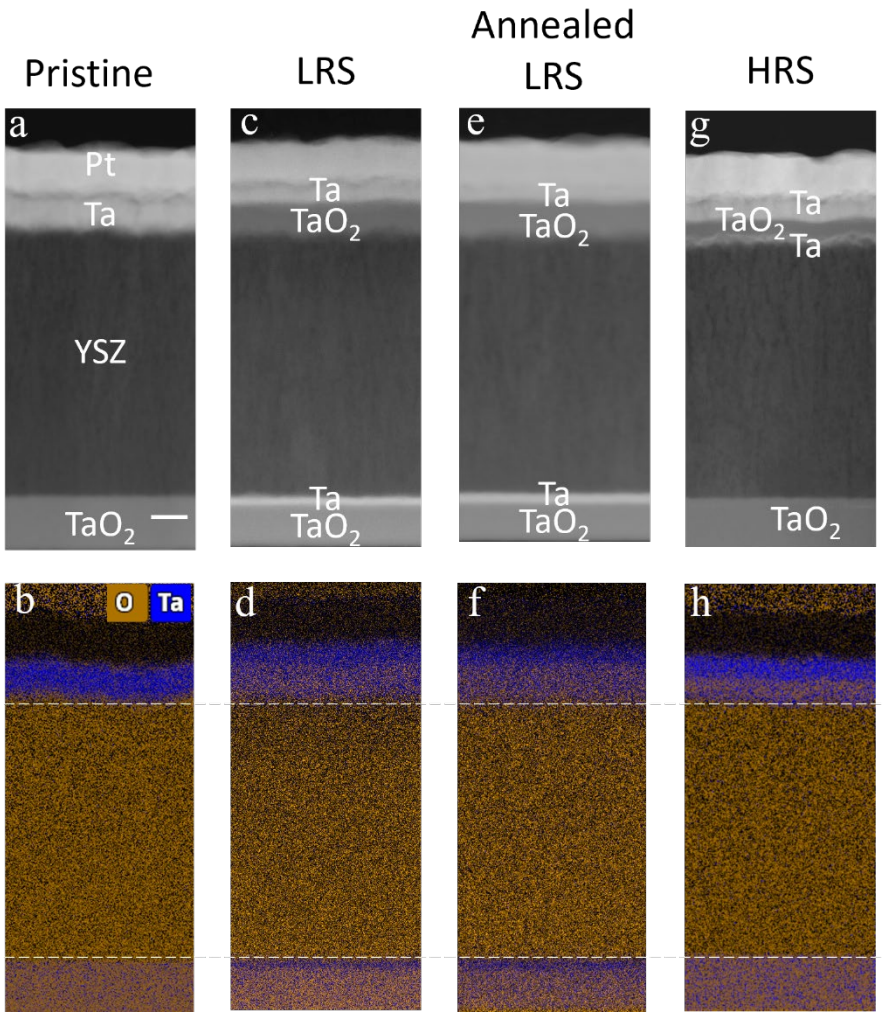


Figure 5.7: Field-directed migration and redistribution of oxygen ions showing the mechanism of switching and retention. (a-b) STEM (a), and the corresponding EDS mapping of O and Ta (b) in pristine devices. (c-d) STEM (c), and the corresponding EDS mapping of O and Ta (d) in LRS devices. (e-f) STEM (e), and the corresponding EDS mapping of O and Ta (f) in LRS device after 400°C annealing for 12hr. (g–h) STEM (g), and the corresponding EDS mapping of O and Ta (h) in HRS devices. Scale bar: 20 nm.

HRS is visually depicted in Figure 5.7g and corroborated by the EDS mapping in Figure 5.7h. The channel side closely resembles the pristine state, yet upon closer examination, residual traces of Ta are detectable at the bottom of the Ta interface in the LRS condition, accounting for the higher conductance seen in HRS relative to the pristine configuration. Conversely, the HRS is

characterized by a discernible reduced Ta layer at the reservoir-electrolyte interface, distinguishing it from both the pristine and LRS states. Further exploration of the HRS, particularly in the context of the phase separation and oxygen ion diffusion, will be elaborated upon in the subsequent section, through physical modeling.

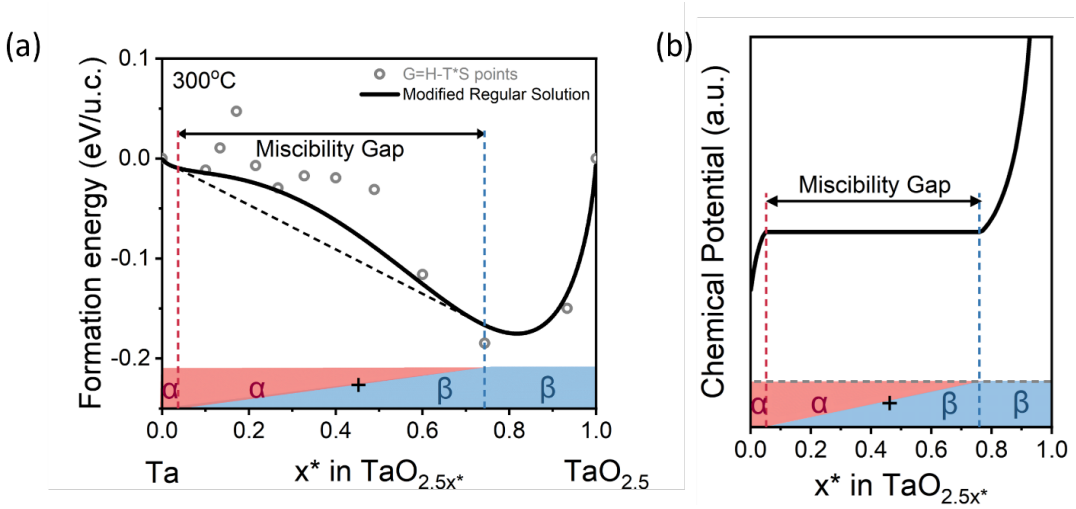


Figure 5.8: Computed formation energy and chemical potential of amorphous tantalum oxideS1. (a) Free energy curve fitted from DFT free energy points at 300oC and (b) corresponding oxygen chemical potential. ~Ta (***α***) and TaO1.9 (***β***) are identified as two stable phases in the amorphous tantalum-oxygen system.

5.4 Device Simulation of TaO_X-based ECRAM

Our above research demonstrates that phase separation is a strong candidate for the origin of non-volatility in ECRAM. Although phase separation conventionally characterizes the simultaneous presence of two distinct crystalline structures, we recently showed that phase separation between two amorphous states varying metal-to-oxygen ratios within amorphous tantalum oxides enables information retention in TaO_X resistive memory[82].

We combine the computed formation energy of amorphous tantalum oxide[82] (Figure 5.8) with a 2D phase-field model to simulate the switching and retention behaviors in our device (Figure 5.9). In this phase-field model, mass flux (J) follows the gradient of the computed chemical potential via $J = -D/k_B T\, c\, \nabla\mu + f$, where c is the oxygen concentration, D the oxygen

diffusivity, and *f* is the flux through the interface between YSZ electrolyte and TaO_X channel, which is controlled by the applied voltage and open circuit potential.

Figure 5.9a presents the simulation results of switching from pristine to LRS, and from LRS to HRS. We simulate a top layer of Ta and bottom layer of $TaO_{1.9}$. The first strong potentiation pulse (2V, 1s at 350°C) migrates O^{2-} ions from the bottom channel oxide layer, creating a ~5 nm reduced and conductive interface (t_2 in Figure 5.9d). The sharp interface indicates the phase separation of our system and thickness match well with TEM results of the LRS device. This interface conducts electrons and increases the device conductance from <10 μS to 600 uS, comparable to experiment (Figure 5.1b). We next simulate the switch from LRS to HRS with a -2V 1s pulse. The bottom reduced interface is oxidized again with the oxygen ions, while the top interface is also reduced. The HRS is more conductive than the pristine state, with a different-thickness reduced interface in the channel oxide layer. The HRS in the TEM is not fully reduced, similar to the HRS in our simulation (t_3 in Figure 5.9a).

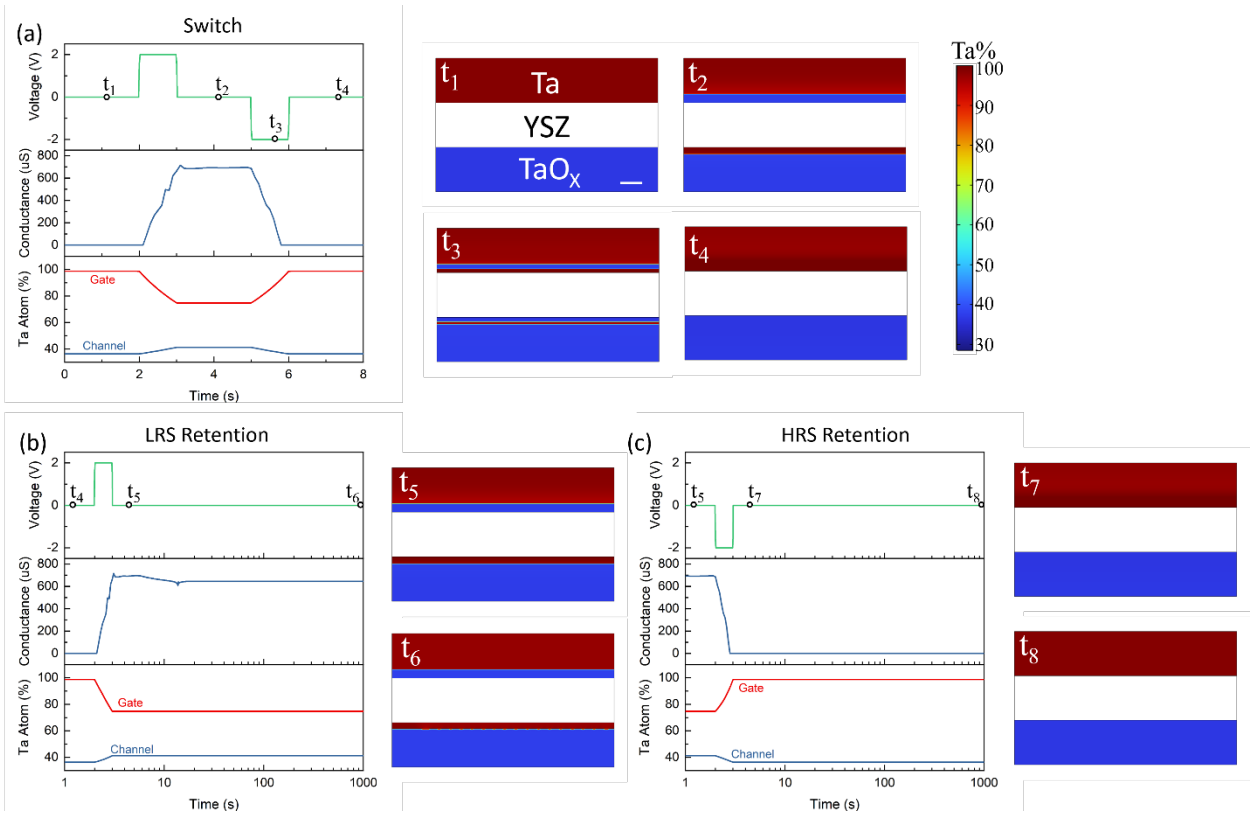


Figure 5.9: Phase-field model of migration and redistribution of oxygen ions during switching and retention. (a-c) Simulation of conductance and tantalum concentration dynamics during switching (a), LRS retention (b), and HRS retention (c). (d) The corresponding concentration mapping of Ta at different times in (a-c). Scale bar, 10 nm.

Figure 5.9b-c presents the simulated retention behavior of devices in LRS and HRS. The simulations reveal that, even under short-circuit conditions of retention measurements, the equilibrium in chemical potential between the top and bottom layers of tantalum oxide results in zero ion flux across the electrolyte, as shown in the lower panel of Figures 5.9b-c. Additionally, this equalized chemical potential allows for the simultaneous presence of both reduced and oxidized phases within the bottom channel layer, as indicated at t_6 in Figure 5.9b. This unique state represents a stable equilibrium for the device, a condition that is maintained not only in LRS but also during the HRS (t_8 in Figure 5.9c), suggesting a robust retention characteristic inherent to the device. This dual-phase stability is integral to the reliable operation of the ECRAM across its

various resistance states, highlighting the device's potential for non-volatile analog memory applications, as demonstrated in the following section.

5.5 Analog and Temperature-depending Switching

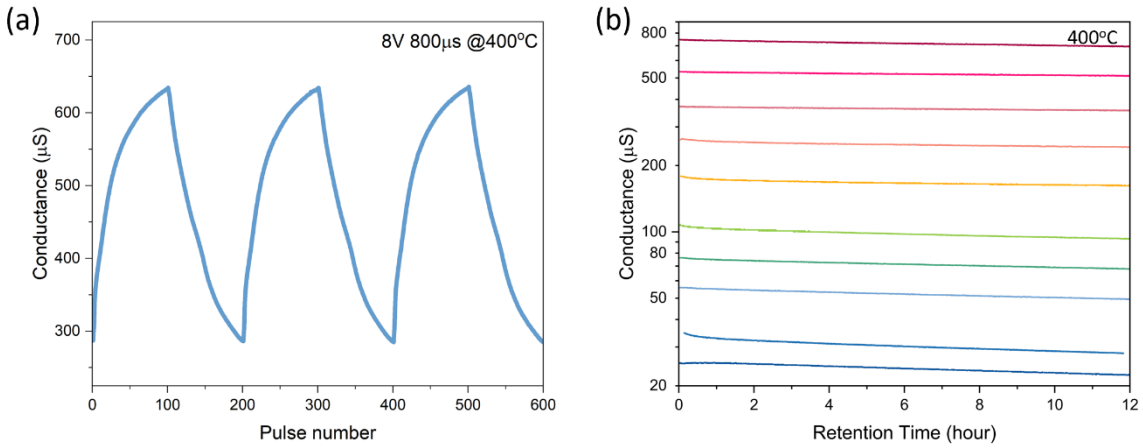


Figure 5.10: Analog switching and retention characterizations of the ECRAM. (a) Linear and symmetric conductance update in an ECRAM using a series of up/down pulsing cycles of different pulse widths at 400°C (100 pulses, ±8 V, 800 μs). (b) Retention test of >10 analog states over a wide switching window.

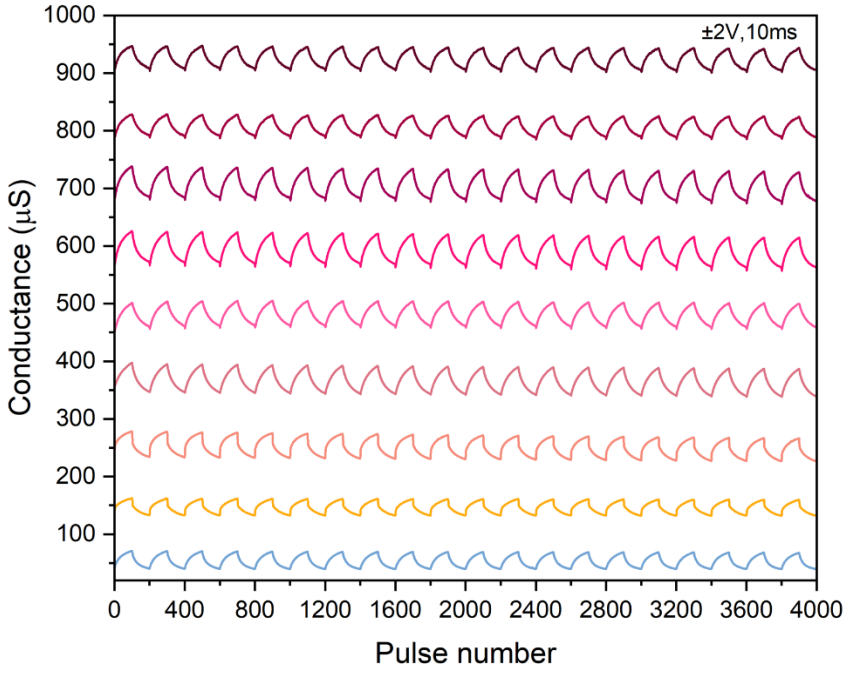


Figure 5.11: Analog behavior across a broad conductance range, spanning from µS to mS, demonstrating the device's potential for reliable analog switching in various computational tasks.

In addition to the binary switching, Our TaO_X-ECRAM cells also exhibit exceptional characteristics in its analog switching behavior, aligning with the traits observed in previous room-temperature ECRAM cells[10]. This device attains and sustains at least 100 distinct analog states through sub-millisecond pulses at 400°C, as illustrated in Figure 5.10a. These properties mirror those found in oxide ReRAM and highlight the device's pivotal ability for analog-analog matrix-multiplications, thus validating its importance in advancing computational frameworks. Of paramount significance is the consistent observation of a linear and symmetric update characteristic across the ECRAM cell, demonstrating an exceptional level of reproducibility and uniformity from cycle-to-cycle. Moreover, detailed investigation revealed that the ECRAM device manifests analog behavior across widely dispersed switching windows, spanning from the microsiemens to millisiemens range (as indicated in Figure 5.11). This reliability and consistency

further substantiate the device's potential for dependable analog data manipulation in various computational tasks. For example, analog switching with sub-microsiemens range can also been achieved in our device for low energy-consumption computation (Figure 5.12).

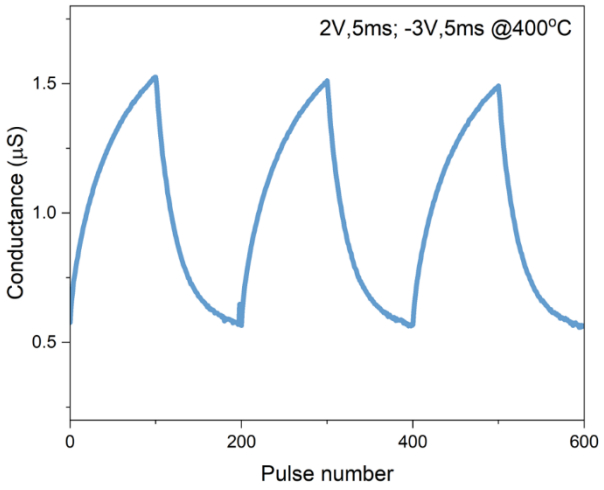


Figure 5.12: Analog switching at approximately 1 μS. This characteristic enables the device to be used for low energy-consumption computation.

A detailed investigation of the pulse condition on the switching includes pulse width and amplitude. In probing the analog switching behavior across pulse widths ranging from 500 μs to 4 ms at 8V (Figure 5.13a), the ECRAM device showcased an adjustable linear analog switching with pulse width. A similar behavior has been observed with a negative pulse (Figure 5.13b). This indicates that the device's conductance can be finely tuned by altering the duration of the applied pulses. Moreover, the study extended to examine the effect of pulse amplitude on the device's conductance. Figure 5.14 reveals that the conductance change is linearly proportional to the pulse amplitude. This finding aligns well with the linear relationship observed in previous TiO_2 ECRAM studies at elevated temperatures[9]. The linear relationship between the conductance change and pulse amplitude suggests that the device can be precisely controlled from pulse width.

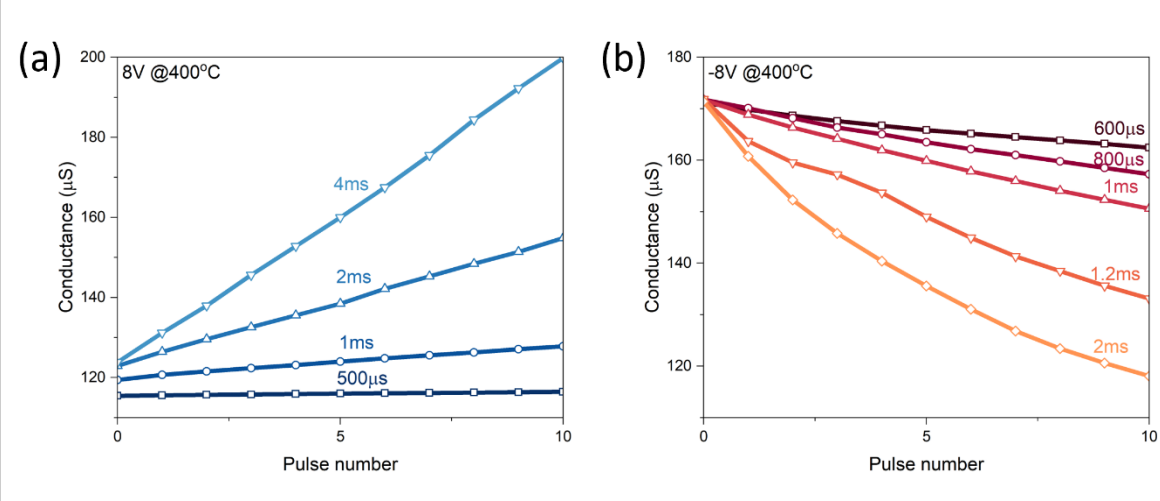


Figure 5.13: Analog switching with different pulse widths. Conductance can be finely tuned by the applied pulses with different pulse widths.

The thorough exploration of the analog switching behavior within the ambit of varying temperatures, specifically ranging from 250°C to 550°C, has unveiled intriguing insights into thermal stability and switching dynamics of our ECRAM devices (Figure 5.15 and 5.16). The transition from lower to higher temperatures demonstrated a noticeable augmentation in the switching speed within the device. As shown in the nonlinearity ($\boldsymbol{\alpha}$) factors in Figure 3.14h, at temperatures <= 400°C, the analog switching exhibited a consistent and measured response, maintaining its characteristic linear and symmetric behavior with α for both potentiation and depression close to 1 (ideal linearity)[84]. However, as temperatures increased to 450°C and subsequently to 550°C, discernible linearity shifts in analog switching behavior emerged with the α far from 1 with an expedited switching rate. Despite this change, the device still exhibited remarkable stability and reproducibility in its analog behavior, albeit with an accelerated pace and nonlinearity alterations in the switching windows, further illuminating the adaptability and resilience of the ECRAM in varying thermal conditions.

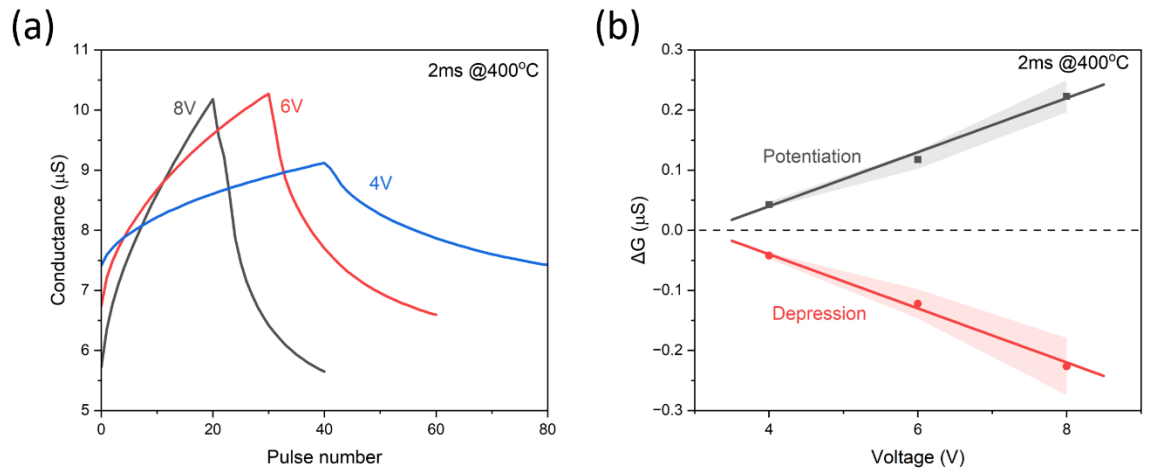


Figure 5.14: Analog switching with different pulse amplitudes. The conductance change is linearly proportional to the pulse amplitude, which enables precise control with pulse width.

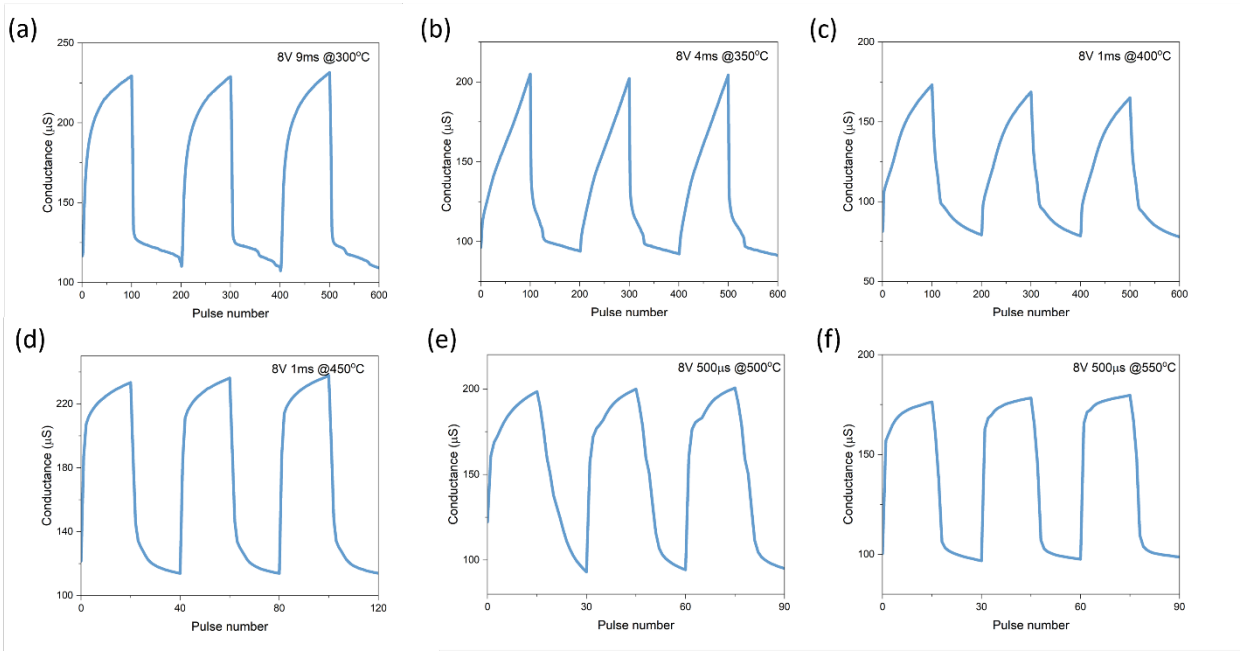


Figure 5.15: Analog switching with 8V pulse across a broad temperature range, spanning from 300°C to 550°C.

To validate the stability and stability of the programmed analog states within the ECRAM device, extensive data retention tests were conducted. Impressively, the programmed analog states ranging from 20 μS to over 800 μS exhibited remarkable stability even after a stringent 12-hour test period at 400°C, as depicted in Figure 5.10b. The observed phase separation phenomenon within our device contributes to the establishment of multiple equilibrium states, thereby

accounting for the existence of these stable states. Moreover, rigorous endurance tests involving 10,000 pulses with 100 distinct analog states at 300°C further highlighted the potential of the erasable nonvolatile memory for high-temperature applications (Figure 5.17). The ability to retain analog information and to sustain 10,000 pulses without substantial wear or loss of functionality make it a promising candidate for applications demanding prolonged and resilient data storage in extreme environments.

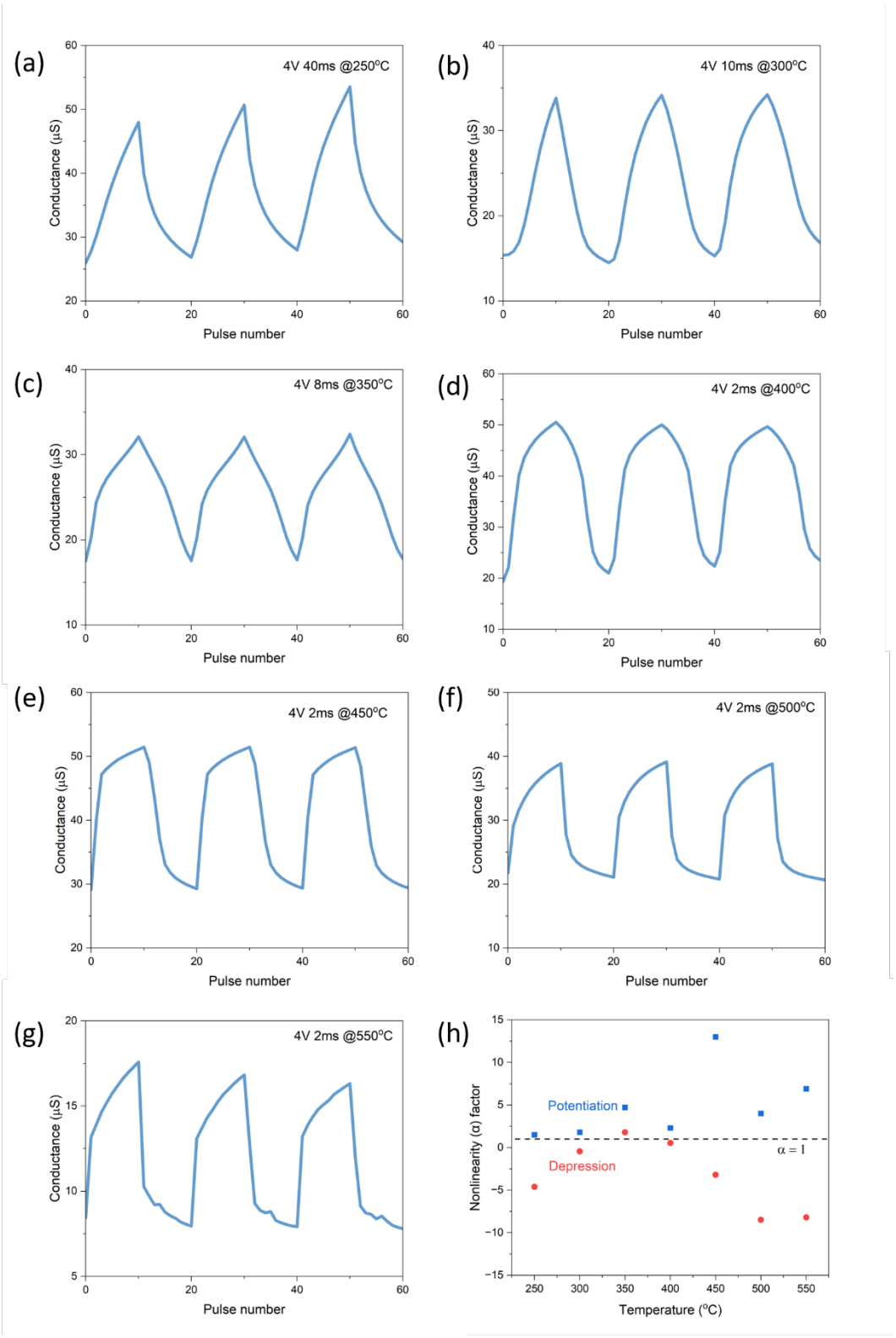


Figure 5.16: (a-g) Analog switching with 4V pulse across a broad temperature range, spanning from 250°C to 550°C. (h) Nonlinearity (α) factors for both potentiation and depression. When α is close to 1, the conductance modulation

approaches ideal linearity. The analog switching exhibited better linear behavior at temperatures ≤ 400°C compared to those at ≥ 450°C.

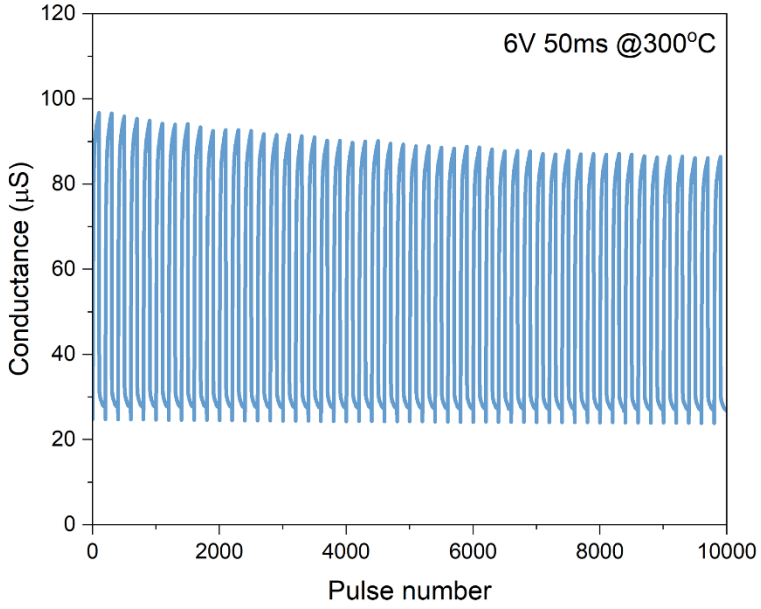


Figure 5.17: Endurance test of 10000 pulses at 300°C for analog switching with 100 multistate.

5.6 Conclusion

In this chapter, we demonstrated that phase separation in amorphous tantalum oxide is key to enabling nonvolatile phenomena in ECRAM. Our findings reveal that this phase separation stabilizes oxygen ion distribution, leading to improved retention and switching performance, particularly under high temperatures up to 600°C. Through a combination of experimental results and phase-field modeling, we established that TaO_X-based ECRAM offers both binary and analog switching capabilities with exceptional stability and endurance, making it a strong candidate for high-temperature nonvolatile memory applications. These insights provide a new approach for advancing analog computing and memory technologies in extreme environment

Chapter 6 Conclusion and Future Work

6.1 Summary

This thesis work focuses on understanding and advancing emerging nonvolatile resistive memory technology. The research begins with the observation of uphill diffusion in ReRAM, a phenomenon where ions move against the concentration gradient under certain conditions. This observation led to the unraveling of intrinsic phase separation in the amorphous oxide system used in ReRAM. By exploring the thermodynamic principles governing phase separation, the thesis provides a detailed analysis of how these processes affect the stability and performance of resistive memory devices.

Building on the foundational understanding of phase separation and ion dynamics in amorphous oxides, the research then applies these principles to enhance the retention performance of ECRAM. Retention performance, which refers to the ability of the memory device to maintain its data state over time without power, is crucial for the reliability of nonvolatile memory. By leveraging the thermodynamic insights gained from studying ReRAM, strategies were developed to control phase separation and ion distribution in ECRAM, thereby improving its retention characteristics.

Overall, this thesis provides a comprehensive study of the mechanisms driving phase separation and ion movement in resistive memory technologies and demonstrates how these insights can be used to optimize the performance of next-generation nonvolatile memory devices. The work not only contributes to the theoretical understanding of memory materials but also offers

practical approaches to enhancing the stability and reliability of ECRAM, paving the way for its integration into advanced computing systems and high-density memory applications.

6.1.1 Thermodynamics and Kinetics in ReRAM

We utilised a multimodal approach combining device measurements, scanning probe microscopy, depth profiling, *ab initio*, and continuum simulations. In conjunction, our results provide a consistent picture showing the strong consequence of phase separation on mass transport in TaOx. Our inclusion of compositional phase separation into oxygen transport models is a paradigm change for resistive memory and more broadly for defect-rich electronics. We thereby correct a longstanding and pervasive assumption of ideal solid solution used in previous physical models based on ideal Fickian diffusion. The Fickian diffusion equation $J = -D\,\nabla c$ is a special case of mass transport where the mobile chemical species form an ideal thermodynamic solution with the host (see Appendix B). Because most binary metal-oxygen phase diagrams show phase separation for temperatures <500ºC, the ideal solution assumption for $J = -D\,\nabla c$ is not fulfilled outside dilute limits in most crystalline metal oxides. Combined, our results show that ideal Fickian diffusion should not be assumed for most, if not all, filament-based VCM. Rather than assume ideal solution thermodynamics, it is important to modify the Gibbs energy to account for phase separation.

Additionally, our ability to measure sub-oxide tracer diffusion (Figure 4.3) and characterise composition phase separation (Figure 3.7 and 3.10) reconciles vast discrepancies regarding both the magnitude and direction of retention time in TaOx VCM. While phase separation into Ta-rich and O-rich domains have previously been observed in pioneering electron microscopy measurements of the filament[47,69], our work explains how phase separation affects mass transport and ultimately controls the ability of memristive devices to attain a core functionality, which is to

retain information over time. The composition phase separation mechanisms described in this work differ from the role of the decomposed SrO phase in $SrTiO_3$, which acts as a kinetic oxygen diffusion barrier[85]. We show that information retention in valence change memory has a thermodynamic origin–phase separation–and is not only a consequence of oxygen diffusion kinetics. While our experiments simulate oxygen, the computed chemical potential of Ta is also nonmonotonic with composition; therefore, we expect qualitatively similar diffusion characteristics if Ta is the mobile ion, as suggested in several recent experiments[86].

From a technological point of view, our results demonstrate that phase separation, even for metastable amorphous materials, may enable resistive switching devices with retention times unconstrained by diffusion times (Figure 3.17). This design rule is especially important for unconventional memristors such as those made from transition metal dichalcogenides[5] and organic materials[54] that typically have poor retention. Phase separation also provides an avenue to improve retention in non-filamentary interfacial memristors[87], which has more reliable switching but poorer retention.

Beyond resistive memory, our work has broad implications for future electronics enabled by defects and defect migration. For example, oxygen vacancy migration is directly linked to ferroelectricity in orthorhombic Hafnia[88]. While the dilute point defects in traditional covalent semiconductors generally follow ideal solution thermodynamics, our work shows that this assumption may not apply to newer classes of electronic and quantum materials with much higher point defect concentrations[89–91]. Accounting for nonideal interactions including compositional phase separation is critical, and ignoring such effects can lead to substantial errors like it did for resistive switching.

6.1.2 Thermodynamic Engineering for Nonvolatile ECRAM

Our study presents a non-volatile ECRAM device leveraging amorphous TaO_X, showcasing substantial stability in binary and analog operations even at temperatures as high as 600°C. By this metric, its high-temperature performance is substantially better than commercial floating-gate memory, valence-change resistive memory, and other forms of electrochemical random-access memory. Its temperature performance is comparable to that of recently-demonstrated nitride-based ferroelectric memory. However, our ECRAM uses lower voltages and the opportunity for analog mulitlevel states. Such a memory cell is deposited at room temperature and annealed at 400C, making it compatible with both CMOS and SiC technology.

Beyond performance, our TEM and phase-field model confirms that amorphous phase separation is responsible for the excellent retention of our nonvolatile ECRAM. This characterization and modeling results confirm that compositional phase separation can be used nonvolatile memory with extreme temperature stability. Moreover, the persistent coexistence of the Ta-rich and oxygen-rich regions provides additional evidence of phase separation in amorphous tantalum oxide. Due to the bulk dimensional switching region, our characterization of phase seaparation in ECRAM could also help understanding of filamentary valence-change memory made using tantalum oxide and other materials, where the nanosized filaments are much more difficult to locate.

6.2 Future Work

6.2.1 Downscaling ECRAM

With electron beam lithography, atomic layer deposition, sputter deposition, and other nanofabrication techniques in the Lurie Nanofabrication Facility, the sub-micron ECRAM devices can be developed. These techniques allow for precise control over the device dimensions and material properties, which are crucial for fabricating high-performance nanoscale devices.

Electron beam lithography provides the capability to pattern features at the sub-micron level, while atomic layer deposition and sputter deposition ensure uniform and high-quality thin films essential for the active layers of ECRAM devices.

By systematically downscaling the device dimensions, I aim to investigate how these changes affect critical device properties, specifically focusing on retention and switching times. Retention refers to the ability of the ECRAM to maintain its resistance state over time without power, which is essential for reliable non-volatile memory applications. Switching time, on the other hand, is the speed at which the device can change between resistance states, influencing the overall performance and energy efficiency of the memory. Understanding the impact of size reduction on these parameters will provide valuable insights into the limits and potentials of ECRAM technology.

This research will contribute to the broader goal of optimizing ECRAM technology for high-density memory applications and improving its integration into advanced computing systems. As device dimensions continue to shrink in the pursuit of higher memory densities and faster computing speeds, it is crucial to understand the scalability of ECRAM devices and their performance at the nanoscale. Through this work, I will provide important data and analysis that can inform the design and development of next-generation memory and neuromorphic computing architectures, ensuring that ECRAM can meet the demands of future technological advancements.

6.2.2 Fabrication of ECRAM Arrays for High-temperature Applications

One of the primary avenues for future work is the fabrication and characterization of ECRAM arrays. Developing an array of ECRAM devices will be crucial for assessing their scalability and integration potential in larger memory systems. In fabricating ECRAM arrays, it will be important to address challenges related to device uniformity, cross-talk between cells, and

integration with existing semiconductor technologies. Systematic studies will be conducted to optimize the fabrication process, ensuring high yield and reliability of the devices. Characterization of these arrays will focus on evaluating their electrical performance, retention, switching times, and endurance. Additionally, exploring the impact of array architecture on overall device performance and developing efficient read/write schemes will be critical steps toward practical applications of ECRAM in advanced memory systems.

The successful fabrication and testing of high-temperature ECRAM arrays will open new avenues for their integration into advanced computing and memory systems. Potential applications include high-temperature data logging, robust memory systems for aerospace and automotive electronics, and reliable storage solutions for industrial automation. Further, these advancements could pave the way for ECRAM's use in harsh environments, contributing to the development of resilient and efficient electronic systems.

Appendices

Appendix A: Thermodynamic Considerations of Amorphous Materials

All the amorphous tantalum oxide films used in this work are metastable and have higher formation energy than the stable crystalline states. However, even though such materials are metastable, we can still apply thermodynamic principles to understand and describe mass transport. In this section, we aim to answer some frequently asked questions that we received when discussing these ideas in the community.

1) Why can we define chemical potential and Gibbs free energy for metastable compounds?

The chemical potential and Gibbs free energy are physical variables. Just as metastable materials have temperature, pressure, and volume, they also have chemical potential and Gibbs free energy.

2) If tantalum oxide material is in a metastable amorphous state, why does it obey the same mass transport laws as the equilibrium crystalline material?

In tantalum oxide, the crystalline state cannot be accessed at temperatures below 600ºC. Therefore, all tantalum oxide films in this work will be amorphous. However, even though there exists a crystalline state with lower energy, an individual atom does not have this information. Therefore, its kinetics will be dictated by the local forces and energies. During retention under no applied voltages, the primary driver of transport is the chemical potential.

3) How can an amorphous material have different phases?

The definition of a phase is a material that is homogeneous in all physical properties. Some examples of physical properties include crystal symmetry, chemical composition, and magnetic phase. Therefore, while amorphous solids lack long-range crystal symmetry, they can still have different phases if the chemical composition is different. In this work, we study composition phase separation into oxygen-deficient and oxygen-rich materials. Phase separation is not limited to differences in crystal symmetry.

4) What is the definition of amorphous phase separation?

For this work, phase separation is defined as when two phases of the material can be distinguished, and is not progressing towards a uniform, homogeneous material even when in contact. Because the crystalline phase is not accessible at our temperatures, the amorphous phases can undergo phase separation when the convex hull is represented by a common tangent in the Gibbs Free Energy. Experimentally, phase separation arises when two materials with distinct properties are observed. For crystalline materials, this is usually most easily observed with diffraction. Because amorphous materials do not have long-range order, we instead aim to identify distinct chemical compositions, and show that they will remain distinct even after long periods of time.

Phase diagrams can be generated for amorphous and other metastable materials. One example is the ternary phase diagram of amorphous borosilicate glass (SiO_2, B_2O_3, Na_2O). Another example is that of the radioactive U-235: although it is technically metastable with a half-life ~10^9 years, it will form the same binary phase diagram with oxygen as U-238 does.

5) What is "flux equilibrium"?

We use the term "flux equilibrium" to describe a situation where there is no net mass flux ($J=0$), but the system is not in true equilibrium because it resides in a metastable state. In our case,

this occurs when the net flux is 0 because there is no gradient in the chemical potential ($\nabla\mu = 0$), but the material is in a higher-energy, metastable amorphous state.

6) Why does the amorphous Ta-O phase separate?

Ta-O phase separates because we experimentally observe two distinct compositions that are not converging towards a single homogeneous material. The thermodynamic reason is that a common tangent can be constructed in the composition–energy diagram. Therefore, for a fixed number of tantalum and oxygen atoms, the bonding energy from a combination of oxygen-deficient and oxygen-rich compounds is more negative (favourable) compared to that of a single homogeneous compound. This makes phase separation the more energetically favourable state for the compositions within the miscibility gap.

Appendix B: Thermodynamic Origins of J =-D∇c

In this section, we show how the generalised transport equation lead to the common approximation $J = -D\nabla c$ only under ideal thermodynamic solutions.

The generalised transport equation is given as

$$J = -D/k_B T\ c\ \nabla\mu \tag{5}$$

where J is the flux, D the diffusivity k_B the Boltzmann constant, T the temperature, c the concentration, and μ the chemical potential.

In an ideal solution (or for nonideal solutions under a dilute approximation), the chemical potential only accounts for the entropy, and is given by

$$\mu = k_B T\ ln\ c/c_0 = k_B T\ (ln\ c - ln\ c_0) \tag{6}$$

where c_0 is the number of sites. By substituting this chemical potential into the generalised transport equation alongside the chain rule, we can derive the common form of Fick's first law.

$$\begin{aligned} J &= -\frac{D}{k_B T}\ c\ \nabla(k_B T\ ln\ c - k_B T\ ln\ c_0) \\ &= -\frac{D}{k_B T} k_B T\ c\ \nabla(ln\ c) \\ &= -D\ c\ \frac{1}{c}\nabla c = -D\nabla c \end{aligned} \tag{7}$$

As shown in this derivation, the precondition for Fick's first law ($J = -D\nabla c$) is that the chemical potential only has an entropic component (equation 6). This condition is not applicable for most metal-oxygen compounds under nondilute concentrations.

References

(1) Chen, A. A Review of Emerging Non-Volatile Memory (NVM) Technologies and Applications. *Solid-State Electron.* **2016**, *125*, 25–38. https://doi.org/10.1016/j.sse.2016.07.006.

(2) Wang, Z.; Wu, H.; Burr, G. W.; Hwang, C. S.; Wang, K. L.; Xia, Q.; Yang, J. J. Resistive Switching Materials for Information Processing. *Nat. Rev. Mater.* **2020**, *5* (3), 173–195. https://doi.org/10.1038/s41578-019-0159-3.

(3) Waser, R.; Dittmann, R.; Staikov, G.; Szot, K. Redox-Based Resistive Switching Memories – Nanoionic Mechanisms, Prospects, and Challenges. *Adv. Mater.* **2009**, *21* (25–26), 2632–2663. https://doi.org/10.1002/adma.200900375.

(4) Yang, J. J.; Strukov, D. B.; Stewart, D. R. Memristive Devices for Computing. *Nat. Nanotechnol.* **2013**, *8* (1), 13–24. https://doi.org/10.1038/nnano.2012.240.

(5) Lee, M.-J.; Lee, C. B.; Lee, D.; Lee, S. R.; Chang, M.; Hur, J. H.; Kim, Y.-B.; Kim, C.-J.; Seo, D. H.; Seo, S.; Chung, U.-I.; Yoo, I.-K.; Kim, K. A Fast, High-Endurance and Scalable Non-Volatile Memory Device Made from Asymmetric Ta2O5−x/TaO2−x Bilayer Structures. *Nat. Mater.* **2011**, *10* (8), 625–630. https://doi.org/10.1038/nmat3070.

(6) Li, H. K.; Chen, T. P.; Hu, S. G.; Liu, P.; Liu, Y.; Lee, P. S.; Wang, X. P.; Li, H. Y.; Lo, G. Q. Study of Multilevel High-Resistance States in HfOx-Based Resistive Switching Random Access Memory by Impedance Spectroscopy. *IEEE Trans. Electron Devices* **2015**, *62* (8), 2684–2688. https://doi.org/10.1109/TED.2015.2445339.

(7) Azzaz, M.; Vianello, E.; Sklenard, B.; Blaise, P.; Roule, A.; Sabbione, C.; Bernasconi, S.; Charpin, C.; Cagli, C.; Jalaguier, E.; Jeannot, S.; Denorme, S.; Candelier, P.; Yu, M.; Nistor, L.; Fenouillet-Beranger, C.; Perniola, L. Endurance/Retention Trade Off in HfOx and TaOx Based RRAM. In *2016 IEEE 8th International Memory Workshop (IMW)*; 2016; pp 1–4. https://doi.org/10.1109/IMW.2016.7495268.

(8) Kim, S.; Todorov, T.; Onen, M.; Gokmen, T.; Bishop, D.; Solomon, P.; Lee, K.-T.; Copel, M.; Farmer, D. B.; Ott, J. A.; Ando, T.; Miyazoe, H.; Narayanan, V.; Rozen, J. Metal-Oxide Based, CMOS-Compatible ECRAM for Deep Learning Accelerator. In *2019 IEEE International Electron Devices Meeting (IEDM)*; 2019; p 35.7.1-35.7.4. https://doi.org/10.1109/IEDM19573.2019.8993463.

(9) Li, Y.; Fuller, E. J.; Sugar, J. D.; Yoo, S.; Ashby, D. S.; Bennett, C. H.; Horton, R. D.; Bartsch, M. S.; Marinella, M. J.; Lu, W. D.; Talin, A. A. Filament-Free Bulk Resistive Memory Enables Deterministic Analogue Switching. *Adv. Mater.* **2020**, *32* (45), 2003984. https://doi.org/10.1002/adma.202003984.

(10) Huang, M.; Schwacke, M.; Onen, M.; del Alamo, J.; Li, J.; Yildiz, B. Electrochemical Ionic Synapses: Progress and Perspectives. *Adv. Mater.* **2023**, *35* (37), 2205169. https://doi.org/10.1002/adma.202205169.

(11) Talin, A. A.; Li, Y.; Robinson, D. A.; Fuller, E. J.; Kumar, S. ECRAM Materials, Devices, Circuits and Architectures: A Perspective. *Adv. Mater.* **2023**, *35* (37), 2204771. https://doi.org/10.1002/adma.202204771.

(12) Onen, M.; Emond, N.; Wang, B.; Zhang, D.; Ross, F. M.; Li, J.; Yildiz, B.; del Alamo, J. A. Nanosecond Protonic Programmable Resistors for Analog Deep Learning. *Science* **2022**, *377* (6605), 539–543. https://doi.org/10.1126/science.abp8064.

(13) Fuller, E. J.; Gabaly, F. E.; Léonard, F.; Agarwal, S.; Plimpton, S. J.; Jacobs-Gedrim, R. B.; James, C. D.; Marinella, M. J.; Talin, A. A. Li-Ion Synaptic Transistor for Low Power Analog Computing. *Adv. Mater.* **2017**, *29* (4), 1604310. https://doi.org/10.1002/adma.201604310.

(14) Zidan, M. A.; Strachan, J. P.; Lu, W. D. The Future of Electronics Based on Memristive Systems. *Nat. Electron.* **2018**, *1* (1), 22–29. https://doi.org/10.1038/s41928-017-0006-8.

(15) Jeong, D. S.; Kim, K. M.; Kim, S.; Choi, B. J.; Hwang, C. S. Memristors for Energy-Efficient New Computing Paradigms. *Adv. Electron. Mater.* **2016**, *2* (9), 1600090. https://doi.org/10.1002/aelm.201600090.

(16) Sebastian, A.; Le Gallo, M.; Khaddam-Aljameh, R.; Eleftheriou, E. Memory Devices and Applications for In-Memory Computing. *Nat. Nanotechnol.* **2020**, *15* (7), 529–544. https://doi.org/10.1038/s41565-020-0655-z.

(17) Sangwan, V. K.; Hersam, M. C. Neuromorphic Nanoelectronic Materials. *Nat. Nanotechnol.* **2020**, *15* (7), 517–528. https://doi.org/10.1038/s41565-020-0647-z.

(18) Suga, H.; Suzuki, H.; Shinomura, Y.; Kashiwabara, S.; Tsukagoshi, K.; Shimizu, T.; Naitoh, Y. Highly Stable, Extremely High-Temperature, Nonvolatile Memory Based on Resistance Switching in Polycrystalline Pt Nanogaps. *Sci. Rep.* **2016**, *6* (1), 34961. https://doi.org/10.1038/srep34961.

(19) Chua, L. Memristor-The Missing Circuit Element. *IEEE Trans. Circuit Theory* **1971**, *18* (5), 507–519. https://doi.org/10.1109/TCT.1971.1083337.

(20) Strukov, D. B.; Snider, G. S.; Stewart, D. R.; Williams, R. S. The Missing Memristor Found. *Nature* **2008**, *453* (7191), 80–83. https://doi.org/10.1038/nature06932.

(21) Jo, S. H.; Chang, T.; Ebong, I.; Bhadviya, B. B.; Mazumder, P.; Lu, W. Nanoscale Memristor Device as Synapse in Neuromorphic Systems. *Nano Lett.* **2010**, *10* (4), 1297–1301. https://doi.org/10.1021/nl904092h.

(22) Du, C.; Ma, W.; Chang, T.; Sheridan, P.; Lu, W. D. Biorealistic Implementation of Synaptic Functions with Oxide Memristors through Internal Ionic Dynamics. *Adv. Funct. Mater.* **2015**, *25* (27), 4290–4299. https://doi.org/10.1002/adfm.201501427.

(23) Yang, Y.; Chen, B.; Lu, W. D. Memristive Physically Evolving Networks Enabling the Emulation of Heterosynaptic Plasticity. *Adv. Mater.* **2015**, *27* (47), 7720–7727. https://doi.org/10.1002/adma.201503202.

(24) Neudeck, P. G.; Okojie, R. S.; Chen, L.-Y. High-Temperature Electronics - a Role for Wide Bandgap Semiconductors? *Proc. IEEE* **2002**, *90* (6), 1065–1076. https://doi.org/10.1109/JPROC.2002.1021571.

(25) Cressler, J. D.; Mantooth, H. A. *Extreme Environment Electronics*; CRC Press, 2017.

(26) Neudeck, P. G.; Spry, D. J.; Chen, L.; Prokop, N. F.; Krasowski, M. J. Demonstration of 4H-SiC Digital Integrated Circuits Above 800 °C. *IEEE Electron Device Lett.* **2017**, *38* (8), 1082–1085. https://doi.org/10.1109/LED.2017.2719280.

(27) Yuan, M.; Xie, Q.; Niroula, J.; Isamotu, M. F.; Rajput, N. S.; Chowdhury, N.; Palacios, T. High Temperature Robustness of Enhancement-Mode p-GaN-Gated AlGaN/GaN HEMT Technology. In *2022 IEEE 9th Workshop on Wide Bandgap Power Devices & Applications (WiPDA)*; 2022; pp 40–44. https://doi.org/10.1109/WiPDA56483.2022.9955304.

(28) Jo, E.; Kang, Y.; Sim, S.; Lee, H.; Kim, J. High-Temperature-Operable Electromechanical Computing Units Enabled by Aligned Carbon Nanotube Arrays. *ACS Nano* **2023**, *17* (14), 13310–13318. https://doi.org/10.1021/acsnano.3c01304.

(29) Drury, D.; Yazawa, K.; Zakutayev, A.; Hanrahan, B.; Brennecka, G. High-Temperature Ferroelectric Behavior of Al0.7Sc0.3N. *Micromachines* **2022**, *13* (6), 887. https://doi.org/10.3390/mi13060887.

(30) Dong, R.-Y.; Granick, S. Reincarnations of the Phase Separation Problem. *Nat. Commun.* **2021**, *12* (1), 911. https://doi.org/10.1038/s41467-020-20360-4.

(31) Park, S.-O.; Jeong, H.; Park, J.; Bae, J.; Choi, S. Experimental Demonstration of Highly Reliable Dynamic Memristor for Artificial Neuron and Neuromorphic Computing. *Nat. Commun.* **2022**, *13* (1), 2888. https://doi.org/10.1038/s41467-022-30539-6.

(32) Kwon, D.-H.; Kim, K. M.; Jang, J. H.; Jeon, J. M.; Lee, M. H.; Kim, G. H.; Li, X.-S.; Park, G.-S.; Lee, B.; Han, S.; Kim, M.; Hwang, C. S. Atomic Structure of Conducting Nanofilaments in TiO2 Resistive Switching Memory. *Nat. Nanotechnol.* **2010**, *5* (2), 148–153. https://doi.org/10.1038/nnano.2009.456.

(33) Chang, T.; Jo, S.-H.; Lu, W. Short-Term Memory to Long-Term Memory Transition in a Nanoscale Memristor. *ACS Nano* **2011**, *5* (9), 7669–7676. https://doi.org/10.1021/nn202983n.

(34) Yang, R.; Terabe, K.; Liu, G.; Tsuruoka, T.; Hasegawa, T.; Gimzewski, J. K.; Aono, M. On-Demand Nanodevice with Electrical and Neuromorphic Multifunction Realized by Local Ion Migration. *ACS Nano* **2012**, *6* (11), 9515–9521. https://doi.org/10.1021/nn302510e.

(35) Lin, Y.; Meng, F.; Zeng, T.; Zhang, Q.; Wang, Z.; Cheng, Y.; Zhao, X.; Gu, L.; Xu, H.; Liu, Y. Direct Observation of Oxygen Ion Dynamics in a WO3-x Based Second-Order Memristor with Dendritic Integration Functions. *Adv. Funct. Mater. n/a* (n/a), 2302787. https://doi.org/10.1002/adfm.202302787.

(36) Chen, Y. Y.; Komura, M.; Degraeve, R.; Govoreanu, B.; Goux, L.; Fantini, A.; Raghavan, N.; Clima, S.; Zhang, L.; Belmonte, A.; Redolfi, A.; Kar, G. S.; Groeseneken, G.;

Wouters, D. J.; Jurczak, M. Improvement of Data Retention in HfO2/Hf 1T1R RRAM Cell under Low Operating Current. In *2013 IEEE International Electron Devices Meeting*; 2013; p 10.1.1-10.1.4. https://doi.org/10.1109/IEDM.2013.6724598.

(37) Chen, C. Y.; Fantini, A.; Goux, L.; Degraeve, R.; Clima, S.; Redolfi, A.; Groeseneken, G.; Jurczak, M. Programming-Conditions Solutions towards Suppression of Retention Tails of Scaled Oxide-Based RRAM. In *2015 IEEE International Electron Devices Meeting (IEDM)*; 2015; p 10.6.1-10.6.4. https://doi.org/10.1109/IEDM.2015.7409671.

(38) Wei, Z.; Kanzawa, Y.; Arita, K.; Katoh, Y.; Kawai, K.; Muraoka, S.; Mitani, S.; Fujii, S.; Katayama, K.; Iijima, M.; Mikawa, T.; Ninomiya, T.; Miyanaga, R.; Kawashima, Y.; Tsuji, K.; Himeno, A.; Okada, T.; Azuma, R.; Shimakawa, K.; Sugaya, H.; Takagi, T.; Yasuhara, R.; Horiba, K.; Kumigashira, H.; Oshima, M. Highly Reliable TaOx ReRAM and Direct Evidence of Redox Reaction Mechanism. In *2008 IEEE International Electron Devices Meeting*; 2008; pp 1–4. https://doi.org/10.1109/IEDM.2008.4796676.

(39) Wei, Z.; Takagi, T.; Kanzawa, Y.; Katoh, Y.; Ninomiya, T.; Kawai, K.; Muraoka, S.; Mitani, S.; Katayama, K.; Fujii, S.; Miyanaga, R.; Kawashima, Y.; Mikawa, T.; Shimakawa, K.; Aono, K. Demonstration of High-Density ReRAM Ensuring 10-Year Retention at 85°C Based on a Newly Developed Reliability Model. In *2011 International Electron Devices Meeting*; 2011; p 31.4.1-31.4.4. https://doi.org/10.1109/IEDM.2011.6131650.

(40) Wriedt, H. A. The O-W (Oxygen-Tungsten) System. *Bull. Alloy Phase Diagr.* **1989**, *10* (4), 368–384. https://doi.org/10.1007/BF02877593.

(41) Tang, J.; Bishop, D.; Kim, S.; Copel, M.; Gokmen, T.; Todorov, T.; Shin, S.; Lee, K.-T.; Solomon, P.; Chan, K.; Haensch, W.; Rozen, J. ECRAM as Scalable Synaptic Cell for High-

Speed, Low-Power Neuromorphic Computing. In *2018 IEEE International Electron Devices Meeting (IEDM)*; 2018; p 13.1.1-13.1.4. https://doi.org/10.1109/IEDM.2018.8614551.

(42) Yao, X.; Klyukin, K.; Lu, W.; Onen, M.; Ryu, S.; Kim, D.; Emond, N.; Waluyo, I.; Hunt, A.; del Alamo, J. A.; Li, J.; Yildiz, B. Protonic Solid-State Electrochemical Synapse for Physical Neural Networks. *Nat. Commun.* **2020**, *11* (1), 3134. https://doi.org/10.1038/s41467-020-16866-6.

(43) Kim, D. S.; Watkins, V. J.; Cline, L. A.; Li, J.; Sun, K.; Sugar, J. D.; Fuller, E. J.; Talin, A. A.; Li, Y. Nonvolatile Electrochemical Random-Access Memory under Short Circuit. *Adv. Electron. Mater.* **2023**, *9* (1), 2200958. https://doi.org/10.1002/aelm.202200958.

(44) Okamoto, H. O-Ti (Oxygen-Titanium). *J. Phase Equilibria Diffus.* **2011**, *32* (5), 473–474. https://doi.org/10.1007/s11669-011-9935-5.

(45) Garg, S. P.; Krishnamurthy, N.; Awasthi, A.; Venkatraman, M. The O-Ta (Oxygen-Tantalum) System. *J. Phase Equilibria* **1996**, *17* (1), 63–77. https://doi.org/10.1007/BF02648373.

(46) Shin, D.; Arróyave, R.; Liu, Z.-K. Thermodynamic Modeling of the Hf–Si–O System. *Calphad* **2006**, *30* (4), 375–386. https://doi.org/10.1016/j.calphad.2006.08.006.

(47) Ma, Y.; Li, D.; Herzing, A. A.; Cullen, D. A.; Sneed, B. T.; More, K. L.; Nuhfer, N. T.; Bain, J. A.; Skowronski, M. Formation of the Conducting Filament in TaOx-Resistive Switching Devices by Thermal-Gradient-Induced Cation Accumulation. *ACS Appl. Mater. Interfaces* **2018**, *10* (27), 23187–23197. https://doi.org/10.1021/acsami.8b03726.

(48) Cahn, J. W.; Hilliard, J. E. Free Energy of a Nonuniform System. I. Interfacial Free Energy. *J. Chem. Phys.* **1958**, *28* (2), 258–267. https://doi.org/10.1063/1.1744102.

(49) Cahn, J. W. On Spinodal Decomposition. *Acta Metall.* **1961**, *9* (9), 795–801. https://doi.org/10.1016/0001-6160(61)90182-1.

(50) Lee, S. H.; Moon, J.; Jeong, Y.; Lee, J.; Li, X.; Wu, H.; Lu, W. D. Quantitative, Dynamic TaO_x Memristor/Resistive Random Access Memory Model. *ACS Appl. Electron. Mater.* **2020**, *2* (3), 701–709. https://doi.org/10.1021/acsaelm.9b00792.

(51) Li, J.; Appachar, A.; Peczonczyk, S. L.; Harrison, E. T.; Ievlev, A. V.; Hood, R.; Shin, D.; Yoo, S.; Roest, B.; Sun, K.; Beckmann, K.; Popova, O.; Chiang, T.; Wahby, W. S.; Jacobs-Godrim, R. B.; Marinella, M. J.; Maksymovych, P.; Heron, J. T.; Cady, N.; Lu, W. D.; Kumar, S.; Talin, A. A.; Sun, W.; Li, Y. Thermodynamic Origin of Nonvolatility in Resistive Memory. *Matter* **2024**, *0* (0). https://doi.org/10.1016/j.matt.2024.07.018.

(52) Yang, Y.; Zhang, X.; Qin, L.; Zeng, Q.; Qiu, X.; Huang, R. Probing Nanoscale Oxygen Ion Motion in Memristive Systems. *Nat. Commun.* **2017**, *8* (1), 15173. https://doi.org/10.1038/ncomms15173.

(53) Choi, S.; Lee, J.; Kim, S.; Lu, W. D. Retention Failure Analysis of Metal-Oxide Based Resistive Memory. *Appl. Phys. Lett.* **2014**, *105* (11), 113510. https://doi.org/10.1063/1.4896154.

(54) Park, J.; Choi, J.; Kim, G.; Kim, G.; Kim, G. S.; Song, H.; Kim, Y. S.; Lee, Y.; Rhee, H.; Lee, H. M.; Hwang, C. S.; Kim, K. M. Modified Dynamic Physical Model of Valence Change Mechanism Memristors. *ACS Appl. Mater. Interfaces* **2022**, *14* (31), 35949–35958. https://doi.org/10.1021/acsami.2c10944.

(55) Chen, Y. Y.; Goux, L.; Clima, S.; Govoreanu, B.; Degraeve, R.; Kar, G. S.; Fantini, A.; Groeseneken, G.; Wouters, D. J.; Jurczak, M. Endurance/Retention Trade-off on $\hboxHfO_2/\hboxMetal$ Cap 1T1R Bipolar RRAM. *IEEE Trans. Electron Devices* **2013**, *60* (3), 1114–1121. https://doi.org/10.1109/TED.2013.2241064.

(56) La Torre, C. Physics-Based Compact Modeling of Valence-Change-Based Resistive Switching Devices. Doctoral dissertation, RWTH Aachen University, 2019.

(57) Larentis, S.; Cagli, C.; Nardi, F.; Ielmini, D. Filament Diffusion Model for Simulating Reset and Retention Processes in RRAM. *Microelectron. Eng.* **2011**, *88* (7), 1119–1123. https://doi.org/10.1016/j.mee.2011.03.055.

(58) Ueki, M.; Hayashi, Y.; Furutake, N.; Masuzaki, K.; Tanabe, A.; Narihiro, M.; Sunamura, H.; Uejima, K.; Mitsuiki, A.; Takeda, K.; Hase, T. Stabilizing Schemes for the Minority Failure Bits in Ta2O5-Based ReRAM Macro. *IEEE Trans. Electron Devices* **2017**, *64* (2), 419–426. https://doi.org/10.1109/TED.2016.2639283.

(59) Goux, L.; Fantini, A.; Chen, Y. Y.; Redolfi, A.; Degraeve, R.; Jurczak, M. Evidences of Electrode-Controlled Retention Properties in Ta2O5-Based Resistive-Switching Memory Cells. *ECS Solid State Lett.* **2014**, *3* (11), Q79. https://doi.org/10.1149/2.0011412ssl.

(60) Jiang, H.; Han, L.; Lin, P.; Wang, Z.; Jang, M. H.; Wu, Q.; Barnell, M.; Yang, J. J.; Xin, H. L.; Xia, Q. Sub-10 Nm Ta Channel Responsible for Superior Performance of a HfO2 Memristor. *Sci. Rep.* **2016**, *6* (1), 1–8. https://doi.org/10.1038/srep28525.

(61) Funck, C.; Menzel, S. Comprehensive Model of Electron Conduction in Oxide-Based Memristive Devices. *ACS Appl. Electron. Mater.* **2021**, *3* (9), 3674–3692. https://doi.org/10.1021/acsaelm.1c00398.

(62) Kim, W.; Wouters, D. J.; Menzel, S.; Rodenbücher, C.; Waser, R.; Rana, V. Lowering Forming Voltage and Forming-Free Behavior of Ta2O5 ReRAM Devices. In *2016 46th European Solid-State Device Research Conference (ESSDERC)*; 2016; pp 164–167. https://doi.org/10.1109/ESSDERC.2016.7599612.

(63) Park, G.-S.; Kim, Y. B.; Park, S. Y.; Li, X. S.; Heo, S.; Lee, M.-J.; Chang, M.; Kwon, J. H.; Kim, M.; Chung, U.-I.; Dittmann, R.; Waser, R.; Kim, K. In Situ Observation of Filamentary Conducting Channels in an Asymmetric Ta2O5−x/TaO2−x Bilayer Structure. *Nat. Commun.* **2013**, *4* (1), 2382. https://doi.org/10.1038/ncomms3382.

(64) Ezhilvalavan, S.; Tseng, T. Y. Preparation and Properties of Tantalum Pentoxide (Ta2O5) Thin Films for Ultra Large Scale Integrated Circuits (ULSIs) Application – A Review. *J. Mater. Sci. Mater. Electron.* **1999**, *10* (1), 9–31. https://doi.org/10.1023/A:1008970922635.

(65) Miao, F.; Strachan, J. P.; Yang, J. J.; Zhang, M.-X.; Goldfarb, I.; Torrezan, A. C.; Eschbach, P.; Kelley, R. D.; Medeiros-Ribeiro, G.; Williams, R. S. Anatomy of a Nanoscale Conduction Channel Reveals the Mechanism of a High-Performance Memristor. *Adv. Mater.* **2011**, *23* (47), 5633–5640. https://doi.org/10.1002/adma.201103379.

(66) Yang, J. J.; Zhang, M.-X.; Strachan, J. P.; Miao, F.; Pickett, M. D.; Kelley, R. D.; Medeiros-Ribeiro, G.; Williams, R. S. High Switching Endurance in TaOx Memristive Devices. *Appl. Phys. Lett.* **2010**, *97* (23), 232102. https://doi.org/10.1063/1.3524521.

(67) Pedersen, C. S.; Chang, J. H.; Li, Y.; Pryds, N.; Garcia Lastra, J. M. Phase Separation in Amorphous Tantalum Oxide from First Principles. *APL Mater.* **2020**, *8* (7), 071108. https://doi.org/10.1063/5.0011390.

(68) Heisig, T.; Lange, K.; Gutsche, A.; Goß, K. T.; Hambsch, S.; Locatelli, A.; Menteş, T. O.; Genuzio, F.; Menzel, S.; Dittmann, R. Chemical Structure of Conductive Filaments in Tantalum Oxide Memristive Devices and Its Implications for the Formation Mechanism. *Adv. Electron. Mater.* **2022**, *n/a* (n/a), 2100936. https://doi.org/10.1002/aelm.202100936.

(69) Ma, Y.; Goodwill, J. M.; Li, D.; Cullen, D. A.; Poplawsky, J. D.; More, K. L.; Bain, J. A.; Skowronski, M. Stable Metallic Enrichment in Conductive Filaments in TaOx-Based

Resistive Switches Arising from Competing Diffusive Fluxes. *Adv. Electron. Mater.* **2019**, *5* (7), 1800954. https://doi.org/10.1002/aelm.201800954.

(70) Fang, Z.; Yu, H. Y.; Liu, W. J.; Wang, Z. R.; Tran, X. A.; Gao, B.; Kang, J. F. Temperature Instability of Resistive Switching on \hboxHfO_x-Based RRAM Devices. *IEEE Electron Device Lett.* **2010**, *31* (5), 476–478. https://doi.org/10.1109/LED.2010.2041893.

(71) Kim, M.; Rehman, M. A.; Lee, D.; Wang, Y.; Lim, D.-H.; Khan, M. F.; Choi, H.; Shao, Q. Y.; Suh, J.; Lee, H.-S.; Park, H.-H. Filamentary and Interface-Type Memristors Based on Tantalum Oxide for Energy-Efficient Neuromorphic Hardware. *ACS Appl. Mater. Interfaces* **2022**, *14* (39), 44561–44571. https://doi.org/10.1021/acsami.2c12296.

(72) Kim, S.; Choi, S.; Lu, W. Comprehensive Physical Model of Dynamic Resistive Switching in an Oxide Memristor. *ACS Nano* **2014**, *8* (3), 2369–2376. https://doi.org/10.1021/nn405827t.

(73) Skowronski, M. Material Instabilities in the TaOx-Based Resistive Switching Devices (Invited). In *2023 IEEE International Reliability Physics Symposium (IRPS)*; 2023; pp 1–5. https://doi.org/10.1109/IRPS48203.2023.10117796.

(74) Simmons, J. G. Generalized Formula for the Electric Tunnel Effect between Similar Electrodes Separated by a Thin Insulating Film. *J. Appl. Phys.* **1963**, *34* (6), 1793–1803. https://doi.org/10.1063/1.1702682.

(75) Zhao, M.; Wu, H.; Gao, B.; Zhang, Q.; Wu, W.; Wang, S.; Xi, Y.; Wu, D.; Deng, N.; Yu, S.; Chen, H.-Y.; Qian, H. Investigation of Statistical Retention of Filamentary Analog RRAM for Neuromophic Computing. In *2017 IEEE International Electron Devices Meeting (IEDM)*; 2017; p 39.4.1-39.4.4. https://doi.org/10.1109/IEDM.2017.8268522.

(76) Nakamura, R.; Toda, T.; Tsukui, S.; Tane, M.; Ishimaru, M.; Suzuki, T.; Nakajima, H. Diffusion of Oxygen in Amorphous Al2O3, Ta2O5, and Nb2O5. *J. Appl. Phys.* **2014**, *116* (3), 033504. https://doi.org/10.1063/1.4889800.

(77) Lee, J.; Schell, W.; Zhu, X.; Kioupakis, E.; Lu, W. D. Charge Transition of Oxygen Vacancies during Resistive Switching in Oxide-Based RRAM. *ACS Appl. Mater. Interfaces* **2019**, *11* (12), 11579–11586. https://doi.org/10.1021/acsami.8b18386.

(78) Traoré, B.; Blaise, P.; Vianello, E.; Grampeix, H.; Jeannot, S.; Perniola, L.; De Salvo, B.; Nishi, Y. On the Origin of Low-Resistance State Retention Failure in HfO2-Based RRAM and Impact of Doping/Alloying. *IEEE Trans. Electron Devices* **2015**, *62* (12), 4029–4036. https://doi.org/10.1109/TED.2015.2490545.

(79) Choi, S.; Shin, J. H.; Lee, J.; Sheridan, P.; Lu, W. D. Experimental Demonstration of Feature Extraction and Dimensionality Reduction Using Memristor Networks. *Nano Lett.* **2017**, *17* (5), 3113–3118. https://doi.org/10.1021/acs.nanolett.7b00552.

(80) Schie, M.; Marchewka, A.; Müller, T.; Souza, R. A. D.; Waser, R. Molecular Dynamics Simulations of Oxygen Vacancy Diffusion in SrTiO3. *J. Phys. Condens. Matter* **2012**, *24* (48), 485002. https://doi.org/10.1088/0953-8984/24/48/485002.

(81) van de Burgt, Y.; Lubberman, E.; Fuller, E. J.; Keene, S. T.; Faria, G. C.; Agarwal, S.; Marinella, M. J.; Alec Talin, A.; Salleo, A. A Non-Volatile Organic Electrochemical Device as a Low-Voltage Artificial Synapse for Neuromorphic Computing. *Nat. Mater.* **2017**, *16* (4), 414–418. https://doi.org/10.1038/nmat4856.

(82) Li, J.; Li, Y.; Sun, W.; Appachar, A.; Lu, W.; Alec Talin, A. Thermodynamic Origin of Nonvolatility in Resistive Switching. **2022**. https://doi.org/10.21203/rs.3.rs-2365752/v1.

(83) Pradhan, D. K.; Moore, D. C.; Kim, G.; He, Y.; Musavigharavi, P.; Kim, K.-H.; Sharma, N.; Han, Z.; Du, X.; Puli, V. S.; Stach, E. A.; Kennedy, W. J.; Glavin, N. R.; Olsson III, R. H.; Jariwala, D. Scalable and Stable Ferroelectric Non-Volatile Memory at > 500 $^\circ$C. arXiv September 8, 2023. https://doi.org/10.48550/arXiv.2309.04555.

(84) Jang, J.-W.; Park, S.; Burr, G. W.; Hwang, H.; Jeong, Y.-H. Optimization of Conductance Change in Pr1–xCaxMnO3-Based Synaptic Devices for Neuromorphic Systems. *IEEE Electron Device Lett.* **2015**, *36* (5), 457–459. https://doi.org/10.1109/LED.2015.2418342.

(85) Baeumer, C.; Schmitz, C.; Ramadan, A. H. H.; Du, H.; Skaja, K.; Feyer, V.; Müller, P.; Arndt, B.; Jia, C.-L.; Mayer, J.; De Souza, R. A.; Michael Schneider, C.; Waser, R.; Dittmann, R. Spectromicroscopic Insights for Rational Design of Redox-Based Memristive Devices. *Nat. Commun.* **2015**, *6* (1), 8610. https://doi.org/10.1038/ncomms9610.

(86) Wedig, A.; Luebben, M.; Cho, D.-Y.; Moors, M.; Skaja, K.; Rana, V.; Hasegawa, T.; Adepalli, K. K.; Yildiz, B.; Waser, R.; Valov, I. Nanoscale Cation Motion in TaOx, HfOx and TiOx Memristive Systems. *Nat. Nanotechnol.* **2016**, *11* (1), 67–74. https://doi.org/10.1038/nnano.2015.221.

(87) Correll, J. M.; Bothra, V.; Cai, F.; Lim, Y.; Lee, S. H.; Lee, S.; Lu, W. D.; Zhang, Z.; Flynn, M. P. A Fully Integrated Reprogrammable CMOS-RRAM Compute-in-Memory Coprocessor for Neuromorphic Applications. *IEEE J. Explor. Solid-State Comput. Devices Circuits* **2020**, *6* (1), 36–44. https://doi.org/10.1109/JXCDC.2020.2992228.

(88) Nukala, P.; Ahmadi, M.; Wei, Y.; de Graaf, S.; Stylianidis, E.; Chakrabortty, T.; Matzen, S.; Zandbergen, H. W.; Björling, A.; Mannix, D.; Carbone, D.; Kooi, B.; Noheda, B. Reversible Oxygen Migration and Phase Transitions in Hafnia-Based Ferroelectric Devices. *Science* **2021**, *372* (6542), 630–635. https://doi.org/10.1126/science.abf3789.

(89) Zhao, Y.; Yavuz, I.; Wang, M.; Weber, M. H.; Xu, M.; Lee, J.-H.; Tan, S.; Huang, T.; Meng, D.; Wang, R.; Xue, J.; Lee, S.-J.; Bae, S.-H.; Zhang, A.; Choi, S.-G.; Yin, Y.; Liu, J.; Han, T.-H.; Shi, Y.; Ma, H.; Yang, W.; Xing, Q.; Zhou, Y.; Shi, P.; Wang, S.; Zhang, E.; Bian, J.; Pan, X.; Park, N.-G.; Lee, J.-W.; Yang, Y. Suppressing Ion Migration in Metal Halide Perovskite via Interstitial Doping with a Trace Amount of Multivalent Cations. *Nat. Mater.* **2022**, 1–7. https://doi.org/10.1038/s41563-022-01390-3.

(90) Zhang, Z.; Zuo, F.; Wan, C.; Dutta, A.; Kim, J.; Rensberg, J.; Nawrodt, R.; Park, H. H.; Larrabee, T. J.; Guan, X.; Zhou, Y.; Prokes, S. M.; Ronning, C.; Shalaev, V. M.; Boltasseva, A.; Kats, M. A.; Ramanathan, S. Evolution of Metallicity in Vanadium Dioxide by Creation of Oxygen Vacancies. *Phys. Rev. Appl.* **2017**, *7* (3), 034008. https://doi.org/10.1103/PhysRevApplied.7.034008.

(91) Sangwan, V. K.; Lee, H.-S.; Bergeron, H.; Balla, I.; Beck, M. E.; Chen, K.-S.; Hersam, M. C. Multi-Terminal Memtransistors from Polycrystalline Monolayer Molybdenum Disulfide. *Nature* **2018**, *554* (7693), 500–504. https://doi.org/10.1038/nature25747.